UNIVERSITY OF SOUTHAMPTON

TRANSITION METAL OXIDES AND OXIDE – HALIDES

A thesis submitted for the Degree of Doctor of Philosophy

by

Marianne Alice Louise Field

SCHOOL OF CHEMISTRY
FACULTY OF SCIENCE, ENGINEERING AND MATHEMATICS

June 2004

UNIVERSITY OF SOUTHAMPTON

ABSTRACT

FACULTY OF SCIENCE, ENGINEERING AND MATHEMATICS
SCHOOL OF CHEMISTRY

Doctor of Philosophy

Transition Metal Oxides and Oxide – Halides

By Marianne Alice Louise Field

Transition metal oxides and oxide halides of the composition $Ln_3Ba_2Mn_2Cu_2O_{12.1}$, $Sr_2Cu_{1-y}Co_yO_2X_2$ (X = Cl, Br), $Sr_3Fe_{2-y}Co_yO_5X_2$ (y = 0, 1, 2, X = Cl, Br) and $NdSrZnO_{4-x}(CO_3)_y$ have been synthesised and the structures of these materials characterised using Rietveld analysis of powder X-ray and powder neutron diffraction data, thermogravimetric analysis, differential thermal analysis and infra-red spectroscopy.

The structures of $Ln_3Ba_2Mn_2Cu_2O_{12.1}$ (Ln = Eu, Sm) have been determined through structure refinement using neutron diffraction data, and the disorder in the anion, and manganese and copper sub-lattices within the layered compounds noted. The displacement of approximately 15 – 20 % of manganese ions into the CuO_2 sheets is likely to preclude the observation of superconductivity in these materials. The partial cross-linking of $Cu(Mn)O_5$ square-pyramids that occurs in the structure, through the addition of excess oxygen, would also be expected to have an inhibiting effect.

Solid solutions of $Sr_2Cu_{1-y}Co_yO_2Cl_2$ and $Sr_2Cu_{1-y}Co_yO_2Br_2$ (y = 0.2, 0.4, 0.5, 0.6, 0.8) have been synthesised and their structures characterised by powder X-ray diffraction. The cell parameters change as the copper ion is replaced by cobalt, with a steady increase in the *a* parameter and gradual decrease in the *c* parameter. This trend reflects the replacement of a Jahn Teller ion (copper (II)) by an ion that is not subject to this effect (high spin cobalt (II)).

The crystal and magnetic structures (where appropriate) of the Ruddlesden-Popper related iron oxyhalides, $Sr_3Fe_{2-y}Co_yO_5X_2$ (y = 0, 1, 2, X = Cl, Br) have been studied using powder neutron powder diffraction. The materials consist of double layers of Fe/CoO_5 square pyramids separated along the *c* direction by SrX 'rocksalt' layers. Powder neutron diffraction data were collected at room temperature and 2 K for $Sr_3Fe_2O_5Br_2$, $Sr_3FeCoO_5Cl_2$ and $Sr_3Co_2O_5Cl_2$ whilst the thermal dependence of both the nuclear structure and the long range magnetic order of $Sr_3Fe_2O_5Cl_2$ in the range 17 K < T < 625 K has been studied, allowing the materials $T_{Néel}$ = 590 K to be determined. All three phases adopt G-type antiferromagnetic spin structures, with the moments confined within the *xy* plane. The materials possess low temperature moments μ = 4.40(4) μ_B, μ = 4.07(6) μ_B, and μ = 2.11(4) μ_B for $Sr_3Fe_2O_5Cl_2$, $Sr_3Fe_2O_5Br_2$ and $Sr_3FeCoO_5Cl_2$ respectively, indicating the presence of high spin iron (III) in all compounds.

The orthorhombic and tetragonal forms of the compound $NdSrZnO_{4-x}(CO_3)_y$ have been synthesised and studied by powder neutron diffraction. The orthorhombic to tetragonal phase transition was confirmed as occurring when oxygen that is distributed between two partially occupied sites in the orthorhombic phase is restricted to only one site within the tetragonal phase, however, the small proportions of carbonate within the two structures proved impossible to model.

"A philospher once said 'it is necessary for the very existence of science that the same conditions always produce the same results' well, they do not."

Richard Feynman

TABLE OF CONTENTS

ACKNOWLEDGEMENTS

I am very grateful to my supervisor, Professor Mark Weller, for the guidance and encouragement he has shown me. I feel lucky to have worked within the Weller group, and have enjoyed working within the Department of Chemistry as a whole these last few years.

Thanks are also due to the EPSRC for the funding of my PhD and the conference they enabled me to attend.

I owe particular thanks to Dr. Chris Knee, especially for the considerable level of support he gave me on a day to day basis throughout my PhD. Other post-docs, recent past and present, from the Weller group were also helpful in providing general advice, but most specifically in relation to the many frustrations experienced during structural refinements. In particular I would like to thank Dr. Paul Henry and Dr. Andrew Hector.

I would also like to extend my thanks to the many members of the Weller group that I have worked with over the last few years. Bob deserves a special mention for helping out with various (and numerous) technical matters, as do Rayne and Seth for being my desk buddies. However, I would not want to fail to mention by name Lee, Jenny, Aaliya (for entertainment value alone), Jon, Nicola, Craig, Jo, Vince, Tom, Stuart, Seth, Tony, Humanzee, Rina and Andrew, thank you for helping to make my time chez camp Weller a happy one.

ABBREVIATIONS

Some commonly used abbreviations in this work:

PXD	Powder X-ray Diffraction
PND	Powder Neutron Diffraction
TOF	Time of Flight
TGA	Thermogravimetric Analysis
DTA	Differential Thermal Analysis
IR	Infra-red
EXAFS	Experimental X-ray Absorption Fine Structure
FWHM	Full Width at Half Maximum
JCPDS	Joint Committee on Powder Diffraction Standards
GSAS	General Structure Analysis System
esd	Estimated Standard Deviation
CMR	Colossal Magnetoresistance
RT	Room Temperature
T_c	Transition Temperature
Tc	Curie Temperature
T_N	Néel temperature
HS	High Spin
IS	Intermediate Spin
LS	Low Spin

Chapter One

Introduction

1.1 Complex Oxide and Oxide-Halide Materials

The varied chemistry of complex metal oxides confers upon them interesting physical properties and thus over the last fifty years this has been an area of intense study. The extended layers of metal-oxygen polyhedra enable the diverse structural units within the overall structure to co-operate electronically, creating a range of macroscopic physical properties. Such properties have resulted in the development of materials suitable for various industrial applications [1] including semi-conductors [2], high-temperature superconducting cables [3], giant magnetoresistant hard-drives [4, 5], rechargeable batteries [6] and capacitors [7].

As a result of the interest created by the discovery of high-temperature superconductivity much work has been directed at layered cuprates, which were thought to be the only structures capable of high temperature superconductivity. The development of new techniques to synthesise and characterise these cuprate phases has also led to a greater understanding of the structural requirements of layered materials in general. In applying the ideas developed for superconductor chemistry to transition metals other than copper (and their oxides) a wealth of new materials, and an awareness of their properties, should result.

Having synthesised these novel phases, structural characterisation is paramount in the understanding of their chemistry and physical properties. Many different experimental techniques exist for the characterisation of oxides, giving information on both the local and long-range structure of the material. These techniques allow the structure/property relationship of a new material to be investigated and possibly optimised for a specific application.

1.2 Perovskite-Based Structures: Simple Building Blocks

There are a large number of mixed metal oxides most of which can be constructed from combining simpler building blocks, such as 'rocksalt', fluorite and perovskite. Perovskites have been the focus of a lot of attention, particularly since the discovery of high-temperature superconductivity, as they are the key

structural unit in high-temperature superconductors and materials demonstrating other key properties, such as Colossal Magnetoresistance (CMR).

1.2.1 The Perovskite Structure

Many materials of stoichiometry ABO_3 take on this structure and it is considered the most common of the ternary phases. The Russian mineralogist L. A. Perovski first determined the structure for the mineral Perovskite, $CaTiO_3$, and even though the mineral has since been discovered to be orthorhombic [8], not cubic (as more commonly associated with the perovskite name) the mineral retains the perovskite name.

For a simple perovskite ABX_3, the large electropositive A cation (e.g. Ba^{2+} or Sr^{2+}) is found in 12-coordinate geometry, whilst the smaller B ion, commonly a small transition metal or main group ion (e.g. Cu^{2+}, Fe^{3+} or Co^{2+}), is in an octahedral environment. The X ion is generally oxygen, O^{2-}, although other anions are known (see later).

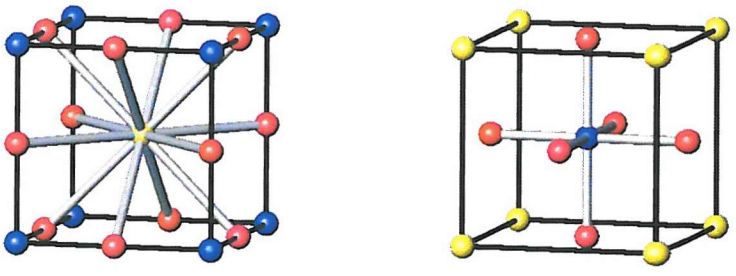

Figure 1.2.1a The Perovskite structure showing the AO_{12} and BO_6 coordination geometry.

The extended structure of a perovskite material can be regarded as a framework of corner-sharing BO_6 octahedra containing 12-coordinate A cations (see Fig 1.2.1b).

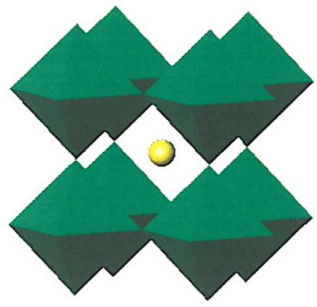

Figure 1.2.1b The 3D framework of BO_6 octahedra containing 12 coordination A cations.

The A, B and O ions need to have suitable ionic radii such that they can make contact and form a bonded structure. These geometric considerations are such that $r_A + r_O$ should equal $\sqrt{2}(r_B + r_O)$, where r is the ionic radius, and from this Goldschmidt [9] developed a tolerance factor *t* that be defined by the expression

$$r_A + r_O = t\sqrt{2}(r_B + r_O)$$

Equation 1.2.1a

which showed the ideal cubic perovskite structure to be stable for $0.8 < t < 0.9$. A variety of distorted perovskite structures are stable over a greater range [10].

The wide range of perovskites that exists is a direct result of two properties of the structure. Firstly, the range of cation sizes that can be accommodated by the structure is great, although this often leads to distortions away from the cubic symmetry (see above). Secondly, the sum of the charges on the A and B ions (+6) may be satisfied by $A^{+}B^{5+}$ (e.g. $KNbO_3$ [11]), $A^{2+}B^{4+}$ (e.g. $SrTiO_3$ [12]) or $A^{3+}B^{3+}$ (e.g. $LaFeO_3$ [13]), or even non-integral compositions, e.g. $La^{3+}(Ru^{4+}_{0.5}Mg^{2+}_{0.5})O_3$ (which has a random distribution of ruthenium and magnesium over the B sites) [14] and $Ba_{0.5}Sr_{0.5}SnO_3$ [15]. The number of possible stoichiometries is further increased by the occurrence of both A cation and oxide non-stoichiometries, such as the tungsten bronzes Na_xWO_3 [16] and the ferrates $SrFeO_{3-x}$ [17].

Anions other than oxide can also be incorporated into perovskites, these include fluorides, $KMgF_3$ [18], chlorides, $CsGeCl_3$ [19], bromides, $CsHgBr_3$ [19], sulphides, $BaZrS_3$ [20] hydrides, $LiEuH_3$ [21], carbides, $GaCo_3C$ [22] and nitrides,

$AgMn_3N$ [22]. The nitrides and carbides have anions in what would be the B cation position for an oxide perovskite, therefore they are known as antiperovskites.

The interesting physical properties that many perovskite materials possess arise as a result of various factors. Structural distortions that cause the unit cell to no longer be centrosymmetric can result in ferroelectric properties, due to the net dipoles that result from the distortions in the cells. Equally cooperative effects can arise from the two- and three-dimensional linking of the transition metal ions through the anions present in the lattice. The high degree of overlap between oxide 2p and 3d transition metal orbitals enables the expression of various properties including magnetic effects. Other physical characteristics arise from particular structural features, such as high-temperature superconductivity and the infinite CuO_2 sheets that are a common structural feature of these materials.

1.2.2 Double Perovskites

Studies on perovskite materials have often taken the form of an exploration of the structure/property relationship of a compound through the systematic change of the size, valence and coordination geometry of the constituent ions. A lot of this work has centred on double perovskites, i.e. $AA'BB'O_6$, and the distribution of the metals within these systems. Three particular B-cation arrangements appear in double perovskites (see Fig. 1.2.2a): random, 'rocksalt' and layered. Which particular structure forms depends on the charge, size and coordination geometry of the B cations, and the A/B size ratio. As the difference between the charges and/or sizes of the B cations increases, the systems tend towards more ordered structures.

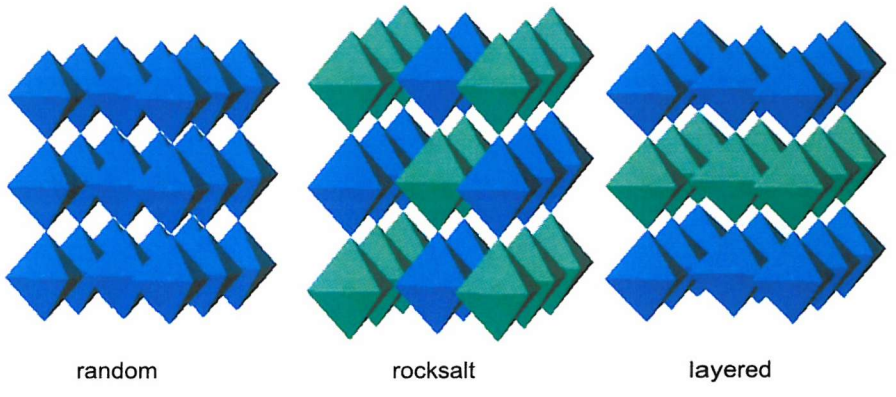

Figure 1.2.2a Possible 'B' cation arrangements in double perovskites.

1.2.2.1 Random Structure Perovskites

Compounds with a random structure show no evidence of B cation order and generally have a cubic (e.g. $BaLaFeMoO_6$ [23]) or orthorhombic unit cell (e.g. $SrLaCuRuO_6$ [24]). An orthorhombic cell is observed when the A–O bond length is less than $\sqrt{2}$ x B–O bond length, i.e. when the Goldschmidt tolerance factor, t, is less than 1.0 (see section 1.1.1). The orthorhombic cell results from correlated tilting of the BO_6 octahedra, which reduces internal bond strain within the structure.

1.2.2.2 'Rocksalt' Structure Perovskites

Compounds with a 'rocksalt' structure show evidence of B cation order, which is indicated by a doubling of the lattice parameters, with respect to those for a random distribution of cations, and the presence of the [111] reflection. This structure type is named after the structure of 'rocksalt' itself because the arrangement of the B and B' cations resembles the arrangement of the anions and cations found in 'rocksalt'. Generally, such materials have a cubic (e.g. Sr_2CuWO_6 [25]) or monoclinic unit cell (e.g. Sr_2LuRuO_6 [26] and Nd_2MgTiO_6 [27]). A monoclinic cell is often observed when the tolerance factor is considerably less than 1.0 and once again results from tilting of the BO_6 octahedra.

1.2.2.3 Layered Structure Perovskites

Compounds with a layered structure also show evidence of B-cation order, which is again indicated by a doubling of the lattice parameters, with respect to those for a random distribution of cations. The layered arrangement is distinguished from the 'rocksalt' unit cell by the presence of the h0l reflections (where h+l=2n+1) and the absence of the [111] reflection. Such materials usually have monoclinic unit cells (e.g. La_2CuSnO_6 [28]) however the oxygen deficient double perovskite $Ba_2InCuO_{4+\delta}$ [29] crystallises with tetragonal symmetry.

1.2.3 Ordering of Transition Metals in Double Perovskites

The ordering of the B cations in double perovskites (general formula A'A"B'B"O_6) is of great interest as it is these ions that generally control the

properties of a material. The layered sublattice is of particular interest because of its rarity and its potential importance in two-dimensional materials (e.g. CuO_2 planes are needed in high-temperature superconductors).

The four factors that control the B cation arrangement are the differences in cation charge, size and coordination environment and the A cation/B cation size ratio [30]. The most important of these is the charge difference and it can be seen that the random structure is prevalent when the charge difference is less than two, whereas when the charge difference is greater than two the 'rocksalt' structure is usually adopted (although the layered structure may form instead).

The difference in the sizes (S) of the B cations is also highly significant, the random arrangement is generally observed when the $S < 0.01$ Å, whilst, the 'rocksalt' arrangement is observed when $0.01 < S < 0.08$ Å, and finally, the layered arrangement is observed when 0.08 Å $< S < 0.12$ Å. Cation size is intimately related to tolerance factors (see Equation 1.2.1a) and A cation/B cation size ratio, as can be seen by studying the Ln_2CuTiO_6 series [31]. As the size of the lanthanide decreases, t decreases, which in turn reduces the probability of stable perovskite phase formation. As the B cation size difference (S) increases, t increases, reflecting the coupling of the increasing two-dimensional B'/B" mismatch with the three-dimensional A/B size mismatch. This results in a perovskite-type compound forming for Ln = La - Gd whereas, a non-perovskite phase is formed when Ln = Tb - Lu.

Another factor that strongly influences the formation of a layered structure is the presence of B cations with different preferred coordination geometries, for example; when B' is a Jahn-Teller ion (which can result in distorted octahedra). The reason for the increased layered phase stability in these circumstances is that the different geometry preferences provide distinct sites for the two B cations within the oxide lattice. Another potential means to encourage layered phase formation is to have different coordination numbers for the two B cations, as in oxygen deficient perovskites.

1.2.4 The K_2NiF_4 Structure

The K_2NiF_4 structure is a tetragonal structure closely related to the perovskite structure and adopts a general formula $AO(ABO_3)_n$. When n=1, a 'layered' perovskite structure is formed, (see Fig. 2.1.2b) which is the structure type of the first member of the Ruddlesden-Popper series discussed in the next section.

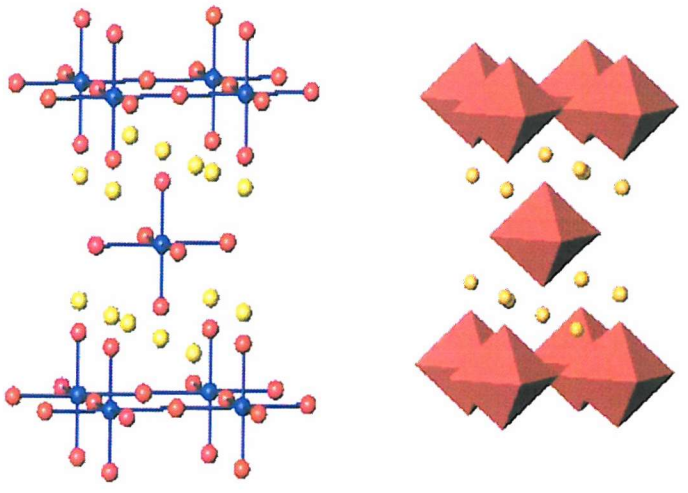

Figure 1.2.4a The structure of K_2NiF_4 showing the NiF_6 coordination and the infinite sheets of octahedra

This structure can be constructed from one B-centred ABO_3 perovskite unit cell with two perovskite A-centred unit cells each with a BX_3 layer removed, one on top of the B-unit and one below. This creates a tetragonal unit cell with the *c* parameter approximately 3 times the length of the *a* parameter [32]. The B atoms are in the same environment as in the perovskite structure, but the A atoms have only nine X ions around them, not 12.

This structure is common for ternary oxides of stoichiometry A_2BX_4 where the A cation is much larger than the B cation. As with simple perovskites, the sum of the charges on the A and B ions (+8) may be satisfied in a range of ways, i.e. by $A^{2+}{}_2B^{4+}$ (e.g. Sr_2TiO_4 [33]), $A^{3+}A^{2+}B^{3+}$ (e.g. $LaSrFeO_4$ [34]) or $A^{3+}{}_2B^{2+}$ (e.g. La_2NiO_4.[35]). The range of B cations for which K_2NiF_4 type structures are known, for particular cations, is smaller than those for which traditional perovskite phases are formed. This can be seen by the fact that $SrFeO_3$ [36], $SrCoO_{3-x}$ [36] and $SrNiO_{3-x}$ [37] all form perovskites but the K_2NiF_4 analogues are unknown for either cobalt or nickel (i.e. Sr_2CoO_4 and Sr_2NiO_4 do not exist).

As is clear from the structure's name, anions other than oxide can be incorporated into materials of K_2NiF_4 structure. Fluorides $A^+_2B^{2+}F_4$ are known for A^+ = K, Rb or Cs and B^{2+} = Mg [38], Mn [38], Fe [39], Co [38], Ni [40], Cu[41] and Zn[42]. A smaller number of chlorides adopt the K_2NiF_4 structure, $Rb_2B^{2+}Cl_4$ (B^{2+} = Mg[43], Cr[44], Mn[45], Cu[46]), as well as bromides, Rb_2MnBr_4[47], and sulphides, $Ba_2B^{4+}S_4$ (B^{4+} = Zr, Hf[48]). Mixed anion structures also exist, in the form of mixed oxide nitrides (e.g. Nd_2AlO_3N and Sr_2TaO_3N [49]) and mixed oxide halides (e.g. Sr_2FeO_3F [50] with fluoride ions taking the apical position). A more recent advance in oxide halide materials is the synthesis of the superconducting material $Sr_2CuO_2F_{2+\delta}$ (T_c = 46 K) [51], formed by fluorine doping of the oxide material Sr_2CuO_3.

As with perovskites, the K_2NiF_4 structure can readily distort from the ideal tetragonal I 4/mmm to more complex orthorhombic structures. The structure can also undergo an elongation in the *c* direction with the copper atoms co-ordinated by an elongated octahedron of six oxygens. This elongation results from the Jahn-Teller effect and is one of the reasons that Bednorz and Müller [52] chose to investigate these copper oxides for superconductivity, indeed the high-temperature superconductor $La_{1.85}Sr_{0.15}CuO_4$ [53] crystallises with this structure. In this compound the lanthanum and barium atoms are similar in size and are randomly distributed over the 'A' cation positions in the structure. The smaller copper atom occupies the 'B' positions.

1.2.5 The Ruddlesden – Popper Phases

These phases were named after Ruddlesden and Popper as they first described this structure type for strontium titanate $Sr_3Ti_2O_7$ [54] in 1957. These phases have general composition $AO(ABO_3)_n$ where $n \geq 2$ and are composed of n ABO_3 perovskite blocks separated by AO layers (n = 1 is equivalent to a K_2NiF_4 structure type), see Figure 1.2.5a. These layers are of 'rocksalt' structure for most crystal structures reported although $La_4Ni_3O_8$ [55] and $Nd_4Ni_3O_8$ [56] have fluorite layers. As n increases the number of examples of this structure type decreases dramatically, this is due to the increasing incidence of stacking faults in the *c* direction; for $n \geq 4$ there are no reports of any crystal structures.

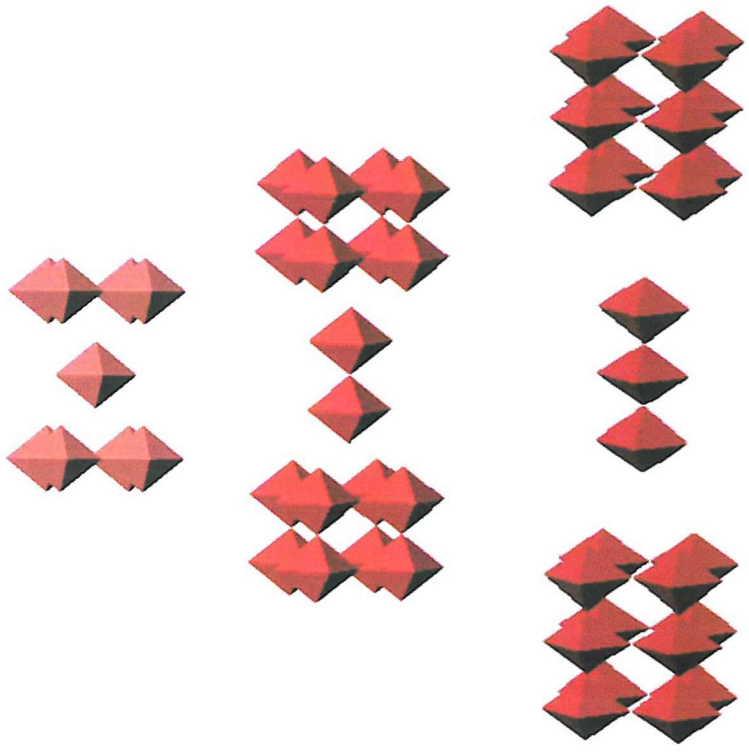

Figure 1.2.5a The structures of Sr_2TiO_4, $Sr_3Ti_2O_7$ and $Sr_4Ti_3O_{10}$ showing the TiO_6 octahedra only.

These phases are often described by their composition such that a K_2NiF_4 structure is known as 2 1 4, $Sr_3Ti_2O_7$ as 3 2 7 structure and $Sr_4Ti_3O_{10}$ as 4 3 10, see the above figure.

Once again the structures can support a number of different cation combinations, including for n = 2 $A^{2+}{}_3B^{4+}{}_2$ (e.g. $Sr_3Ti_2O_7$ [54]), $A^{2+}A^{3+}{}_2B^{3+}{}_2$ (e.g. $SrGd_2Co_2O_7$ [57] and $A^{3+}{}_3B^{2.5+}{}_2$ $La_3Ni_2O_7$ [58]. A large degree of oxygen non-stoichiometry can be accommodated in these systems within the ABO_3 perovskite layers. Such vacancies are normally ordered to produce BO_5 square pyramids (e.g. $Sr_3Fe_2O_6$ [59]) but may be in the form of BO_4 square planes (e.g. $Nd_4Ni_3O_8$ [56]).

Anions other than oxide ions are rarely incorporated into Ruddlesden - Popper phases. For n = 2, there are a few fluorides $K_3B_2F_7$ (B=Mn [60], Fe [60], Co [60], Ni [60], Cu [61], Zn [62]), chlorides $A_3Mn_2Cl_7$ (A=K [63], Rb [64]), an analogous bromide $Rb_3Mn_2Br_7$ [65] and a sulphide $Ba_3Zr_2S_7$ [48]. (N.B. the size of the anion increases

with the size of its alkaline earth counterpart). The oxide halides $Sr_3Fe_2O_5X_2$ [66, 67], $Sr_3Co_2O_5Cl_2$ [68] and $Ba_3In_2O_5X_2$ [69, 70] (X=Cl, Br), $Ca_3Cu_2O_4X_2$ [71] are known mixed oxide halide systems for n = 2 Ruddlesden – Popper phases (the last example possessing oxygen vacancies), whereas, in the case of n = 3 the only well characterised oxide halide systems are the oxide chlorides $Sr_4Co_3O_{7.5}Cl_2$ [72] and $Sr_4Mn_3O_{7.5}Cl_2$ [73]. Other mixed anion systems related to Ruddlesden – Popper phases include $Sr_4Fe_{2-x}M_xO_6CO_3$ (M = Sc, Ni, Co) [74], $Ba_4In_{2-x}O_{6-2.5x}(CO_3)_{1+x}$ [75], $Ba_4In_{0.8}Cu_{1.6}O_{6.2}(CO_3)_{0.6}$ [75], $Sr_4(Fe_{2-x}Mn_x)_{1+y}O_{6(1+y)}CO_{3(1-3y)}$ [76, 77], $(SrO)(SrNbO_{2-x}N)_n$ (n = 1, 2) [78] and $Ln_2Ti_2O_5S_2$ (Ln = Nd, Pr, Sm, Y) [79, 80].

1.2.6 Oxygen Deficient Perovskites

The ideal perovskite structure discussed above only occurs when all atomic sites are fully occupied. Due to the flexibility of the perovskite structure and its ability to accept cations with variable oxidation states, oxygen deficient perovskites are very common [81]. All oxygen deficient phases can be considered as being derived from stacked AO_{3-x} layers. However, the B cations of oxygen deficient phases can reside in six [82], five [83], four [84] or two [85] coordinate interstices that result from a combination of oxygen atoms and vacancies from the layer above and/or below.

The arrangement of vacancies around each B cation in an oxygen deficient perovskite is influenced in a similar way to that of B cation arrangements generally (see section 1.2.3). Differences in size, electronic configuration and coordination preferences of the B cations, and the size and coordination preferences of the A cations affect the vacancy arrangement and control the manner in which the AO_{3-x} layers stack.

Hence the wide range of vacancy patterns observed in various materials is due to the physical and chemical differences in the A and B cations. Comparing the structures of $Ca_2Mn_2O_5$ [83] and $YBaCuFeO_5$ [84] serves as a good example of this relationship (see Fig. 1.2.6a)

The former compound has just one cation, calcium (1.34 Å), whilst the latter contains both yttrium (1.19 Å) and barium (1.61 Å), which differ substantially in size but are of an average ionic radius close to that of calcium (1.4 Å). Although both possess B cations which are exclusively five coordinate there is a fundamental difference in the two structures in that each compound has a distinct stacking sequence. This can be explained by the fact that the coordination requirements of the A sites differ (10, 10 in the calcium manganate phase versus

8, 12 in $YBaCuFeO_5$) and thus the layers must be stacked differently to accommodate this.

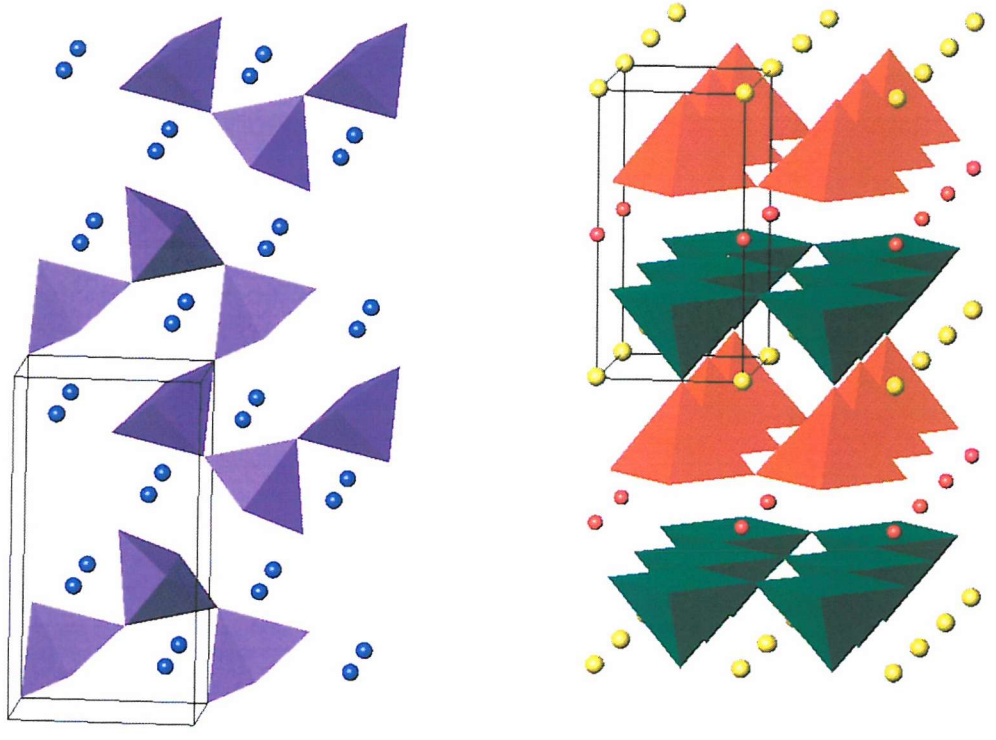

Figure 1.2.6a The structures of $Ca_2Mn_2O_5$ (left) and $YBaCuFeO_5$ (right), showing the MnO_5 and Cu/FeO_5 square-based bipyramids, and the unit cells.

A good example of a well-known structure that adopts an oxygen deficient structure is the high-temperature superconductor $YBa_2Cu_3O_{7-x}$ [86]. This non-stoichiometric system is derived from three perovskite ABO_3 unit cells stacked together directly on top of each other (see Fig. 1.2.6b), to form a material of stoichiometry $A_3B_3O_9$. Copper fills the octahedral corners BO_6, whilst the larger Ba–Y–Ba atoms are positioned in the A sites. Removal of oxygen from the (0,0,½) and (½,0,0) sites yields the $YBa_2Cu_3O_7$ structure.

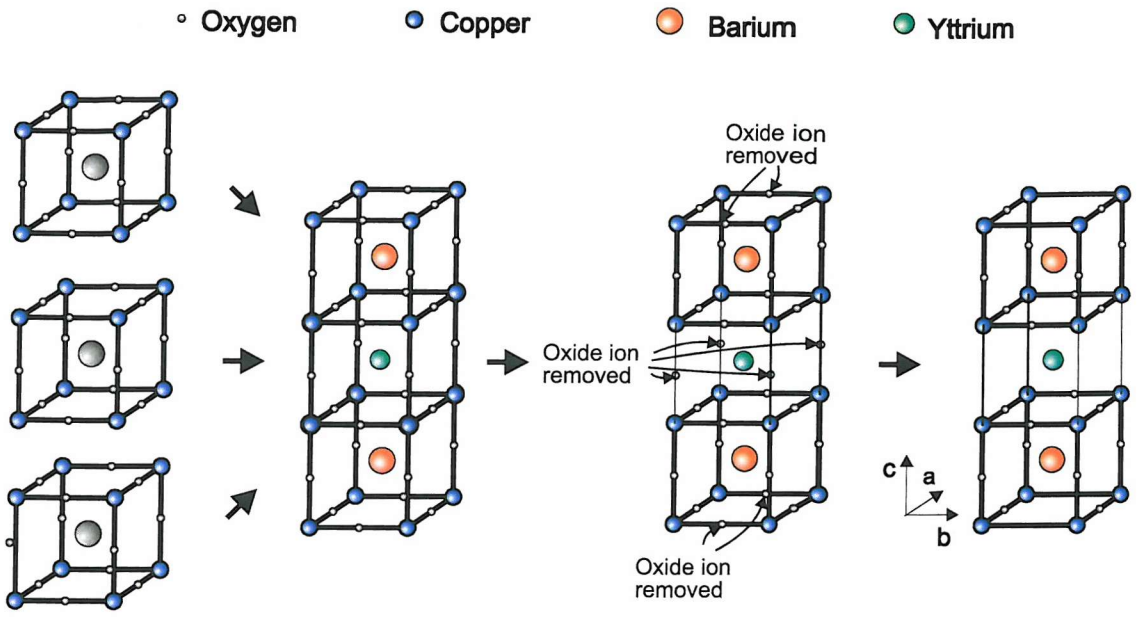

Figure 1.2.6b Derivation of the $YBa_2Cu_3O_7$ structure from a simple perovskite block

The selective removal of oxygen from the sites in the basal plane causes the lattice parameters *a* and *b* to differ resulting in an orthorhombic unit cell (a=3.82 Å, b=3.88 Å, c=11.4 Å). The stacking sequence can be described as:

$$BaO - CuO_2 - Y - CuO_2 - BaO$$

where yttrium is coordinated to 8 oxygens in a distorted cube and barium to 10 oxygens. Copper is in two different coordination environments; square planar and square pyramidal.

1.2.7 Infinite Layer Compounds

Another class of materials based on an oxygen deficient perovskite framework is the infinite layer compounds. The oxygen deficiency within these materials is such that it creates layers of square planes made up from CuO_4 units, separated only by alkaline earth cations. These compounds are of particular importance in the understanding of superconductivity in layered cuprates as they form the basis of most known high temperature superconductors.

Unfortunately, the preparation of most of these materials requires extremely high pressures (~6 GPa) so only a comparatively small number of phases are known to adopt this structure. One non-superconducting material that can be synthesised under atmospheric conditions is $Ca_{0.85}Sr_{0.15}CuO_2$ [87], the ease of synthesis of this compound might be because the particular A cation

stoichiometry present is the optimum for phase stability for this class of compounds.

1.3 Structural Chemistry of Copper

Copper is known to exist in five different oxidation states: 0, +1, +2, +3 and +4 (the most common being +1 and +2), such ions most commonly adopt tetrahedral, square planar or octahedral coordination environments.

The capability of copper to assume numerous different oxidation states results in a varied chemistry and many different coordination geometries. As a variety of coordination geometries may be required of an ion within different sections of a layered compound, layered cuprates are thus quite common and of particular significance to this study. The geometries adopted in the two valencies of most relevance to this work, copper (II) and copper (III), and mixed valence compounds are discussed further in the remainder of this section.

1.3.1 Structural Chemistry of Copper (II)

Due to the structural flexibility of the most common oxidation state, Cu^{2+}, a wide range of compounds exist with such ions in varied coordination environments, though they are often distorted due to the Jahn Teller effect.

The Jahn Teller Effect occurs if the ground state electronic configuration of a non-linear molecule is degenerate, this results in molecules adopting a geometry to remove the degeneracy in the valence level orbitals and become more stable. This often results in tetragonal distortions (see Fig 1.3.1a).

The Jahn Teller Effect occurs with Cu^{2+} (d^9) ions because although theoretically degenerate, the lone electron can occupy either of the $d_{x^2-y^2}$ and d_{z^2} orbitals. A tetragonal distortion lowers the energy of the d_{z^2} orbital and causes a pair of electrons to occupy the d_{z^2} orbital and only one electron is present in the higher energy $d_{x^2-y^2}$ orbital. The degeneracy of the system is removed and lowers the energy of the complex.

This effect is also relevant to d^7 (low spin) and d^4 (high spin) ions, e.g. Cr^{2+}, Mn^{3+}, Fe^{4+}, Ni^{+}, and Ag^{2+}, as they too possess an orbitally degenerate ground state.

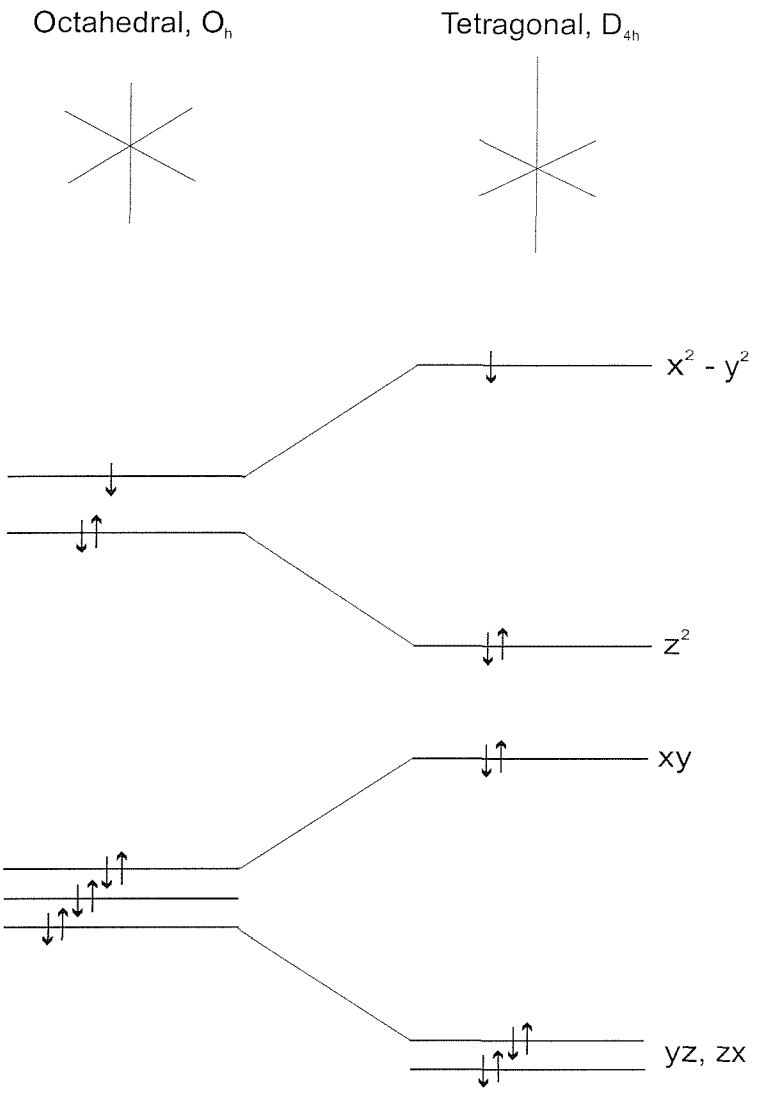

Figure 1.3.1a The Jahn Teller Effect showing the tetragonal distortions in the an octahedral d^9 complex

The distortion produced by the Jahn Teller Effect means that an octahedron with a copper at its centre never has six equal bond lengths, instead it is likely to have four equal bonds in a square planar geometry and two elongated (weaker) apical bonds, e.g. $CuCl_2$, 4 x 2.30Å and 2 x 2.95Å [88], as in the orbital diagram above. The opposite arrangement is also possible, and occurs when two electrons occupy the $d_x^2 - _y^2$ orbital and only one electron is present in the d_z^2 orbital (see section 1.3.1.3). However, knowing that a structure is subject to the Jahn-Teller effect does not enable a prediction as to which distortion will be produced.

The single unpaired electron that results from the Jahn Teller effect allows for unusual interactions within layered cuprates. The electron configuration found

within high-temperature superconductors (and other layered cuprates) would suggest that the lone electron should enable these materials to conduct and yet they are insulators. This suggests that the lone electron present on each copper ion is interacting with others like it within the solid structure as a whole [89]. This interaction has led theoretical physicists towards an explanation for the phenomenon of high-temperature superconductivity, although it is still not fully understood (see section 1.8.1.3).

1.3.1.1 Copper (II) in Four-Coordinate Geometry

Due to the Jahn-Teller effect, divalent copper is rarely found in a regular tetrahedral geometry. For four-coordinate copper, square planar geometries are more commonly encountered and only a few distorted tetrahedral geometries are known. When it occurs, the tetrahedral geometry distortion takes the form of "flattening" (increasing two bond angles away from the ideal 109.5 °) to produce a shape more closely resembling a square planar arrangement.

The structure of crystalline CuO provides a simple example of Cu^{2+} forming four coplanar bonds, the geometry seen in the majority of cuprates in the solid state. The O_{eq}–Cu–O_{eq} bond angles are 2 x 84.5 ° and 2 x 95.5 ° with Cu–O bond lengths of 1.95 Å. The CuO_4 square planes are connected throughout the structure (by edge or corner sharing) to form infinite chains or sheets. This feature is also present in $SrCuO_2$ [90], where edge sharing CuO_4 groups are sandwiched between double layers of SrO. Similar structures are observed in Sr_2CuO_3 [91] and Li_2CuO_2 [92] as well. The Cu–O bonds present in the CuO_4 planes vary in length from 1.9 – 2.0 Å, generally ~1.95 Å. This type of geometry is regularly seen in many superconducting materials (see section 1.8.1.4).

Discrete CuO_4 planes are less common than the infinite interconnected sheets, but may be found in cuprates such as $La_4Ba_2Cu_2O_{10}$ [93].

1.3.1.2 Copper (II) in Five-Coordinate Geometry

Divalent copper can often be found in five coordinate geometries, such as trigonal bipyramidal and distorted square pyramidal.

The elongated square pyramidal coordination results from the Jahn-Teller effect, as described previously, and is generally encountered in cupric oxides. Materials that adopt this structure have four relatively strong planar

interactions (with slightly longer bond lengths than those in purely square planar materials) and a fifth weaker interaction forming the apex of the square based pyramid. As with purely square planar structures, the linking of square pyramids by either edge or corner-sharing can result in infinite chains or planes of CuO_2 stoichiometry, e.g. in $YBa_2Cu_3O_{7-x}$ [86].

Further distortion may occasionally occur, such that one of the two ideal 180 ° O_{eq}–Cu–O_{ax} bond angles decreases whilst the others remain essentially unchanged. This causes the square pyramid geometry to tend towards that of a trigonal bipyramid and usually occurs in materials with a relatively short apical interaction (approx. less than 2.3 Å).

Trigonal bipyramidal species are less common than their square planar counterparts but, nonetheless, well studied. Ions in a trigonal bipyramidal environment usually adopt a significantly distorted structure with the three equatorial bond lengths longer than the two axial ones. A significant distortion in the equatorial plane (away from the ideal 120 ° angle) results in varied O_{eq}–Cu–O_{eq} bond angles with one of these angles being much greater than 120 °. The two axial bonds are approximately the same length as the basal Cu–O bond lengths of the square pyramids, whilst the equatorial bond lengths are also similar in size to the apical Cu–O square pyramidal distance. Two dimensional layers of CuO_5 trigonal bipyramids exist in hexagonal compounds such as $MCuInO_4$ (M = Al, Ga, Fe) [94] where layers of $(Cu/M)O_5$ trigonal bipyramids are corner-sharing to layers of InO_6 octahedra.

1.3.1.3 Copper (II) in Six-Coordinate Geometry

The structural geometry of six-coordinate divalent copper is dominated by distorted octahedral geometry as copper (II) is never seen in an ideal octahedral geometry. Generally a closely bonded equatorial square plane with two weaker orthogonal bonds is seen, with axial bond distances as high as 2.6 Å. At such extremes it is difficult to conclude whether these interactions actually represent bonding.

In some cases, the octahedra distort to form a geometry containing axial bonds that are longer than the corresponding equatorial ones but, which individually, have significantly different bond lengths. Such a distortion can be seen in $Pb_2Cu_2(SeO_3)_3$ [95], which has four equatorial bond lengths between 1.9 Å and 2.0 Å, with additional orthogonal interactions of 2.32 Å and 2.59 Å.

A variation upon the tetragonal distortion in which the equatorial bonds elongate, instead of the axial, is equally possible based on theoretical considerations. However, this is rarely encountered or observed, although it has been reported for materials such as K_2CuF_4 [96]. This material contains two relatively short interactions of 1.94 Å and four longer bonds of 2.07 Å.

1.3.2 Structural Chemistry of Copper (III)

The trivalent state is considerably less stable than the divalent, requiring extreme reaction conditions to prepare purely Cu^{3+} materials as the ions readily reduce to Cu^{2+}. Hence, copper (III) compounds tend to contain copper in combination with highly electronegative elements such as oxygen and fluorine to stabilise the higher oxidation state. As Cu^{3+} is a d^8 ion it is not subject to Jahn Teller distortions and normally exists in a square planar coordination, as seen in the copper (III) oxides $MCuO_2$ (M = Na, K, Rb, Cs) [97]. These materials contain square planar Cu–O bonds approx. 0.1 Å shorter than the bonds in the corresponding Cu^{2+} ternary oxides. Conversely, the structure of $SrLaCuO_4$ [98] is reported to contain a distorted CuO_6 octahedron, with four equatorial bond lengths of ~1.88 Å and two longer axial bonds of ~2.3 Å, similar to the Jahn-Teller distorted octahedral environments.

High oxygen pressures (> 1 bar) are usually required to prepare the $MCuO_2$ materials, and many univalent copper (III) compounds require similariy severe reaction conditions. However, since the discovery of high T_c superconductivity in cuprates much work has been done to develop synthetic methods designed to stabilise unusual oxidation states (e.g. high pressure techniques). Thus the number of known copper (III) compounds is increasing.

1.3.3 Mixed Valence Copper Systems

Transition metal elements have the ability to exist in different oxidation states and consequently a large number of transition metal compounds exhibit mixed valence chemistry [99]. Mixed valence systems can be explained in terms of the Robin and Day classification, which differentiates between systems with a complete ordering (group 1), partial disordering (group 2) or complete disordering (group 3) of the mixed valence metal within the system.

The structural flexibility and range of oxidation states known for copper mean that mixed valence copper compounds are quite common. The resulting

materials adopt similar geometries to those found in single valence copper compounds. The most common mixed valence compounds are those containing the two most stable oxidation states copper (I) and copper (II), mixed copper (II)/copper (III) compounds are less widespread, whilst copper (III)/copper (IV) compounds are extremely rare.

Copper (II)/copper (III) compounds are of most relevance to this work due to their application in high temperature superconductivity (see section 1.8.1.4), and most commonly occur in materials with an excess oxygen non-stoichiometry. Oxygenation of fundamentally divalent materials to fill existing or "created" (by doping) oxygen vacancies can be used to increase the copper oxidation state of a compound. Oxygen-deficient perovskite type structures form the basis of a wide variety of superconducting mixed valence cuprates (see section 1.8.1.4).

Structurally, Cu^{2+} and Cu^{3+} are able to assume similar geometries and often the degree of Jahn-Teller distortion is not sufficient to determine the valence of the copper species. Consequently, Cu^{2+} and Cu^{3+} cannot be easily differentiated within a structure, but as the ordering of copper distributions may be highly important (e.g. in superconducting cuprates) alternative methods of differentiating between the two different valence states may be used to clarify the structure, e.g. bond valence calculations [100, 101] (see Chapter two, section 2.3.6).

1.4 Structural Chemistry of Manganese

Manganese can exist in all of the oxidation states theoretically possible according to an incremental loss of its 3d and 4s electrons, i.e. 0, +1, +2, +3, +4, +5, +6 and +7. Manganese (II) is the most common and most stable oxidation state, however the geometries adopted by manganese (III) and manganese (IV), and mixed valence compounds, are the focus of the remainder of this section as these are the two valencies of most relevance to CMR materials (see section 1.8.3).

1.4.1 Structural Chemistry of Manganese (III)

Unlike copper (II) with its structural flexibility, manganese (III) ions are almost always found in six-coordinate environments. But, as with Cu^{2+} ions, the

coordination environments are usually distorted as Mn^{3+} is d^4 which in high spin configuration is susceptible to the Jahn Teller effect.

α-Mn_2O_3 is a good example of a Jahn Teller distorted structure, Mn^{3+} is in a distorted tetragonal environment with two longer axial and four shorter equatorial Mn-O bonds. This structure is worthy of note as the only distorted example of all the M^{3+} oxides [102]. The structure of MnF_3 is also made up of distorted manganese (III) octahedra.

Low spin Mn^{3+} ions are not subject to the Jahn Teller effect and can be found in different geometries to the distorted octahedron of its high spin equivalent, e.g. $[MnCl_5]^{2+}$ which is square pyramidal.

1.4.2 Structural Chemistry of Manganese(IV)

The simplest example of a manganese (IV) compound is MnO_2. The structure of this compound is complex as a range of polymorphs exists although only one of these is stoichiometric, β-MnO_2.

Manganese (IV) complexes include K_2MnX_6 (X = F [103], Cl [104], CN [105]), whilst there are only a few manganese (IV) complex oxides, e.g. $A_2Mn_3O_7$ (A = Li, Na) [106].

1.4.3 Mixed Valence Manganese Systems

A simple example of a mixed manganese (II)/manganese (III) compound is Mn_3O_4, which is a standard spinel of the form $Mn^{2+}Mn^{3+}{}_2O_4$, with Mn^{2+} and Mn^{3+} ions occupying the tetrahedral and octahedral sites respectively. The manganese (III) environment is more accurately described as being tetragonally distorted due, once again, to the Jahn Teller effect.

Mixed manganese (III)/manganese (IV) compounds are of most relevance to this work, as mentioned above, and have been studied in some depth. Examples include $La_{1-x}A_xMnO_3$ (A = Sr, Ca, x = 0 – 0.5) [107] and $A_{1-x}A'_xMnO_{3+\delta}$ (A = La, Nd, Pr, Sm, Y, A' = Ca, Sr) [108].

As with Cu^{2+} and Cu^{3+}, problems can occur when trying to differentiate between Mn^{3+} and Mn^{4+} within a structure. Bond valence calculations [109, 110] (see Chapter two, section 2.3.6) can, as mentioned previously, be used as a method of differentiating between the two different valence states and to clarify the structure.

1.5 Structural Chemistry of Cobalt

The most common oxidation states present in cobalt compounds are Co^{2+} and Co^{3+}, although Co^{+} and Co^{4+} compounds can be synthesised using extreme conditions (e.g. 1000 °C using a diamond anvil device to provide a pressure of 65 Kbar to form $SrCoO_3$ [111]). In the solid state the trivalent state of cobalt is partially favoured, as shown by the oxidation of CoO to Co_3O_4 upon sintering in air.

Typically cobalt (II) and cobalt (III) exist in tetrahedral or octahedral coordination environments, their geometries are discussed in greater detail in the remainder of this section.

1.5.1 Structural Chemistry of Cobalt (II)

Cobalt (II) complexes are normally tetrahedral or octahedral, although a few examples of five coordinate and square planar species do exist. There are more tetrahedral compounds of Co^{2+} than for any other transition metal. This results from the d^7 electron configuration, which has the least disfavour for tetrahedral geometry compared to octahedral, for any d^n metal. $[CoX_4]^{2-}$ tetrahedral complexes are usually formed with unidentate ligands, e.g. the halides Cl, Br and I. Octahedral Co(II) complexes, such as $[Co(H_2O)_6]^{2+}$, generally prefer to adopt a high spin configuration, with the low spin octahedral complexes tending to lose ligands to become five or four-fold coordinated. Purely divalent cobalt materials are rare and may be difficult to synthesise, e.g. La_2CoO_4 [112] is prepared by the reaction of CoO and La_2O_3 at 2000 °C under carbon dioxide or argon. It has an orthorhombic structure (4 x 1.944 Å equatorial bonds and 2 x 2.034 Å axial bonds) based on a distorted K_2NiF_4 tetragonal system and is isostructural with La_2CuO_4.

1.5.2 Structural Chemistry of Cobalt (III)

Almost all cobalt (III) compounds are octahedrally coordinated, due to the enhanced stability of the octahedral low spin d^6 configuration. Cobalt amine complexes have been extensively studied and provide numerous examples of octahedral Co^{3+}, e.g. the successive replacement of NH_3 in the series $[Co(NH_3)_{6-n}X_n]$ with X = Cl, Br, NO_3 [102]. The low spin arrangement causes the

materials to be diamagnetic and their magnetic properties are therefore of little interest. Compounds containing trivalent cobalt in the solid state are quite abundant, but once more purely trivalent cobalt materials are quite rare, e.g. the brownmillerite phase $Sr_2Co_2O_5$ [69]. Interesting examples of cobalt (III) compounds include lithium based cathode materials such as $LiCoO_2$ [113] (which contains layers of octahedral Co and Li) and the $YBa_2Cu_3O_7$ based material $Y(Ba_{1.44}K_{0.56})Co_3O_{7.9}$ [114].

1.5.3 Mixed Valence Cobalt Systems

Co_3O_4 is a simple example of a mixed cobalt (II)/cobalt (III) compound. This material can be more accurately described as $Co^{2+}Co^{3+}{}_2O_4$ and has the standard spinel structure, with Co^{2+} ions in tetrahedral sites and Co^{3+} in octahedral sites within the oxide lattice.

Oxygen deficient Ruddlesen-Popper type phases $Sr_3Co_2O_{7-\delta}$ ($0.94 \leq \delta \leq 1.22$) have also been reported [115], with the partial occupancy of the oxide sites within the structure resulting in both octahedral and square pyramidal cobalt coordination environments with Co-O bond distances in the range ~ 1.87-2.0 Å.

Cobalt (III)/cobalt (IV) compounds also form, e.g. $SrCoO_{3-\delta}$ [116] and $La_{1-x}Sr_xCoO_3$ [117]. Such materials exhibit a wide range of oxygen non-stoichiometry and adopt varied perovskite related structures.

1.6 Structural Chemistry of Iron

The most common oxidation states present in iron compounds are Fe^{2+} and Fe^{3+}, although all the oxidation states from 0 to 7 are known in various coordination compounds [102]. Iron favours the trivalent state in the solid state, as is shown by the natural abundance of the mineral haematite (α-Fe_2O_3).

The structure of iron (III) compounds forms the focus for the remainder of this section, as this is the valence of most relevance to magnetic effects (as explored in chapter 6).

1.6.1 Structural Chemistry of Iron (III)

Octahedral environments are generally favoured for iron (III) compounds which, as with manganese (III) can be of either high spin or low spin configuration. High-spin complexes are more common for the six-coordinate complexes whereas the spin configuration for five-coordinate complexes is almost entirely dependent on the ligands present in the complex.

Simple iron (III) compounds include $K_6Fe_2O_6$ [118], which adopts a structure formed from pairs of edge-sharing tetrahedra. Whilst the coordination chemistry of iron (III) is varied, with the ion forming complexes with all the common anions (bar those that have reducing properties, e.g. I^-), almost all such complexes are octahedral.

The $YBa_2Cu_3O_7$ based materials $LnBa_2Fe_3O_8$ (Ln = Dy, Er, Y) [119], and compounds related to the mineral $Pb_4Fe_3O_8Cl$ (e.g. $Pb_4Fe_3O_8Br$ [120]) are good examples of layered iron (III) materials.

1.7 Structural Chemistry of Zinc

This metal is very rarely found in any oxidation state other than +2, when it loses both of its 4s electrons, thus it forms compounds with full d shells and is not generally regarded as a transition metal. It does share some properties with d elements, however, as a small degree of $d\pi$ bonding may occur between metal and ligand in some complexes [122].

1.7.1 Structural Chemistry of Zinc (II)

Due to its full d shell Zn^{2+} doesn't have a ligand field stabilisation effect, and the stereochemistry of the ion is determined entirely according to ionic size, electrostatic forces and covalent bonding forces. Although small in size the Zn^{2+} ions are often found in an octahedrally coordinated structure, four-coordinate zinc is also common. Four-coordinate zinc ions are usually found in a tetrahedral environment, as seen in ZnO (which crystallises in a lattice with each zinc ion surrounded by four oxygens, as opposed to CdO, which adopts the 'rocksalt' structure with cadmium ions in octahedral coordination) and $ZnGa_2O_4$ with Zn^{2+} ions in the tetrahedral sites and Ga^{3+} ions in the octahedral sites [32]. A

coordination number of five is the most rare coordination environment for zinc, although both trigonal bipyramidal and square pyramidal geometries have been observed.

1.8 Cooperative Phenomena Arising from Extended Metal-Oxide Pathways

1.8.1 Superconductivity

1.8.1.1 A Brief History of Superconductivity

In 1911 Onnes discovered superconductivity [123] when he cooled mercury to 4.2 K, its transition temperature (T_c), at which point it seemingly displayed zero electrical resistance. Further research showed that many other metals and alloys also possessed this unusual property and progress in transition temperatures was made at a rate of approximately 3 K per decade up to 23 K after 75 years [124]. Then, in 1986 Bednorz and Müller [52] made an unexpected breakthrough with the discovery of a high-temperature superconductor, $La_{2-x}Ba_xCuO_4$ (T_c of 35 K for $x \approx 0.5$). This led to intense exploration of ceramic materials as possible superconductors, readily yielding a T_c of 40 K for the $La_{2-x}Sr_xCuO_4$ system. The introduction of strontium was thought to further strain the Cu-O layers so lanthanum was replaced by smaller lanthanides to counteract this effect. This led to the discovery of $YBa_2Cu_3O_{7-\delta}$ ($\delta \approx 0.1$) [86], with a T_c (92 K) high enough to use with liquid nitrogen, making superconductors suited to conventional cryogenic technology for the first time. Research into ceramic superconductors has continued and the highest transition temperature to date is 135K for $HgBa_2Ca_2Cu_3O_{10}$ [125].

Advances in the field of superconductivity have included many more diverse compounds. Organic compounds were first discovered to be capable of superconductivity with $(TMTSF)_2PF_6$ [126] in 1980, but only with an extremely low T_c (0.9 K). Exploration of this class of materials raised the transition temperature to 13 K (for kappa-$(ET)_2Cu(N(CN)_2)Cl$ [127]) by 1990 but this field has not experienced the almost exponential increase in transition temperature that was seen in cuprate chemistry. The phenomenon has also been shown to exist in fullerenes such as C_{60} [128], and the T_c of such materials was raised by forming intercalation compounds, called fullerides, of general type M_3C_{60} where M = K, Rb or $CsRb_2$ with

T_c up to 33 K [129]. More recently the simple compound MgB_2 was found to superconduct at the surprisingly high temperature of 39 K [130].(or 40 K with ^{11}B [131]) and recent studies are now investigating the intercalation chemistry of this material.

Applications of high T_c cuprates have centred on $YBa_2Cu_3O_7$ and $Bi_2Sr_2CaCu_2O_8$. These materials have been made into thick films, thin films, large grains and wires, which in turn can be used in microwave devices, SQUID magnetometers, levitation devices, electrical conducting wires, etc [132].

Although all types of superconductor are of interest to the materials chemist, the high-temperature superconductors are of particular relevance to this study. Thus the common structural features of such materials will be discussed in greater detail in a later section.

1.8.1.2 Properties of Superconductors

Although the zero electrical resistance of superconductors is the principal reason for the attention shown to such compounds, another property of interest that they possess is the Meissner effect, which is the exclusion of a magnetic field.

When a magnetic field is applied across a superconductor at temperatures less than its T_c, the electrons or holes present within the material generate surface currents that create a magnetic field of equal and opposite magnitude (this can be demonstrated by the levitation of permanent magnets). However if the applied magnetic field exceeds a critical value, H_c, it cannot be expelled and superconductivity ceases to be exhibited by the material.

There are two classes of superconductors, Type I and Type II. Type I superconductors are pure elements, e.g. mercury, have low T_cs and behave as perfect diamagnets excluding a magnetic field completely until the critical field H_c is reached, when they suffer a vertical drop in magnetisation. Type II superconductors are generally alloys and complex oxides, have higher T_cs and are imperfect diamagnets showing a gradual magnetic field penetration above a lower critical field H_{c1} followed by a gradual loss of superconductivity until an upper critical field H_{c2} at which it is completely lost. Because of their ability to withstand higher magnetic fields superconducting magnets for industrial applications, e.g. NMR, are often made from Type II materials such as Nb/Ti alloy [124].

1.8.1.3 Theories of Superconductivity

Low-temperature superconduction is commonly explained by the existence of a Cooper pair, which is a pair of electrons that is scattered less than a lone electron as it travels through the solid. This is due to the distortion caused by one electron attracting the other electron, preventing it from being significantly scattered from its path in the event of a collision. In effect there is a virtual attraction between the two electrons because the local distortion in positive charge makes it favourable for the second electron to join the first. Due to its stability against scattering the Cooper pair can carry charge readily through the solid, giving rise to superconduction.

The local distortion in the lattice is easily disrupted by thermal motion of the ions within the solid, thus this effect only occurs at very low temperatures and for materials with low transition temperatures. There is no firm explanation for the occurrence of high-temperature superconductivity, but it is thought the intrinsic concept of Cooper pairs, i.e. a virtual attraction enabling synchronous movement of energy within a lattice, is important within the mechanism of high-temperature materials as well as for conventional superconductors.

1.8.1.4 Common Features in High-Temperature Superconductors

Two features recur in the structures of complex cuprate superconductors: infinite sheets of CuO_2 planes, with mixed copper valencies of an average oxidation state greater than 2+ (except for in the material $Nd_{2-x}Ce_xCuO_4$, x = 0.05 – 0.3 [133]), and insulating layers. The CuO_2 layers are separated by insulating 'charge reservoir' layers (except for in the infinite layer compounds), e.g. CuO chains and Ba_2O_2 'rocksalt' layers in $YBa_2Cu_3O_7$. Superconductivity is thought to take place in the CuO_2 planes and the charge reservoir layers ensure the correct charge or electron concentration is supplied to these planes (see Fig. 1.8.1.4a).

The CuO_2 Planes

The presence of CuO_2 planes in high-temperature superconductors is made possible by the various coordination geometries and oxidation states that copper can adopt. Copper can be in six-fold (octahedral), five-fold (square pyramidal), and four-fold (square planar) coordinations within the planes; linking of these CuO_4 square planes (present in all these structural elements) forms CuO_2 layers. With these layers conduction bands are formed by the overlap of the

$d_{x^2-y^2}$ orbital of copper and the p_x and p_y orbitals of oxygen, with Cu – O distances characteristically 1.9 – 1.95Å in length. As a result of the Jahn-Teller distortion that occurs (see section 1.3) the hybrid $d_{x^2-y^2}/p_xp_y$ band is a high energy anti-bonding orbital. This band, being half filled, should cause the material to behave as a metal, but instead semiconducting properties are observed. Such behaviour results from the strong electron correlations within the band, which induce antiferromagnetic semiconducting behaviour. Superconductivity is only observed for a narrow range of mixed valence (Cu^{2+}/Cu^{3+}) compositions between antiferromagnetic (see section 1.8.2) semiconducting and normal metallic behaviour. This mixed valence ensures the correct charge carrier concentration on the CuO_2 planes, which in turn depends on whether the carriers are positive holes (p-type superconductors) or electrons (n-type superconductors).

The great majority of high-temperature superconductors are p-type and the optimum copper oxidation state is approximately 2.2+. The ratio of Cu^{2+}/Cu^{3+} ions, and thus the average value of the oxidation state, may be controlled by donor intercalation, metal substitution, halogen substitution and addition/removal of oxygen.

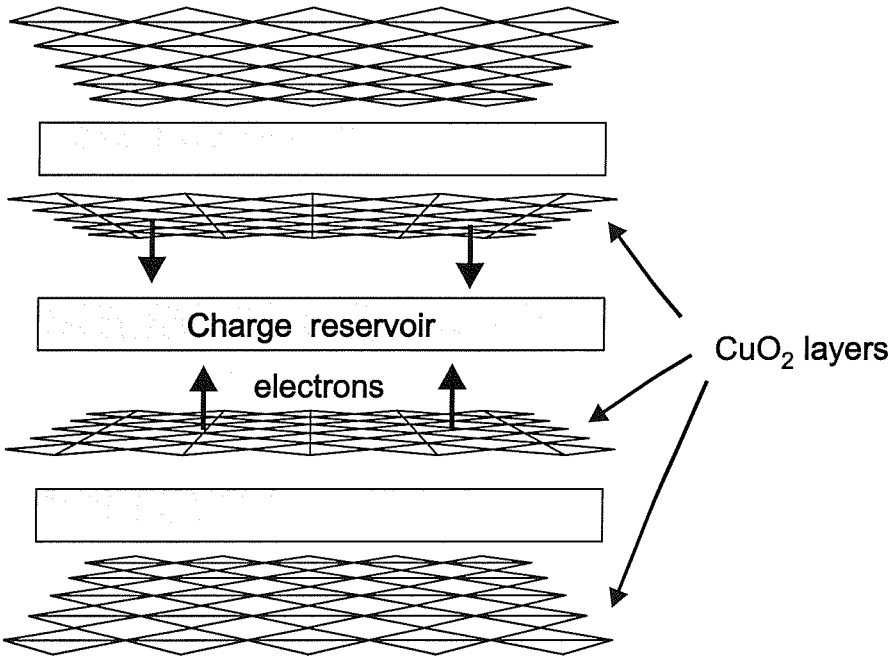

Figure 1.8.1.4a Schematic representation of the structural features of high temperature superconducting cuprates

Role of the Separating Layer

With the exception of the infinite layer compounds (see section 1.2.6), all superconducting cuprates have separating layers between the CuO_2 planes, *e.g.* CuO chains in $YBa_2Cu_3O_{7-\delta}$, double fluorite layers in $NbSr_2(Nd/Ce)_2Cu_2O_{9-\delta}$ [134] or Tl_2O_2 'rocksalt' layers in $Tl_2Ba_2CaCu_2O_8$ [135]. Structural variations in these metal and/or metal-oxygen layers that separate the CuO_2 planes result in changes in the electronic properties of the material as a whole. By controlling the copper oxidation state, and thus the charge carrier (positive holes or electrons) concentration within the CuO_2 planes, these separating layers (or charge reservoirs) help create the conditions required for superconductivity.

1.8.2 Magnetism

Electrons have spin as well as charge and the orientation of unpaired electrons determines a material's magnetic behaviour. A random orientation of electron spins is known as *paramagnetism*, when unpaired electrons align themselves parallel to each other this is *ferromagnetism*, whereas *antiferromagnetism* occurs when spins align anti-parallel (with a net magnetic moment of zero). Another type of magnetic behaviour is *ferrimagnetism*, which results from ions with different spins aligning antiferromagnetically, but unequally, to give a net moment.

Magnetic interactions are generally quite weak and will be readily overcome by the constant thermal movement that occurs at relatively high temperatures, causing a sample to exhibit paramagnetic behaviour. Below a transition temperature, the value of which varies from one magnetic material to another, the magnetic energies surpass the thermal energies and the spins align. This ordering temperature is known as the Curie temperature (Tc) in the case of ferromagnetic materials.

The magnetic susceptibility (χ) of a material is a measure of its magnetisation when in an external magnetic field. The spins within a paramagnetic material will partially align themselves with the field, although thermal effects will counteract this ordering such that the higher the temperature the lower the magnetic susceptibility. In ferromagnetic materials the spins align increasingly strongly (causing concurrent increases in the magnetic susceptibility) once the thermal energy barrier to ordering is overcome at Tc. Antiferromagnetic

materials will align their spins half parallel and half anti-parallel to the external field, such that once the thermal energy barrier to ordering is overcome, at the Néel temperature (T_N), their magnetic susceptibility gradually decreases. A representation of these effects is displayed below:

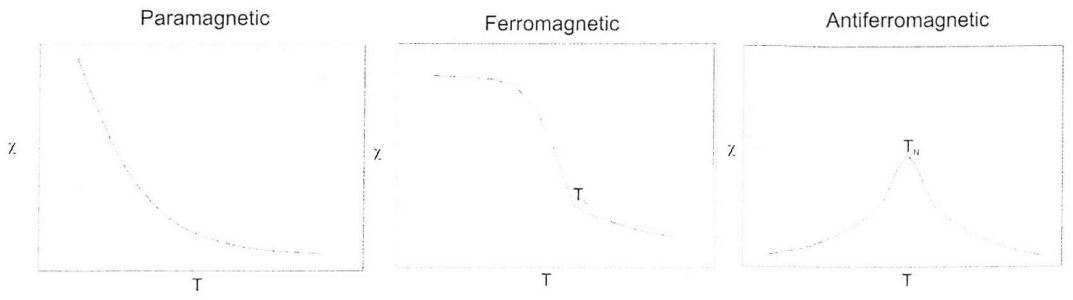

Figure 1.8.2a Temperature Dependence of Magnetic Susceptibility of Paramagnetic, Ferromagnetic and Antiferromagnetic materials

For the alignment of magnetic spins to occur spontaneously it follows that there must be an energetic interaction between neighbouring spins. The coupling of spins to give rise to antiferromagnetism is thought to occur in many materials by a process known as *superexchange*, in which the orbitals of metal ions lie in the same direction as the orbitals of the oxygen ion between them. Thus a chain coupling can occur through the oxygen, such that the spins of the two metal ions lie antiparallel to each other. Due to the fact that the parent compounds of high temperature superconductors (and materials exhibiting colossal magnetoresistance, see section 1.8.3) are antiferromagnetic, and that subtle changes (e.g. doping) can produce such interesting properties, a lot of research has been done to increase understanding of these compounds (e.g. La_2CuO_4 [136] and $LaMnO_3$ [137]).

Neutron diffraction can be useful in determining the magnetic structure of a material as neutrons interact with the unpaired electrons present in a material, due to them possessing a magnetic dipole moment. The additional scattering effect of the interaction between the neutrons and unpaired electrons can cause additional peaks to appear in the diffraction profile, which are indicative of the magnetic superstructure present in the material. It is possible to determine if a material is ferromagnetic or antiferromagnetic by studying these peaks.

1.8.3 Colossal Magnetoresistance

The current level of understanding of colossal magnetoresistance (CMR) has arisen principally from initial work carried out on perovskites derived from $LnMnO_3$ (Ln = lanthanide) [138]. These materials became the focus of this area of research approx. 10 years ago, when it was shown that certain manganese oxides showed a large change in resistance when a magnetic field was applied [139]. These are anti-ferromagnetic because Mn^{3+} (d^4) undergoes Jahn-Teller distortions which cause ferromagnetic ordering from the e_g orbitals and ½ filled t_{2g} orbitals. Alkaline earth metal (e.g. calcium) doping of such materials introduces some Mn^{4+} to create a metallic ferromagnet.

If a sample of $La_{0.7}Ca_{0.3}MnO_3$ is cooled its resistance increases slowly until approx. 250 K at which point the electrical resistance of the material suddenly drops by a factor of approx. 10,000 times, this effect is known CMR. The temperature at which this effect occurs, for any given material, will be almost the same as the T_c for that material, i.e. when it suffers a substantial drop in resistance it also becomes magnetic as the spins of its outer electrons align.

A great deal of interest is being shown in CMR as a medium for data storage and one of the areas of research growth related to this is layered transition metal oxides, which are thought to hold the key to even greater magnetoresistance.

1.8.3.1 Theories of Colossal Magnetoresistance

The CMR effect is thought to be linked to the fact that although both lanthanum and calcium donate electrons to the lattice, the calcium atoms, because they donate fewer electrons, cause a shortfall in the sea of donated electrons. This creates electron mobility and these "free" electrons interact with other "fixed" electrons that are attached to the manganese sites. The "fixed" electrons give these sites their spins, past which the free electrons must move.

When ferromagnetism occurs the spins of the “fixed” electrons line up and as the spins of the "free" and “fixed” electrons interact this helps a “free” electron move through the aligned spins of the material. This explanation of why the high $\rightarrow$ low resistance and non-magnetic $\rightarrow$ magnetic transitions occur near the same temperature is known as the *double exchange model*. However, this simple model is imperfect and does not take account for the mixture of Mn^{4+} and Mn^{3+}

ions needed for CMR to be observed. This mixture of valences is key to the model, especially when you consider the change in ion symmetry that occurs when an electron alters the oxidation state of a particular ion. When an ion alters from Mn^{4+} to Mn^{3+} the ion increases in size and becomes less symmetrical. Thus an electron moving from one ion to another must cause distortions along its path, this requires a lot of energy, which in turn causes great resistance to its movement [140]. The de-localisation of electrons that occurs when their spins align prevents differentiation between individual ions and removes the distortion energy barrier. This model offers a fuller, but not entirely comprehensive explanation of CMR.

Phase diagrams have shown that the electrical properties of CMR materials are dependent upon chemical composition, i.e. $La_{1-x}Sr_xMnO_3$ is very different from $Pr_{1-x}Ca_xMnO_3$ [141]. This complicates the explanation of this behaviour even further.

1.8.3.2 Common Features in CMR materials

As with superconductivity there appear to be common factors amongst CMR perovskites. These include a Mn^{4+} content (relative to total manganese content) of approximately 33 %, linked metal oxygen pathways and a particular average size of interpolated cation (A, Ln) [142]. Additionally, the lower the T_c of the material the greater the level of magnetoresistance.

1.9 The Scope of this Work

Although copper oxides have been studied extensively due to the interest in high T_c superconductivity there is still much that remains to be done within this field of research. The work carried out thus far, although comprehensive, has not exhausted the possibilities within the chemistry of cuprates. Whilst the search for new layered oxide materials exhibiting interesting and useful properties continues expansion of research into oxide halides, other metal oxides and mixed metal systems has proved fruitful. This exploration of layered oxide chemistry has helped develop an understanding of the relationship between structure and property that is of fundamental interest to materials chemistry.

The focus of this work has been to explore the relationship between structure and property in layered oxides and oxide chlorides, by synthesising and characterising a range of materials. More specifically, chapter three presents the results of a powder neutron diffraction study of the layered mangano-cuprates $Ln_3Ba_2Mn_2Cu_2O_{12\pm\delta}$ (Ln = Eu and Sm). These materials were of interest as they appeared to have the common characteristics of both high T_c superconductors and colossal magnetoresistance materials. Chapter four concentrates on the development of the Jahn Teller effect in a solid solution, by examining powder X-ray diffraction data for the phases $Sr_2Cu_{1-y}Co_yO_2X_2$ (X = Cl and Br, y = 0.2, 0.4, 0.5, 0.6, 0.8). Chapter five explores the structural effects of halide and cobalt substitution upon a known iron oxide chloride, investigating the changes to crystal structure and sublattice magnetisation that occur using powder neutron diffraction. The material $NdSrZnO_{4-x}$ is examined in chapter six in an effort to investigate its unusual structural transition from a tetragonal to an orthorhombic material.

Some of the compounds studied have been previously reported, but not fully characterised, and the work in this thesis has enabled their chemical and physical properties to be more fully explored.

1.10 References

1 Subramanian M A, Aravamudan G, Subba Rao G V, *J. Solid State Chem.*, 1980, **31**, 329

2 Galasso F, Derby W, *Inorg. Chem.*, 1965, **1**, 71

3 in 'Editorial', *New Sci.*, 2001, **169** (2284), 3

4 Derbyshire K, Korczynski E, *Solid State Technol.*, 1995, **38** (9), 57 and in 'Technology', *New Sci.*, 1994, **143** (1932), 19

5 Ney A, Pampuch C, Koch R, Ploog K H, *Nature*, 2003, **425**, 485

6 Hunger H F, Bramhall P J, J Electrochem. Soc. 1983, **130** (8), C308-C308

7 Carrano J, Sudhama C, Chikarmane V, Lee J, Tasch A, Shepherd W, Abt N, *IEEE T. Ultrason. Ferr.*, 1991, **38** (6), 690

8 Subramanian M A, Calabrase J C, Torardi C C, Gopalakristashan J, Askew T R, Flippen F R, Morrisey K J, Chowdry U, Sleight A W, *Nature*, 1988, **332**, 440

9 Goldschmidt V M, Skrifter Norske Videnskaps-Akad. Oslo, I. Mat.-Naturv. Kl., No.8, 1926

10 Anderson P W, *Physica C*, 1991, **185-189**, 11

11 Wood E A, *Acta Crystallogr.*, 1951, **4**, 353

12 Brous J, Fankuchen I, Banks E, *Acta Crystallogr.*, 1953, **6**, 67

13 Koehler W C, Wollan E O, *J. Phys. Chem. Solids*, 1957, **2**, 100

14 Galasso F S, *Structure and Properties of Inorganic Solids*, Pergamon Press, Oxford, 1970

15 Bayer G, *J. Am. Ceram. Soc.*, 1963, **46**, 604

16 de Jong W F, *Z. Krist.*, 1932, **81**, 314

17 Brisi C, *Ricerca Sci.*, 1954, **24**, 1858

18 Ludekens W L W, Welch A J E, *Acta. Crystallogr.*, 1952, **5**, 841

19 Naray-Szabo I, *Mulgyet Zoylemen*, 1947, **1**, 30

20 Clearfield A., *Acta Crystallogr.*, 1963, **16**, 134

21 Messer C E, Hardcastle K, *Inorg. Chem.*, 1964, **3**, 1327

22 Nowtony H, Ettmayer P, *J. Inst. Met.*, 1996, **97**, 180

23 Nakamoto T, Choy J H, *J. Solid State Chem.*, 1977, **20**, 233

24 Attfield M P, Battle P D, Bollen S K, Kim S H, Powell A V, Workman M, *J. Solid State Chem.*, 1992, **96**, 344

25 Blassé G, *J. Inorg. Nucl. Chem.*, 1965, **27**, 993

26 Battle P D, Jones C W, *J. Solid State Chem.*, 1989, **78**, 108

27 Groen W A, van Berkel F P F, Ijdo D J W, *Acta Crystallogr., Sect. C: Cryst. Struct. Commun.*, 1986, **42**, 1472

28 Anderson M T, Poeppelmeier K R, *Chem. Mater.*, 1991, **3**, 476

29 Gregory D H, Weller M T, *J. Mater. Chem.*, 1994,**4**, 921

30 Anderson M T, Greenwood K B, Taylor G A, Poeppelmeier K R, *Prog. Solid St. Chem.*, 1993, **22**, 197

31 Palacin M R, Bassas J, Rodriguez-Carvajal J, Gomez-Romero P, *J. Mat. Chem.*, 1993, **3**, 1171

32 Wells A F, *Structural Inorganic Chemistry*, Clarendon Press, Oxford, 1962

33 Range K J, Rau F, Klement U, *Z. Naturforsch.*, 1991, **46**, 1315

34 Russell L E, Harrison J D L, Brett N H, *J. Nucl. Mater.*, 1960, **2**, 310

35 Weiss R, *Compt. Rend.*, 1958, **246**, 3073

36 Yakel H L, *Acta. Crystallogr.*, 1955, **8**, 394

37 Takeda Y, Hashino T, Miyamoto, H, Kanamaru F, Kume S, Koizumi M, *J. Inorg. Nucl. Chem.*, 1972, **34**, 1599

38 Babel D, Herdtweck E, *Z. Anorg. Allg. Chem.*, 1982, **487**, 75

39 de Pape J, *Bull. Soc. Chim. Fr.*, 1965, 3489

40 Balz D, Plieth K, *Z. Elektrochem.*, 1955, **59**, 545

41 Haegele R, Babel D, *Z. Anorg. Allg. Chem.*, 1974, **409**, 11

42 Babel D, Herdtweck E, *Z. Kristallogr.*, 1980, **153**, 189

43 Gibbons C S, Reinsborough V C, Whitla W A, *Can. J. Chem.*, 1975, **53**, 114

44 Fair M J, Gregson A K, Day P, Hutchings M T, *Physica B*, 1977, **86**, 657

45 Goodyear J, Ali E M, Steigmann G A, *Acta Crystallogr., Sect. B: Struct. Sci.*, 1977, **33**, 2932

46 Witteveen H T, Jongejan D L, Brandwijk V, *Mater. Res. Bull.*, 1974, **9**, 345

47 Goodyear J, Ali E M, Sutherland H H, *Acta Crystallogr., Sect. B: Struct. Sci.*, 1979, **35**, 456

48 Chen B H, Eichhorn B, *Mater. Res. Bull.*, 1991, **26**, 1035

49 Assabaa-Boultif R Marchand R, Laurent Y, Videau J-J, *Mater. Res. Bull.*, 1994, **29**, 667

50 Galasso F, Darby W, *J. Phys. Chem.*, 1963, **67**, 1451

51 Al-Mamouri M, Edwards P P, Greaves C, Slaski M, *Nature*, 1994, **369**, 382

52 Bednorz J G, Müller K A, *Z. Phys. B.*, 1986, **64** 189

53 Weller M T, *Inorganic Materials Chemistry, Oxford Chemistry Primers*, Oxford University Press, Oxford, 1996

54 Ruddlesden S N, Popper P, *Acta. Crystallogr.*, 1958, **11**, 54

55 Lacorre P, *J. Solid State Chem.*, 1992, **97**, 495

56 Retoux R, Rodriguez-Carvajal J, P. Lacorre, *J. Solid State Chem.*, 1998, **140**, 307

57 Siwen L, Yufang R, *Mat. Res. Bull.*, 1994, **29**, 993

58 Brisi C, Valliano M, Abbattista F, *J. Less-Common Metals*, 1981, **79**, 215

59 Dann S E, Currie D B, Weller M T, *J. Solid State Chem.*, 1992, **97**, 179

60 Babel D, Herdtweck E., *Z. Anorg Allg. Chem.*, 1982, **487**, 75

61 Babel D, Herdtweck E., *Z. Anorg Allg. Chem.*, 1981, **474**, 113

62 Babel D, Herdtweck E., *Z. Kristallogr.*, 1980, **153**, 189

63 Seifert H J, Koknat F W *Z. Anorg Allg. Chem.*, 1965, **341**, 269
64 Goodyear J, Ali E M, Sutherland H H, *Acta Crystallogr., Sect. B: Struct. Sci.*, 1978, **34**, 2617
65 Goodyear J, Ali E M, Sutherland H H, *Acta Crystallogr., Sect. B: Struct. Sci.*, 1982, **38**, 600
66 Leib W, Muller -Buschbaum H K, *Z. Anorg. Allg. Chem.*, 1984, **518**, 115
67 Gutau W, Muller-Buschabaum H K, *Z. Anorg Allg. Chem.*, 1990, **584**, 125
68 McGlothlin N, Ho D, Cava R J, *Mater. Res. Bull.*, 2000, **35**, 1035
69 Abed M, Muller-Buschbaum H K, *Z. Anorg. Allg. Chem.*, 1991, **592** , 73
70 Abed M, Muller-Buschbaum H K, *J. Alloys and Compd.*, 1992, **183**, 24
71 Sowa T, Hiratani M, Miyauchi K, *J. Solid State Chem.*, 1990, **84**, 178
72 Boje J, Muller-Buschabaum H K, *Z. Anorg. Allg. Chem.*, 1991, **592** , 73
73 Knee C S, Weller M T, *Chem. Commun.*, 2002, 256
74 Breard Y, Michel C, Maignan A, Studer F, Raveau B, *Chem. Mater.*, 2003, **15**, 1273
75 Baszczuk A, Wolcyrz M, Zygmunt A, *J. Alloys Compd.*, 2003, **360**, 1
76 Yamaura K, Huang Q, Lynn J W, Erwin R W, Cava R J, *J. Solid State Chem.*, 2000, **152**, 374
77 Bréard Y, Michel C, Hervieu M, Nguyen N, Studer F, Maignan A, Raveau B, Bourée F, *J. Solid State Chem.*, 2003, **170**, 424
78 Tobias G, Oro-Sole J, Beltran-Porter D, Fuertes A, *Crys. Eng.*, 2002, **5,** 479
79 Goga M, Seshadri R, Ksenofontov V, Gütlich P, Tremel W, *Chem. Commun.*, 1999, 979
80 Denis S G, Clarke S J, *Chem. Commun.*, 2001, 2356
81 Rao C N R, Gopalakrischnan J, *New Direction in Solid State Chemistry*, 2nd ed, Cambridge University Press, New York, 270, 1997
82 Battle P D, Gibb T C Lightfoot P, *J. Solid State Chem.*, 1989, **79**, 75
83 Poeppelmeier K R, Leonowicz M E, Longo J M, *J. Solid State Chem.*, 1982, **44**, 89
84 Battle P D, Gibb T C, Lightfoot P, *J. Solid State Chem.*, 1990, **84**, 237
85 Bordet P, Chaillout C, Caponi J J, Chenavas J, Marezio M, *Nature*, 1987, **327**, 687
86 Wu M K, Ashburn J R, Torng C J, Meng R L, Gao L, Huang Z J, Wang Y Q, Chu C W, *Phys. Rev. Lett.*, 1987, **58**, 909
87 Siegrist T, Zahurah S M, Murphy D W, Roth R S, *Nature,* 1988, **334**, 231
88 West A R, *Basic Solid State Chemistry*, Wiley, New York, 1996
89 Cava R J, *J. Am. Ceram. Soc.*, 2000, **83**, 1, 5
90 Hiroi Z, Takano M, Azuma M, Takeda Y, Bando Y, *Physica C*, 1991, **185-189**, 775
91 Hiroi Z, Takano M, Azuma M, Takeda Y, *Nature*, 1993, **364**, 315
92 R Hoppe, H Rieck, *Z. Anorg. Allg. Chem.*, 1970, **379**, 157
93 Michel C, Er-Rakho L, Raveau B, *J. Solid State Chem.*, 1981, **39**, 161
94 Schmitz-DuMont O, Kasper H, *Z. Anorg. Allg. Chem.*, 1965, **341**, 252
95 Effenger H, *J. Solid State Chem.*, 1988, **73**, 118

96 Herdtweck E, Babel D, *Z. Anorg. Allg. Chem.*, 1981, **474**, 113

97 Wahl K, Klemm W, *Z. Anorg. Allg. Chem.*, 1952, **270**, 69

98 Goodenough J B, Demazeau G, Pouchard M, Magen-Muller P, *J. Solid State Chem.*, 1973, **8**, 325

99 Robin M B, Day P, *Adv. Inorg. Radiochem.,* 1967, **10**, 247

100 Zachariasen W H, *Acta Crystallogr.*, 1963, **16**, 385

101 Brown I D, *Acta Crystallogr. Sect. B*, 1977, **33**, 1305

102 Greenwood N N, Earnshaw A, Chemistry of the Elements, 1st Edition, Pergamon Press, Oxford, 1984

103 Hoppe R, Hofmann B, *Z. Anorg. Allg. Chem.*, 1977, **436**, 65

104 Moews P C, *Inorg. Chem.*, 1966, **5**, 5

105 Gupta M P, Milledge H J, McCarthy A E, *Acta Crystallogr. B*, 1974, 30, 656

106 Raekelboom E A, Hector A L, Owen J, Vitins G, Weller M T, *Chem. Mater.*, 2001, **13**, 4618

107 Mahesh R, Mahendiran R, Raychaudhuri A K, Rao C N R, *J. Solid State Chem.*, 1995, **114**, 297

108 Rao C N R, *J. Phys. Chem. B*, 2000, **104**, 5877

109 Zachariasen W H, *Acta Crystallogr.*, 1963, 16, 385

110 Brown I D, *Acta Crystallogr. Sect. B*, 1977, **33**, 1305

111 Shaplygin I S, Lazarov V B, *J. Russ. Inorg. Chem.,* 1985, **30**, 3214

112 Lehmann H, Muller-Buschbaum H K, *Z. Anorg. Allg. Chem.*, 1980, **470**, 59

113 Boyle T J, Ingersoll D, Alan T M, Tafoya C J, Rodriguez M A, Vanheusden K, Doughty D H, *Chem. Mater.,* 1998, **10**, 2270

114 Geremia S, Nardin G, Mosca R, Randaccio L, Zangrando E, *Solid State Commun.*, 1989, **72**, 333

115 Dann S E, Weller M T, *J. Solid State Chem.,*1995, **115**, 499

116 Takeda Y, Kanno R, Takeda T, Yammamoto O, *Z. Anorg. Allg. Chem.,* 1986, **540**, 259

117 Yamazoe N, Furukawa S, Teraoka Y, Seiyama T, *Chem. Lett.*, 1982, 2019

118 Brachtel G, Hoppe R, *Z. Anorg. Allg. Chem.*, 1978, **446**, 64

119 Karen P, Kjekshus A, Huang Q, Lynn J W, Rosov N, Sora I N, Karen V L, Mighell A D, Santoro A, 1998, *J. Solid State Chem.*, **136**, 21

120 Knee CS, Weller MT, J. Mater. Chem., 2001, **11**, 2350

121 Li R K, Physica C, 1997, **277**, 252

122 Cotton F A, Wilkinson G, Advanced Inorganic Chemistry, 5th Edition, John Wiley & Sons, New York, 1988

123 Onnes H K, *Leiden. Comm.*, 1911 **124C**

124 Shriver D F, Atkins P, Langford C H, *Inorganic Chemistry*, 2nd Edition, Oxford University Press, Oxford, 1995

125 Schilling A, Cantoni M, Cuo J D, Ott H R, *Nature*, 1993, **363**, 56

126 Andres K, Wudl F, McWhan D B, Thomas G A, Nalewajek D, Stevens A L, *Phys. Rev. Lett.*, 1980, **45**, 1449

127 Geiser U, Schultz A J, Wang H H, Watkins D M, Stupka D L, Williams J M, Schirber J E, Overmyer D L, Jung D, Novoa J J, Whangbo M H, *Physica C*, 1991, **174** (4-6), 475

128 Kroto H W, Heath J R, O'Brien S C, Curl R F, Smalley R E, *Nature*, 1985, **318**, 162

129 Hebard A F, Rosseinski M J, Haddon R C, Murphy D W, Glarum S H, Palstra T T M, Ramirez A P, Kortan A R, *Nature*, 1991, **350**, 600

130 Nagamatsu N, Nakagawa N, Muranaka T, Zenitani Y, Akimitsu J, *Nature*, 2001, **410**, 63

131 Bud'ko S. L, Lapertot G, Petrovic C, Cunningham C. E, Anderson N, Canfield P. C, *Phys. Rev. Lett*, **86**, 9, 1877

132 Grovenor C, *IRC in Superconductivity, Annual Winter School 2001 lecture*, "Superconducting Materials"

133 Paulus E F, Yehia I, Fuess H, Rodriguez J, Vogt T, Stroebel J, Klauda M, Saemann-Ischenko G, Solid State Commun., 1990, **73**, 791

134 Li R, Zhu Y, Xu C, Chen Z, Qian Y, Fan C, *J. Solid State Chem.*, 1991, **94**, 206

135 Cox D E, Torardi C C, Subramanian M A, Gopalakrischnan J, Sleight A W, *Phys. Rev. B.*, 1988, **38**, 6624

136 Ekstrom M, Hartmann O, Karlsson E, Lidstrom E, Granberg P, Nygren M, *Phys. Rev. B*, 2001, **64** 184522

137 Chatterjee L, *Phys. Status Solidi A*, 2003, **196**, 267

138 Ramirez A P, *J. Phys.: Condens. Matter*, 1997, **9**, 8171

139 von Helmolt R, Wecker J, Holzapfel B, Schultz L,, Samwer K, *Phys. Rev. Lett.*, 1993, **71**, 2331

140 Booth C H, Bridges F, Kwei G H, Lawrence J M, Cornelius A L, Neumeier J J, *Phys. Rev. Lett.*, 1998, **80**, 853

141 Battle P, *RSC Annual Conference 2001 lecture*, "Novel Magnetic Behaviour in Ruddlesden-Popper Manganates"

142 Raveau B, Maignan A, Martin C, Caignaert V, Hervieu M, Simon C, *Abstr. Pap. Amer. Chem. Soc.*, Apr 13 1997, **213**: 701-INOR, Part 2

Chapter Two

Experimental Techniques

2.1 Introduction

This work has used a range of synthetic and analytical techniques to produce and characterise a variety of inorganic solid state compounds.

During the course of this research a variety of synthetic methods have been used, both traditional solid state methods and "sealed tube" techniques have predominated, but high-pressure and sol-gel techniques were employed as well.

The most commonly used technique for analysis was Powder X-ray Diffraction (PXD), but although complete structures can be derived from data collected using this technique it is often necessary to gain complementary information. Such additional data has been acquired from Powder Neutron Diffraction (PND), Thermogravimetric Analysis (TGA), Differential Thermal Analysis (DTA) and Infrared Spectroscopy (IR), and used to help fully determine physical structure, magnetic structure and phase behaviour.

2.2 Synthetic Techniques

2.2.1 Traditional Solid State Method

Dry reagents, commonly metal salts, oxides and carbonates, are ground together in an agate pestle and mortar. Acetone can be used as an inert solvent to create a slurry which aids particle dispersion and thus mixing of reagents. When the acetone has evaporated the mixed powder can be transferred to a high-temperature stable alumina crucible then placed in a furnace to be annealed. Multiple heat treatments of increasing temperature are often used. Regrinding and/or pelletising the reactants between each treatment helps increase contact between the reactant species and thus help the reaction progress.

2.2.2 "Sealed Tube" Solid State Method

This technique begins in the same way as the traditional solid state method with the appropriate starting materials being ground together in a pestle and mortar; however this stage is usually carried out in a N_2 glove box to avoid

moisture being absorbed by hygroscopic reactants such as $SrCl_2$. The dry reactant mixture is transferred to a silica tube using a funnel with a long stem, and the tube sealed using a blowtorch after being thoroughly evacuated on a vacuum line. The sealed tube is then placed within a section of alumina furnace tubing and heated from room temperature to the desired reaction temperature. After a set period of time the furnace is turned off and the tube allowed to cool back to room temperature. (This careful heating/cooling regime is designed to prevent the tube from breaking, whilst an alumina jacket is used as a precautionary measure to minimise damage should the tube break). As the reactants are heated under vacuum no redox reactions can take place, and thus using this technique allows metal oxidation states to be stabilised that would otherwise alter on being heated in air.

Often a crucible will be used to contain the starting materials within the tube; this is done to prevent them from reacting with the silica tube itself. It is also worth noting that the reactants used with this technique must be of a form that does not decompose at high temperature (e.g. oxides not carbonates). Any reactant that gave off gas at raised temperatures could cause the tube to explode, which would be both dangerous and prevent the reaction from proceeding as planned.

2.2.3 Sol-Gel Based Methods

The sol-gel technique involves the production of ceramic materials by the preparation of a sol, gelation of the sol, then removal of the solvent (see Figure 2.2.3a).

Inorganic or organic precursors (e.g. nitrates or alkoxides) of metals are dissolved in a solvent to form a suspension in which gravitational forces are negligible and molecular species can exist in isolation. A gel forms when the sol is heated slowly to form macroscopic species as the solvent evaporates. The transformation from amorphous gel to crystalline solid occurs upon firing (as with the ceramic method above).

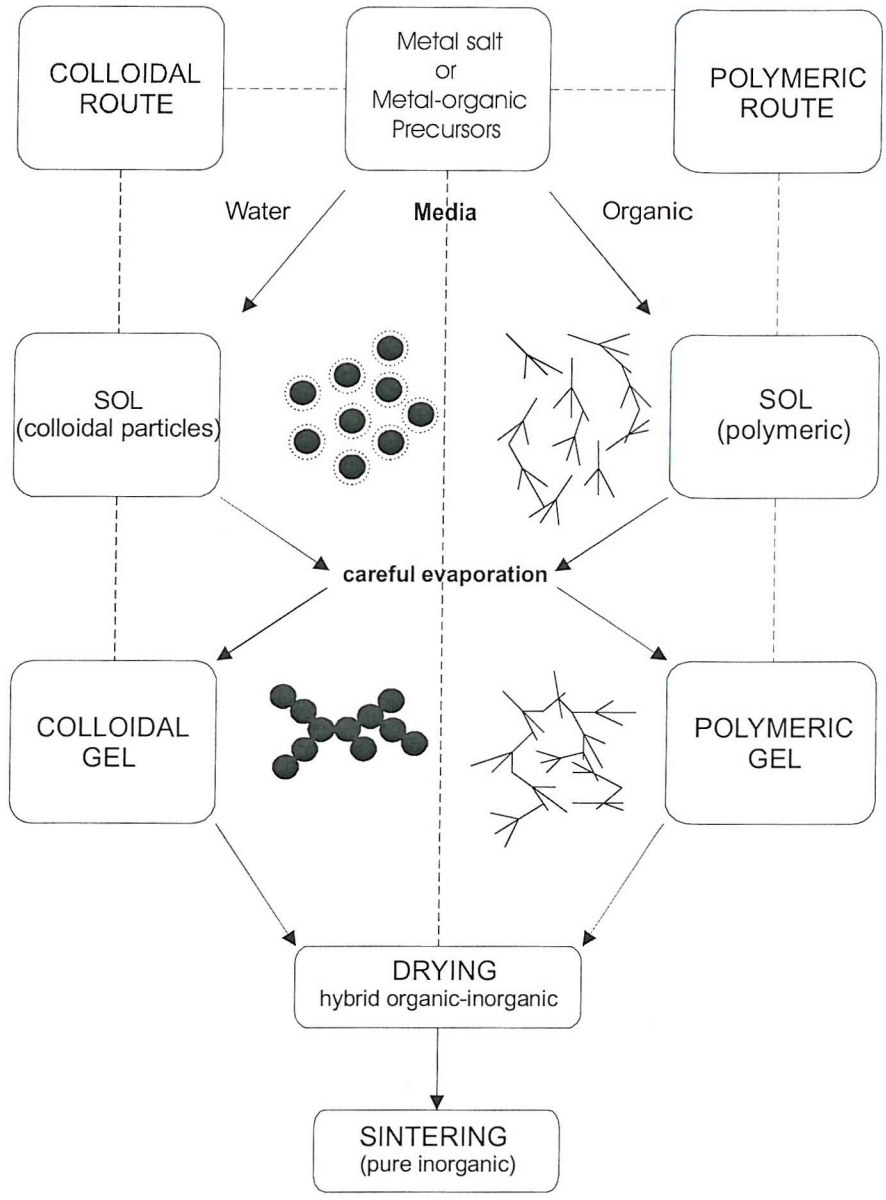

Figure 2.2.3a Schematic Representation of Sol-Gel Synthesis [1]

Sol-gel based processes can aid the production of homogenous, pure materials at low temperatures and, sometimes, the formation of new materials that cannot otherwise be made. This is due to several factors; as the starting materials are dissolved in solvents atomic level mixing occurs, this in turn means that lower reaction temperatures may be used which can result in the stabilisation of low-temperature phases and often results in smaller particle sizes as well. However, sol-gel syntheses can be long and costly processes and at times retain by-products and/or precursors thus polluting the final product.

2.3 Analytical Techniques

2.3.1 Powder X-ray Diffraction (PXD)

2.3.1.1 Introduction and Theory

This non-destructive technique has become the primary analytical technique of the solid state chemist. PXD readily allows crystalline materials to be characterised and sample purity to be ascertained, whilst a more detailed study allows for the observation of phase transitions, measurement of particle size, refinement of structures and identification of crystal defects and disorder [2].

This research study has relied heavily upon using this method of analysis to enable identification of synthetic products and determination of the purity of the products formed. Initial analysis of PXD data involves comparing the diffraction pattern collected to those stored on the JCPDS Powder Diffraction File [3]. This database of thousands of patterns is searched for a match to the profile collected; specifying which elements should be present in the compound refines this search. Once a good quality sample of a compound is made PXD can be used to accurately determine lattice parameters and fully resolve the structure using the Rietveld Method as explained in section 2.3.3.

When X-rays encounter matter they interact with the electrons present within it and are scattered by them as a result. A crystalline solid has atoms arranged in regular repeating lattices with interatomic distances comparable to the wavelength of X-rays, ~ 1Å, which in effect means a three dimensional diffraction grating is formed from the regular array of scattering centres. As a consequence an interference pattern distinctive to a structure is created when the X-rays encountering it are scattered in a particular way by the specific arrangement of atoms.

The diffraction of X-rays is commonly modelled using Bragg's Law [4] in which parallel planes of atoms within a crystal, separated by distance d, scatter the parallel X-ray beams that hit them with an incidence angle, θ. A simplified representation of this can be seen in Figure 2.3.1a.

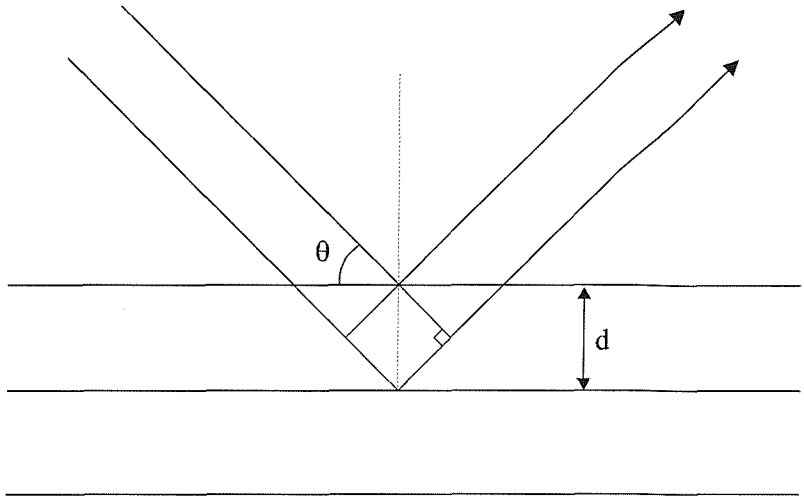

Figure 2.3.1a Schematic representation of parallel planes of atoms within a crystal interacting with X-ray radiation.

Constructive interference between the beams only results when the pathlength difference between them is equivalent to an integral number of wavelengths. This relationship forms the Bragg Equation:

$$n\lambda = 2d \sin \theta$$

Equation 2.3.1i

where n = 1,2,3,...

λ = wavelength of incident x-rays.

d = separation of planes ('d-spacing')

θ = incident angle of the x-rays.

The intensity of a particular reflection varies depending upon a range of factors. The scattering power of the atoms within a plane is the greatest factor controlling the intensity of diffraction maxima. The scattering power of an atom is proportional to the atom's atomic number (i.e. the number of electrons, as this is what interacts with the X-rays) and the higher the number the greater the atom's scattering power. Other factors to affect observed intensities include temperature factors, absorption factors, multiplicities (the number of reflections contributing to an observed maxima) and preferred orientation.

It is worth noting that not all planes within a crystalline substance will result in an observed intensity in the diffraction pattern. Reflection conditions and systematic absences caused by symmetry elements inherent to a structure may prevent diffraction maxima from being observed.

2.3.1.2 Instrumentation

PXD data were collected on a Siemens D5000 or Bruker D85 diffractometer using a copper source and single crystal monochromator to produce Cu $K\alpha_1$ radiation (λ = 1.5406 Å). The sample to be analysed is mounted flush in a recessed sample holder made of aluminium or plastic, which is in turn mounted in the sample stage of the diffractometer. The sample rotates during the measurement at a constant angular velocity and the scintillation detector is rotated at twice the angular velocity.

To counteract the preferred orientation of crystallites within certain samples such samples are spun horizontally within their mounting to create an average view of the sample, thus reducing the effect of individual crystallites. Another problem that can be encountered when analysing samples using PXD is that certain compounds fluoresce when exposed to X-rays due to the metals contained within them. This leads to unclear diffraction patterns with high backgrounds. Fluorescence can be completely removed by operating the D85 diffractometer in reflection mode ($CuK\alpha_1$) employing a Si/Li solid-state detector (SOL-X, Baltic Scientific Instruments).

A schematic of the Siemens D5000 and Bruker D85 diffractometers is shown in Figure 2.3.1b:

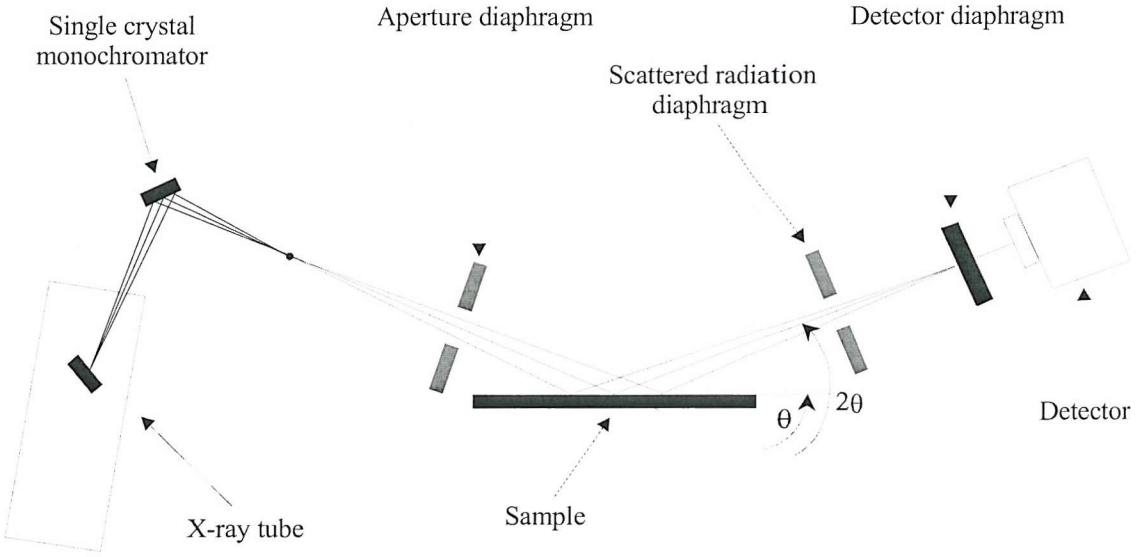

Figure 2.3.1b A Schematic of the D5000 and D85 Diffractometers

A computer controls each instrument, runs different collection programs and compiles the data for analysis and storage.

2.3.2 Powder Neutron Diffraction (PND)

2.3.2.1 Introduction and Theory

Powder neutron diffraction (PND) is another technique used in solid state chemistry that is very useful for analysing the structure of crystalline materials. The data collected using this technique is used in much the same way as with PXD but unlike X-rays, which are scattered by the electron cloud of an atom, neutrons are scattered by its nucleus. Thus the scattering power of elements towards neutrons can be quite different from those towards X-rays (as the values vary erratically), particularly as the scattering power of a nucleus is dependent on both potential scattering and resonant scattering.

The suitability of neutrons to the diffraction technique results from several properties including a wavelength comparable to atomic separation and an intrinsic magnetic moment, which allows both crystal and magnetic structures to be investigated.

PND is advantageous over PXD in a variety of ways and overcomes many of the problems intrinsic to X-ray diffraction. One problem commonly experienced with PXD is that light elements with low electron densities are difficult to detect due to the proportional relationship of scattering power with atomic number. In the case of neutrons, however, the atomic nuclei are responsible for the scattering and there is no simple dependence of neutron scattering power over atomic number making it easier to accurately determine light atoms' atomic parameters. This is of particular significance to this work as PND permits the accurate determination of oxygen positions in the presence of heavy elements such as lanthanides.

As the scattering power of a nucleus towards neutrons varies irregularly across the periodic table, at times adjacent elements can have vastly different scattering factors. This confers upon PND the ability to distinguish between neighbouring elements in the periodic table, which is not possible with PXD (as with a similar number of electrons the two elements would have almost identical scattering power). This advantage has been made use of in this study to differentiate between copper and manganese (see Chapter 3).

Another advantage of carrying out structural analysis using neutrons is that as neutrons point scatter due to their small size, that even at large diffraction

angles destructive interference is negligible. This eliminates the decrease in scattering power at high 2θ values as seen with PXD, allowing an accurate measurement of peak intensity across all 2θ values.

The high penetrating power of neutrons allows the sample to be heated or cooled during data collection as the material from which a furnace or cryostat is made will not prevent the neutrons passage. This permits in-situ study of phase transitions, low temperature structures, and often using low temperature data reduces thermal motion within a structure which facilitates more accurate structural determination.

Finally, neutron diffraction may also be used to study the magnetic structure of materials, as neutrons possess a magnetic dipole moment of their own. The unpaired electrons present in magnetic materials interact with the neutrons, giving rise to an additional scattering effect producing extra peaks in the observed pattern. These extra peaks represent the super structure formed by the positions of the magnetic atoms within the overall structure.

For these reasons, and despite the high cost and potential safety hazard inherent in a powerful ionising radiation source, neutron diffraction proves to be an invaluable tool in the detailed study of many materials.

There are two principal sources of neutron radiation suitable for diffraction techniques: constant wavelength and time of flight (TOF). The latter was the technique used for this research and thus the theory behind this technique is explained below.

Neutrons, due to their wave-particle duality, may be used for diffraction experiments in a similar way to X-rays. The wavelength of a given neutron is governed by the de Broglie equation [5]:

$$\lambda = \frac{h}{mv}$$

Equation 2.3.2a

where λ = wavelength

h = Planck's constant

m = mass of a neutron

v = velocity of a neutron

A synchrotron spallation source provides pulses of neutron radiation across a range of wavelengths. The diffracted neutrons are separated according to their time of flight by fixed angle detectors, and therefore, over a fixed distance, they are separated by their wavelength. Usually in a diffraction experiment the variables of the Bragg equation are d and θ at fixed λ; in a TOF experiment this is changed so that λ and d are variables at fixed θ.

If a primary flight path (moderator to sample) is a distance L_1, a secondary flight path (sample to detector) is L_2 and the corresponding times of flight are t_1 and t_2, then;

$$\frac{h}{m_n}.\left[\frac{t_1+t_2}{L_1+L_2}\right] = 2d\sin\theta$$

Equation 2.3.2b

Therefore with a total neutron flight path L ($L_1 + L_2 = L$) and total time of flight t ($t_1 + t_2 = t$), then:

$$t = 2dL\left(\frac{m_n}{h}\right)\sin\theta$$

$$\therefore t \propto d$$

Equation 2.3.2c

Consequently, for a 12 m instrument like POLARIS, a 1 Å d-spacing reflection will be detected in a backscattering bank at a TOF of ~5000 μs.

2.3.2.2 Instrumentation

TOF PND data were collected on the POLARIS, HRPD and GEM instruments at the ISIS facility (a synchrotron spallation source) at the Rutherford Appleton Laboratory (R.A.L.), Oxfordshire.

The POLARIS instrument receives short pulses (<90 μs) of neutrons from the proton spallation of a uranium or tantalum target, with neutrons of wavelengths down to 0.2 Å suitable for diffraction. The initial burst of neutrons is slowed in a gadolinium poisoned water monochromator at 295 K to give the required tight neutron pulse over a wide range of wavelengths. A schematic representation of POLARIS is given in Figure 2.3.2ai.

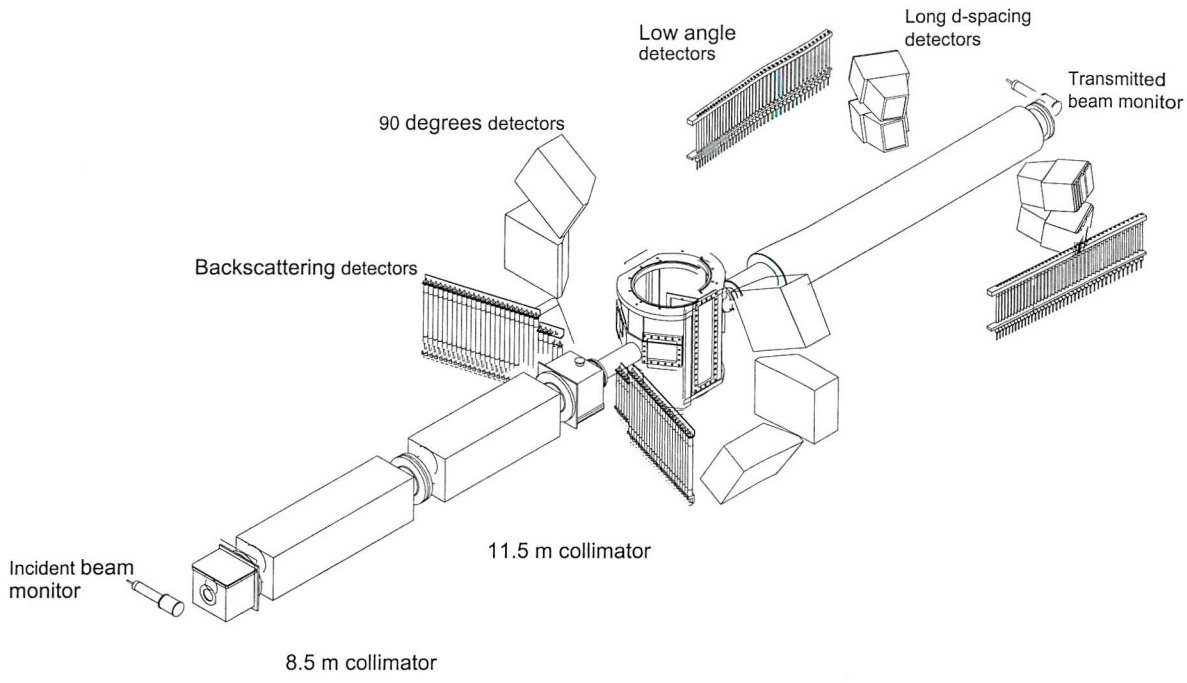

Figure 2.3.2ai Schematic of the POLARIS Diffractometer [6].

The samples were loaded in vanadium cans of 6 – 12 mm overall diameter, and placed within an evacuated sample chamber. On POLARIS backscattered neutrons are detected by 38 ^{3}He detectors giving a resolution of $\Delta d/d \sim 5 \times 10^3$ and a d-spacing range of 0.2 – 3.2 Å. Typical data collection periods on POLARIS for samples of 1 – 2 g were 2 – 4 hours depending on the sample.

HRPD, the High Resolution Powder Diffractometer, is situated approx. 100 m from the ISIS target at the end of a neutron guide and uses a liquid methane moderator to provide an incident flux out to a maximum wavelength of 10 – 12 Å. The highest resolution backscattering data may be recorded out to d-spacings of approx. 5 Å whilst complementary detectors at 90°, and low angles,

extend the measurable d-spacing range, albeit at lower resolution, to beyond 20 Å. A schematic representation of HRPD is given in Figure 2.3.2aii.

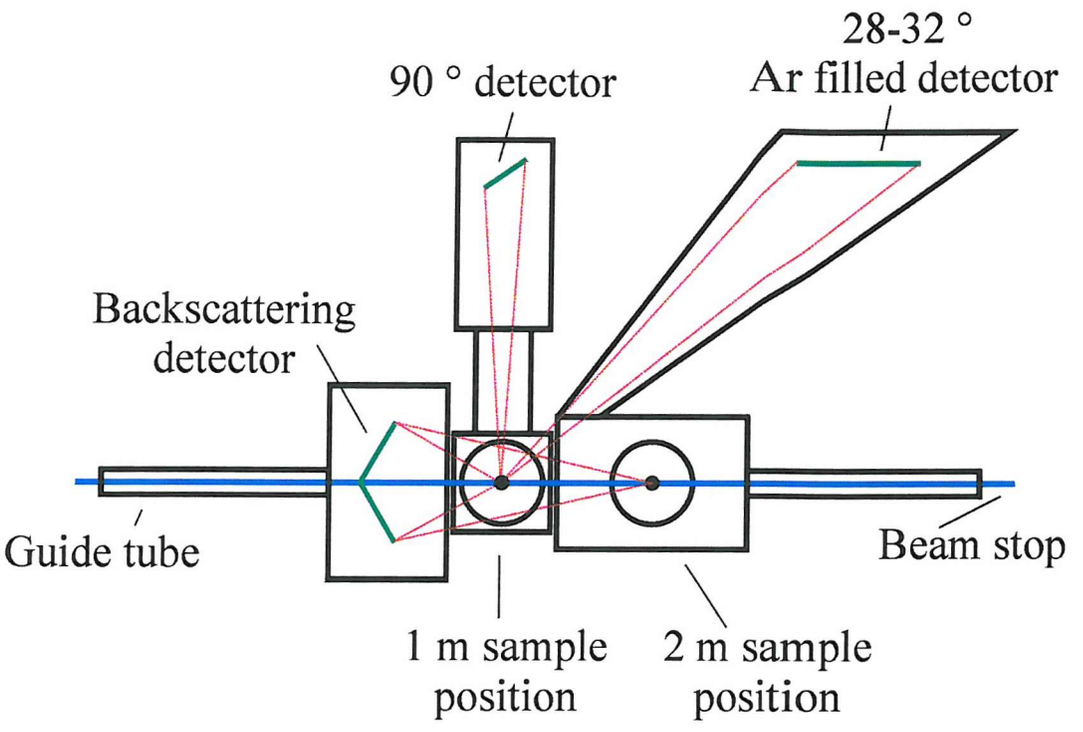

Figure 2.3.2aii Schematic of the HRPD diffractometer [6].

The samples were loaded in square vanadium slab cans measuring 2 x 13 x 23 mm, and placed within an evacuated sample chamber. On HRPD backscattered neutrons are detected by ZnS scintillator detectors giving a resolution of $\Delta d/d \sim 4 \times 10^{-4}$ over a wide d-spacing range. Due to the low flux intensity available at HRPD typical data collection periods are lengthy, and samples of approx. 1 g were measured for 12 hours.

GEM can be used to perform high flux intensity, high resolution experiments with a low background count; highly useful for the study of crystalline materials. The instrument comprises a primary flight path of 17 m and has seven detector banks, which give an overall detector area of approx. 10 m^2 covering a wide range in scattering angle from below 5° to170°. GEM has disc choppers for restricting the wavelength range and thus preventing frame overlap, and a nimonic chopper for reducing the contribution to the background from high energy neutrons. A schematic representation of GEM is given in Figure 2.3.2aiii.

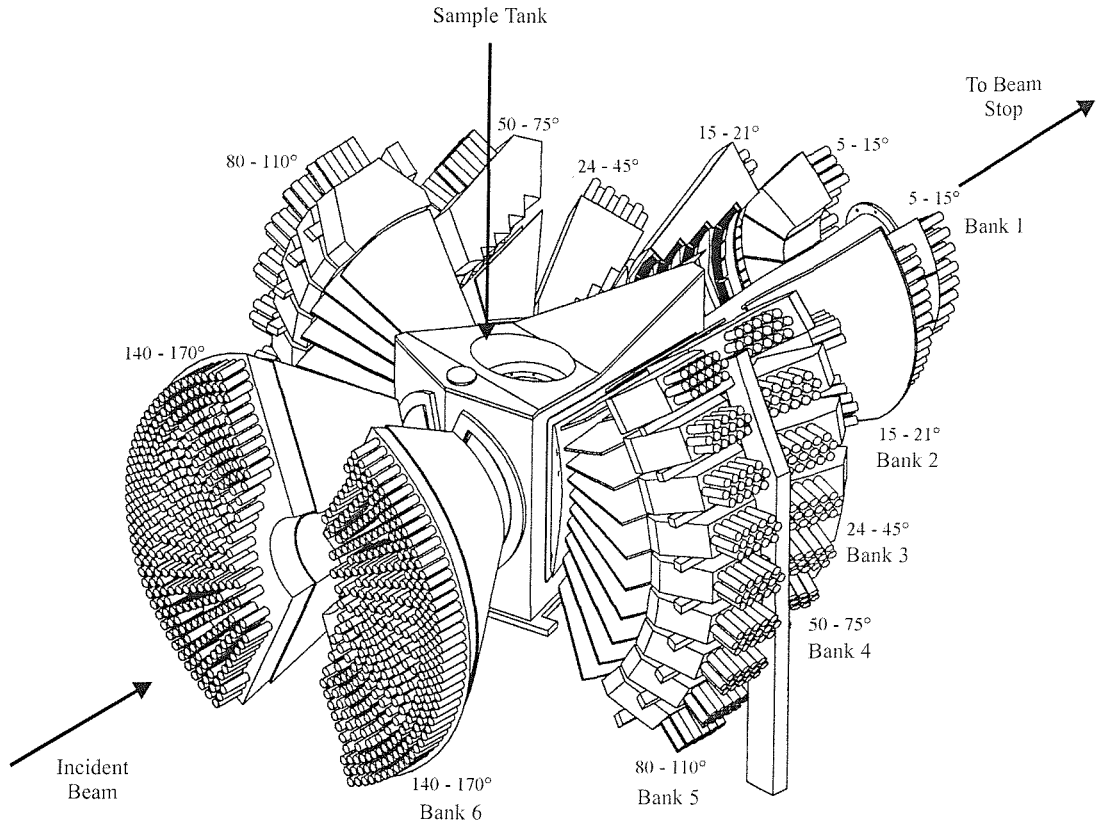

Figure 2.3.2aiii Schematic of the GEM diffractometer [6].

GEM has multiple ZnS scintillator detectors giving a resolution of $\Delta d/d = 2 - 3 \times 10^{-3}$ in backscattering and $\Delta d/d = 5 \times 10^{-3}$ at a scattering angle of 90° at all d-spacings. The combination of a high count rate and good resolution enables data to be collected in very short times and on small samples, thus typical data collection periods on GEM for samples of 0.5 – 1 g were 10 – 20 minutes depending on the sample.

2.3.3 The Rietveld Method

The previous two sections (2.3.1 and 2.3.2) dealt with the collection of PXD and T.O.F. PND data. The Rietveld refinement method [7] has been used to analyse the data collected and extract structural information from it, as will be described below.

Single crystal data is analysed using a least squares refinement of structure factors (or $|F|$ values) in relation to intensities obtained from the three-dimensional diffraction pattern. As powder diffraction data is displayed in two

dimensions it is not suited to refinement by the same methods used for single crystals. Much of the information needed to determine structure factors, and thus refine a structure, can be contained within overlapping peaks and as a result be too complex to distinguish.

H. M. Rietveld [8] was the first to propose that analysing the whole diffraction pattern at once could allow a structure to be determined using a method of profile refinement. This lead him to develop The Rietveld Method [9] which is based upon minimising the difference between the experimental data (in the form of an observed diffraction pattern) and a theoretical model by refining certain parameters. This minimisation is achieved through carrying out simultaneous least-squares refinements on the two groups of refineable parameters, the structural and profile parameters.

The structural parameters describe the contents of the unit cell and include the thermal displacement parameters (temperature factors), coordinates and occupancies of each atom. The profile parameters define the position, shape and full-width-at-half-maximum (FWHM) of each peak, the profile scale factor, lattice parameters, background coefficients, zero point error, phase fractions and preferred orientation correction.

Within this study the General Structural Analysis System (GSAS) [10] software package has been used to perform Rietveld refinements on data collected on both single wavelength powder X-ray diffractometers and time of flight neutron instruments. A typical refinement process would be carried out as follows.

An approximate structural model (often a closely related crystal structure) is entered into the program, including cell parameters, space group and atom positions. First of all scale and background parameters are refined, then lattice parameters and zero point error, in order to accurately position diffraction maxima. Preliminary refinement of peak shape parameters can then be performed. Next atom positions are located within the structure by allowing them to vary, which in turn alters the peak intensities and improves the peak shape. Thermal motion at the atom positions is then included in the refinement by allowing the isotropic temperature factors to vary. Anisotropic temperature factors can also be included in the refinement to improve the fit, however, their use is often only applicable to neutron diffraction data. Other additional parameters may also be included in the refinement if appropriate. These include the occupancy at atom sites (to allow for partial occupancies), phase fractions (in

the case of multiple phase samples) and the preferred orientation correction (useful when a noticeable alteration from expected peak heights is observed as can result from samples containing crystallites with either-plate or rod-like morphologies).

The progress of the refinement can be followed visually using the powplot function within the GSAS program. This function simultaneously displays the experimental data, the calculated profile and a difference plot. A perfect fit would result in a flat difference plot, but this is very rarely achieved.

The observed counts (Y_i^{obs}) are compared with the calculated counts (Y_i^{calc}) for each point ($2\theta_n$) on the profile of the model structure. The parameters of Y_n^{calc} are adjusted to minimise the function:

$$M_i = \Sigma \; W_i \left[Y_i^{obs} - Y_i^{calc} \right]^2$$

Equation 2.3.3a

where W_i = weighting factor = $(Y_i^{obs})^{-1}$

For PXD data, the calculated intensities Y_i^{calc} are determined from the structural model by summing the calculated contributions from neighbouring Bragg reflections (k) plus the background (b_i):

$$y_i^{calc} = s\sum_k L_k |F_k|^2 \varphi(2\theta_i - 2\theta_k) P_k A + y_{bi}$$

Equation 2.3.3b

where s = scale factor

L_k contains Lorentz polarisation and multiplicity factors

ϕ = reflection profile function

F_k = structure factor for the kth Bragg reflection

P_k = preferred orientation function

A = an absorption factor

y_{bi} = background intensity at ith step

Preferred orientation arises when there is a strong tendency for the crystallites to be ordered in a particular way. It is defined by:

$$P_k = \left[G_2 + (1 - G_2)exp(-G_1\alpha_k^2)\right]$$

Equation 2.3.3c

where G_1 and G_2 = refinable parameters

α_k = angle between the presumed cylindrical symmetry axis and the preferred orientation axis direction

The background intensity at $2\theta_i$ (y_{bi}) can be obtained from a specified, refineable background function, such as a fifth-order polynomial [11]:

$$y_{bi} = \sum_{m=0}^{5} B_m \left[\frac{2\theta_i}{BKPOS} - 1\right]^m$$

Equation 2.3.3d

where BKPOS = a user specified background position

Since the refinement method is based upon comparing intensities at every point it is fundamental, to the construction of the calculated profile, that the shape of the Bragg reflections, i.e. peak shape, is accurately described. The peak shape used in this work is the pseudo-Voigt function, a linear approximation to the convolution of the Gaussian and Lorentzian components of the peaks:

$$\eta L + (1 - \eta)G$$

Equation 2.3.3e

where L = the Lorentzian

G = the Gaussian contributions to the peak shape

η = the mixing parameter

η has been shown to vary as a linear function of 2θ and can be modelled as:

$$\eta = N_A + N_B(2\theta)$$

Equation 2.3.3f

where N_A and N_B = refinable parameters

The Gaussian (G) and Lorentzian (L) contributions to the peak shape are represented by the equations:

$$G = \frac{(4ln2)^{1/2}}{H_k\sqrt{\pi}} exp\left(-4ln2(2\theta_i - 2\theta_k)^2 / H_k^2\right)$$

Equation 2.3.3g

and

$$L = \frac{\frac{2}{\pi H_k} 1}{\left[1 + 4\frac{(2\theta_i - 2\theta_k)^2}{H_k^2}\right]}$$

Equation 2.3.3h

where $2\theta_k$ = the calculated position for the kth Bragg peak corrected for the counter zeropoint

H_k = the FWHM of the kth Bragg reflection

In the case of constant wavelength neutron diffraction, the H_k, of a peak has been shown to vary with the scattering angle $2\theta_k$ [12] and is modelled as:

$$H_k^2 = Utan^2\theta + Vtan\theta + W$$

Equation 2.3.3i

where U, V and W = the refinable parameters (both instrument and sample dependent).

Therefore, this formula can account for peak broadening effects resulting from particle size. However, it must be noted that when refining TOF PND and PXD data a more complex expression is used [7].

When a quanitative assessment of the goodness of fit is required (not just the qualitative pictorial representation offered by the histogram) the GSAS program can output a number of reliability indices. R_p is a parameter that measures agreement with the profile:

$$R_{profile} = R_p = 100\left[\frac{\sum_i \left|y_i^{obs} - y_i^{calc}\right|}{\sum_i y_i^{obs}}\right]$$

Equation 2.3.3j

R_e is of purely statistical significance:

$$R_{expected} = R_{exp} = 100\left[\frac{(N-P+C)}{\sum_i \omega_i (y_i^{obs})^2}\right]^{1/2}$$

Equation 2.3.3k

where N = number of observables

P = number of refinable parameters

C = number of constraints

R_{wp} is the most mathematically meaningful R factor, as the numerator is being minimised:

$$R_{wp} = 100\left[\frac{\sum_i \omega_i \left[y_i^{obs} - y_i^{calc}\right]^2}{\sum_i \omega_i \left[y_i^{obs}\right]^2}\right]^{1/2}$$

Equation 2.3.3l

χ^2 is a natural measure of good fit, it is normally minimised during the refinement process:

$$\chi^2 = \left[\frac{1}{N-P+C}\right]^2 \sum_i W_i \left|Y_i^{obs} - Y_i^{calc}\right|^2$$

$$= \left[\frac{R_{wp}}{R_e}\right]^2$$

Equation 2.3.3m

A good fit should result in the weighted R-factor approaching the statistically determined R-factor, i.e. χ^2 should approach unity.

A visual measure of goodness of fit is also of value, simply examining the difference line of a profile fit allows for an estimation to be made as to how good the structural model is.

Whatever the outcome of a refinement it is important to remember that the final model must make chemical sense. Bond lengths and angles extracted at the end of a refinement should be within reasonable limits; otherwise the model is of little value no matter how good the reliability indices may suggest it to be.

2.3.4 Thermal Analysis

2.3.4.1 Introduction and Theory

Thermal analysis involves the measurement of physical or chemical changes that occur as a result of temperature change. With respect to solid state chemistry research the properties examined are usually mass and thermodynamic events. These changes are measured by thermogravimetric analysis (TGA) and differential thermal analysis (DTA).

TGA records the weight change that occurs when a sample is heated under controlled conditions. The compound being tested is heated in a flow of gas (commonly air, 5% H_2 in N_2 or Ar) and any weight loss that results from decomposition, or loss of an adsorbed compound such as water, are measured.

DTA records the difference in temperature between the sample and an inert reference material. As the reference will not decompose or change phase over the temperature range of the equipment it enables comparison with such events occurring in the compound being tested. Whether the sample temperature is greater or less than the reference material allows the identification of exothermic and endothermic events, see Figure 2.3.4a:

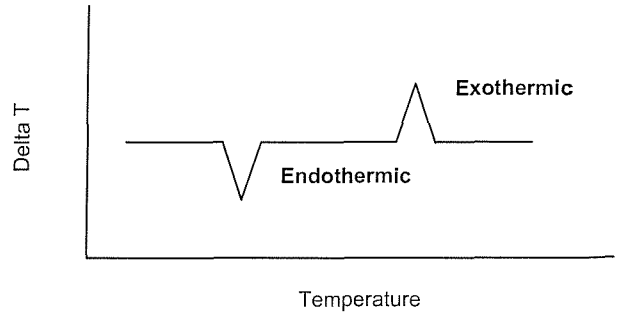

Figure 2.3.4a Example of DTA trace showing exothermic and endothermic events.

Collecting both TGA and DTA data at the same time enables the identification of thermal events that are associated with weight loss. Also, by studying the cooling, as well as the heating stage, a thermal change can be seen to be either reversible or irreversible. If an opposite thermal change results upon cooling this is a reversible change, if no change occurs then this is an irreversible change.

2.3.4.2 Instrumentation

Thermal analysis data were collected on a Polymer Laboratories STA 1500. This instrument can simultaneously record the TGA and DTA responses for a sample, over a temperature range of room temperature (RT) to 1500 °C, and with a gas flowing over the compound. For a schematic representation see Figure 2.3.4b:

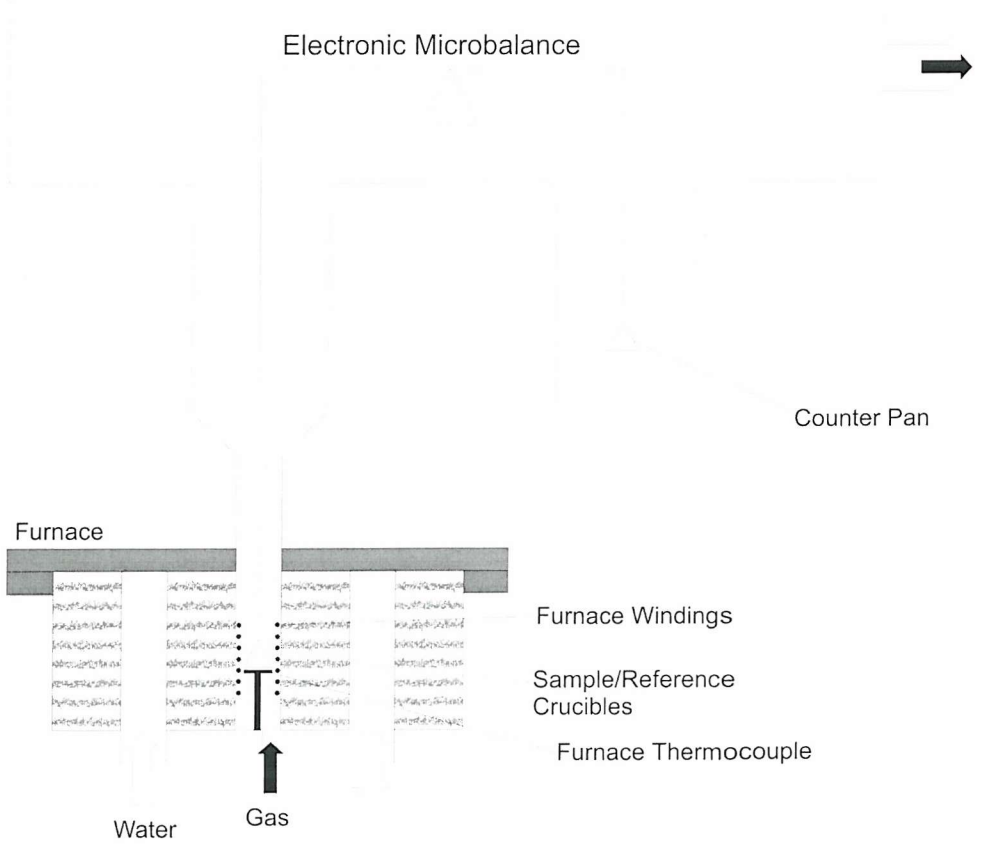

Figure 2.3.4b Schematic representation of PL STA 1500.

A computer controls the instrument and enables different programs to be run. A typical run involved heating approx. 15mg of sample from RT to 1000 °C at a rate of 10 °C per minute, holding that temperature for 10 minutes, then cooling to RT at 10 °C per minute. Every 3 seconds a data set is recorded, and at the end of a run the complete data set can be exported to be manipulated by other software programs at other computer terminals.

2.3.5 Infrared Spectroscopy (IR)

2.3.5.1 Introduction and Theory

The absorption of IR radiation at particular frequencies by bonded atoms within a solid can excite vibrational modes. Infra-red spectra are plots of the intensity of such absorptions as a function of the frequency of the incident radiation, which is usually collected from 4000 cm^{-1} to 400 cm^{-1} but can be varied over a greater range. Each vibration within an infra-red spectrum is characteristic to a particular molecular or lattice vibration and can thus be assigned to a part of the structure of the compound being studied. However a varied collection of absorptions may result from the overlapping of different vibrations and be difficult to interpret.

2.3.5.2 Instrumentation

IR Spectra were recorded using a Perkin Elmer Spectrum One system with a resolution of 1 cm^{-1}. The samples were diluted with pre-dried KBr (approximately 5 mg sample in 200 mg KBr), and placed in the specialised powder sample holder. Spectra were then recorded in reflectance mode.

2.3.6 Bond Valence Calculations

This is not an experimental technique but an analytical method by which an indication of the strength of a bond within a crystalline solid can be calculated. Bond valence calculations are used to assess the chemical viability of a structure ascertained from diffraction data, and to estimate the valence of an ion in a particular coordination environment.

Valence bond theory is used to describe bonding in organic and coordination compounds in the form of single, double or triple bonds. However, this cannot be used to explain the bonding in crystalline non-molecular inorganic materials when most structures have too few electrons to assign a pair to each bond. Thus Zachariasen [13] and Brown [14] developed an empirical approach, bond valence theory, which evaluates individual bond valences, and consequently sums them to produce a site valence. This is shown below in the form of the valence sum rule:

$$V_i = \sum_j S_{ij}$$

Equation 2.3.6a

where S_{ij} = valence of a bond between atoms i and j

V_I = valence of atom I

This method is based on bond strength being inversely proportional to bond length, with longer bonds implying a weaker interaction. Bond valence theory determines a valence for a particular atom from the observed bond lengths associated with its site. Therefore, in an inorganic material bond strength can be calculated from experimentally measured bond lengths. A correlation between bond lengths and valence has been established after examining a range of inorganic crystalline systems. This inverse relationship can be described by the expression:

$$S_{ij} = exp\left[\frac{R_o - R_{ij}}{B}\right]$$

Equation 2.3.6b

where R_{ij} = length of a bond around the ion

R_0 = variable empirically determined parameter, actual values used are those derived by Altermatt and Brown [15]

B = constant empirically determined parameter

A limitation of this method of analysis is that it assumes that the crystalline system is relaxed and not a rigid lattice. A large amount of structural strain compresses bond lengths leading to larger, "over bonded", valences. Conversely, stretched structures lead to longer bond lengths and 'under bonded'

sites. However in most cases the actual valence is within 0.2 of the calculated valence and thus gives a good indication of the bonding environment.

2.4 References

1 Brinker J, Scherer G W, Sol-Gel Science, the physics and chemistry of sol-gel processing, Academic Press, Inc., New York, 1990

2 West A R, Solid State Chemistry and its Applications, Wiley, Chichester, 1984

3 International Centre for Diffraction Data, 12 Campus Boulevard Newton Square, Pennsylvania, 19073 – 3273, U.S.A., 1995

4 Bragg W L, *Proc. Camb. Phil. Soc.*, 1913, **17**

5 Shriver D.F, Atkins P W, Langford C H, Inorganic Chemistry, Oxford University Press, Oxford, 11, 1994

6 www..isis.rl.ac.uk

7 Rietveld H M; *Acta Crystallogr.*, 1966b, **21**, A228, Rietveld H M; *J. Appl. Crystallogr.*, 1969b, **2**, 65

8 Rietveld H M; *Acta Crystallogr.*, 1967, **22**, 151

9 Rietveld H M; *J. Appl. Crystallogr.*, 1969, **2**, 65

10 Larson A C, von Dreele R B; General Structure Analysis System, Los Alamos National Laboratory LAUR, 1994, 86-748

11 Young R A, ed, The Rietveld Method, International Union of Crystallography, Oxford University Press, Oxford, 1995

12 Caglioti G, Paoletti A, Ricci F P, *Nucl. Instrum. Methods,* 1958, **35,** 223

13 Zachariasen W H, *Acta Crystallogr.*, 1963, **16**, 385

14 Brown I D, *Acta Crystallogr. B*, 1977, **33**, 1305

15 Altermatt D, Brown I D, *Acta Cryst.* 1985, **B41**, 240

Chapter Three

Synthesis and Structural Characterisation of $Ln_3Ba_2Mn_2Cu_2O_{12}$ Phases (Ln = Eu and Sm)

3.1 Introduction

The oxide chemistries of copper and manganese have recently commanded considerable attention due to the unusual electronic and magnetic properties exhibited by such materials. Much of this attention has been directed at two specific oxidation states Cu II and Mn III which are Jahn-Teller ions (d^9 and d^4 respectively). In terms of copper II chemistry the main thrust has been the synthesis of new high temperature superconducting compounds constructed from layers of corner sharing CuO_4 square planes of the formal stoichiometry CuO_2 [1]. The structures of these materials are all formally derived from the perovskite structure with various other layers interposed. These inter-cuprate sheets may be of other structure types, such as fluorite or 'rocksalt', but may also be perovskite based themselves as for example materials of the type $Gd_2Ba_2Ti_2Cu_2O_{12}$ [2]. With respect to Mn (III) chemistry the aim has been the formation of mixed valency Mn^{3+}/Mn^{4+} materials demonstrating magnetoresistance such as $Ln_{1-x}Ca_xMnO_3$ [3] and $LaSr_2Mn_2O_7$ [4]. Again these structures are based on perovskites although, unlike superconductor chemistry, a three dimensional component to the structure seems to be required for the observation of the property of interest.

The combination of manganese and copper in complex perovskite based structures has been achieved by Hervieu *et al.* [5] and studied in detail by Matsubara and co-workers [6,7,8]. Materials of the composition $Ln_3Ba_2Mn_2Cu_2O_{12}$ exist only for Ln = Sm, Eu, Gd and adopt the so-called intergrowth structure with perovskite and 'rocksalt' units. The structure, shown in Figure 3.1a, has K_2NiF_4 layers of the composition Ln_2MnO_4 alternating with layers of the formal composition $LnBa_2Cu_2MnO_8$.

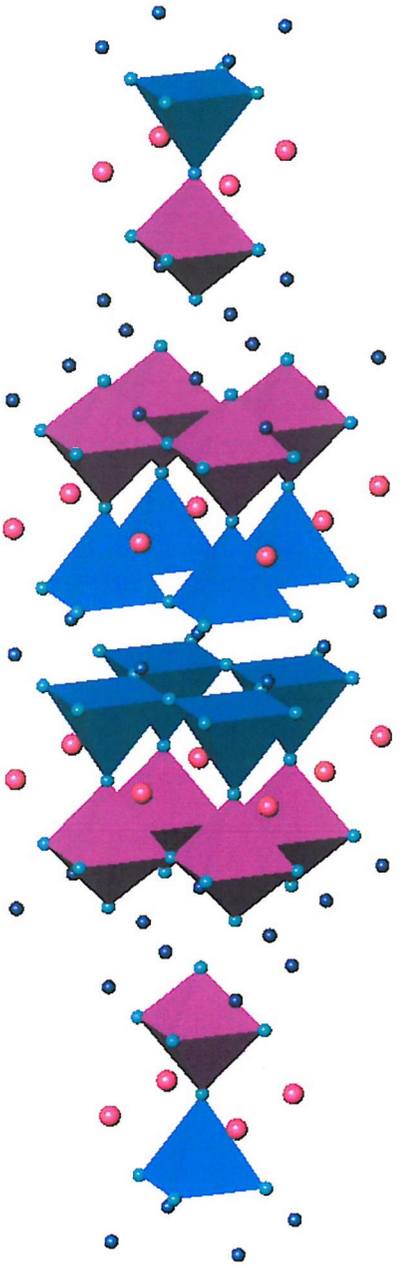

Figure 3.1a Structure of $Ln_3Ba_2Mn_2Cu_2O_{12}$

An overall oxygen stoichiometry of y = 0 in the formula $Ln_3Ba_2Mn_2Cu_2O_{12\pm y}$ produces a mixed Mn^{3+}/Mn^{4+} material with a manganese oxidation state typical of that observed in CMR materials. Cation substitutions have also been performed on this system forming, for example, $(Eu_{3-x}Ca_x)Ba_2Mn_{2-y}Sc_yCu_2O_{12}$ with the aim of oxidising copper into the superconducting range around $Cu^{2.25+}$, but all such phases were found to be semi-conducting [8].

All the structural analyses carried out on members of the $Ln_3Ba_2Mn_2Cu_2O_{12\pm y}$ systems until now have used powder X-ray diffraction methods or electron microscopy. Such techniques are relatively insensitive to oxygen distributions due to the presence of the heavier, strongly scattering elements. In addition the similarity of manganese and copper, and of lanthanide and barium ions, in terms of the scattering of X-rays makes distinguishing these elements extremely difficult. In order to rationalise the properties of the members of the $Ln_3Ba_2Mn_2Cu_2O_{12\pm y}$ system determinations of the distributions and levels of oxygen and the cations on their respective sub-lattices are obviously crucial. The technique of choice for such a study is powder neutron diffraction where oxygen is a strong neutron scatterer and significant scattering contrasts can exist between near-neighbour elements; e.g. Mn b = -3.7fm, Cu b = 7.7fm. However, the small range of lanthanides for which the $Ln_3Ba_2Mn_2Cu_2O_{12\pm y}$ phase forms normally precludes the use of neutron diffraction methods as naturally occurring isotopic composition Gd, Sm and Eu are all strong neutron absorbers. This problem may be overcome through the use of specific lanthanide isotopes that are only weakly absorbing such as ^{160}Gd, ^{154}Sm and ^{153}Eu. This work reports the structural study of $^{154}Sm_3Ba_2Mn_2Cu_2O_{12\pm y}$ and $^{153}Eu_3Ba_2Mn_2Cu_2O_{12\pm y}$, in as prepared and oxygen annealed forms, by high-resolution neutron diffraction.

3.2 Experimental Procedure

At first it was hoped that the problem of having to use neutron absorbing lanthanides within this compound type could be avoided by choosing atoms whose combined ionic radii would create an average radius close to that of those ions known to form the $Ln_3Ba_2Mn_2Cu_2O_{12}$ phase, i.e. gadolinium, samarium and europium. Thus a mixture of lanthanide starting materials was used within the syntheses in an attempt to form $NdDy_2Ba_2Mn_2Cu_2O_{12}$, $PrHo_2Ba_2Mn_2Cu_2O_{12}$ and $SmGdDyBa_2Mn_2Cu_2O_{12}$ following the method of Matsubara et al. [6, 7, 8].

Samples were prepared by intimately grinding together high purity stoichiometric mixtures of Nd_2O_3, Dy_2O_3, $BaCO_3$, Mn_2O_3 and CuO, Pr_6O_{11}, Ho_2O_3, $BaCO_3$, Mn_2O_3 and CuO or Sm_2O_3, Gd_2O_3, Dy_2O_3, $BaCO_3$, Mn_2O_3 and CuO (all 99.9% or better) and heating the reactants to 1000 °C for 4 hours, regrinding the intermediates and heating again to 1100 °C for a further 4 hours (for results, see Table 3.3.1a).

Synthetic work then concentrated on optimising the reaction conditions for the formation of pure phases of the single lanthanide phases.

Initially a conventional solid state synthetic method was tried with stoichiometric mixtures of Sm_2O_3 / Gd_2O_3 / Eu_2O_3, $BaCO_3$, Mn_2O_3 and CuO (all 99.9% or better), these were intimately ground together then heated at 1000 °C for 4 hours, reground and heated again to 1100 °C for a further 4 hours, and the final heating repeated until pure phase samples of each target phase were produced (for results, see Table 3.3.1b).

The synthesis of the related phases $Gd_3Ba_2(Mn_{1.5}Ru_{0.5})Cu_2O_{12}$ and $Eu_3Ba_{2-x}Sr_xMn_2Cu_2O_{12}$ (x = 0, 1, 2) was also attempted, using the same reaction conditions as above, from reaction mixtures containing stoichiometric amounts of Gd_2O_3, $BaCO_3$, Mn_2O_3, RuO_2 and CuO (all 99.9% or better, for results, see Table 3.3.1c) and Gd_2O_3, $BaCO_3$, $SrCO_3$, Mn_2O_3, and CuO (all 99.9% or better, for results, see Table 3.3.1d). These phases were attempted as it was thought that modifying the cations within the structure could cause interesting structural changes. The substitution of ruthenium for manganese was tried as such reactions have recently received attention within the literature [9], whilst the barium/strontium solid solution was tried as similar materials have been successfully made previously [10].

The effect of annealing under oxygen was observed repeating the syntheses with second thermal treatment occurring under a flow of oxygen (for results, see Table 3.3.1e).

In an effort to eradicate by-products without needing multiple thermal treatments at 1100 °C, two different methods were tried with the Sm_2O_3, $BaCO_3$, Mn_2O_3 and CuO (all 99.9% or better) reaction mixture. Firstly, a higher thermal treatment (for results, see Table 3.3.1f), secondly, the use of MnO_2 instead of Mn_2O_3 as the source of manganese (for results, see Table 3.3.1g) and thirdly, pelletising the reactants under 10 tonnes/cm^2 (for results, see Table 3.3.1h).

Finally, the optimised method of pelletising and multiple thermal treatments with intermediate careful grinding was used in the production of the valuable isotope containing phases. The europium and samarium phases were

the phases selected for study by PND, because the $Eu_3Ba_2Mn_2Cu_2O_{12}$ was the original example of this phase, whilst samarium was thought to be more useful for exploring the boundaries of phase formation. The phases $^{153}Eu_3Ba_2Mn_2Cu_2O_{12}$ and $^{154}Sm_3Ba_2Mn_2Cu_2O_{12}$ were synthesised in platinum crucibles from reaction mixtures using $^{153}Eu_2O_3$ and $^{154}Sm_2O_3$ (purchased from Trace Isotope at a level of >98.7 % purity) in place of the normal Eu_2O_3 and Sm_2O_3 (for results, see Table 3.3.1i and Table 3.3.1j).

After PND data had been collected for the phase $^{153}Eu_3Ba_2Mn_2Cu_2O_{12}$, the sample was annealed at 1050 °C for approximately 18 hours under a flow of oxygen, with slow cooling in oxygen to room temperature (for results, see Table 3.3.1i), and further PND data collected.

PXD data were used to confirm the purity of the phases formed, however full structural refinements of the $^{153}Eu_3Ba_2Mn_2Cu_2O_{12}$ and $^{154}Sm_3Ba_2Mn_2Cu_2O_{12}$ phases were carried out using the PND data.

Powder neutron diffraction data were collected from 500mg–1g samples on the diffractometer HRPD at Rutherford Appleton Laboratories at 298 K, 150 K and 2 K for the $^{153}Eu_3Ba_2Mn_2Cu_2O_{12}$ sample and 298 K only for the $^{154}Sm_3Ba_2Mn_2Cu_2O_{12}$ and oxygen annealed $^{153}Eu_3Ba_2Mn_2Cu_2O_{12}$ samples. Data collection times were 16 hours and data reduction was carried out using the standard methods; both back scattering and 90° data banks were included in the structure refinement, which employed the GSAS package [11]. Raw data from the europium containing samples were corrected for the effects of absorption due to the residual ^{151}Eu in the sample. For the samarium based material such data correction proved more difficult, due to the presence of the secondary phase, and the absorption correction was handled as far as possible in the data refinement.

3.3 Results, including Structural Refinement

3.3.1 Synthetic Results

Except in the case of the phase containing neutron adsorbing isotopes ($SmGdDyBa_2Mn_2Cu_2O_{12}$), it proved impossible to form the desired target phases with a mixture of complex oxides forming instead the phases detailed in table 3.3.1a.

Target Phase	Reagents	Heat Treatment	Products
$Nd_2DyBa_2Mn_2Cu_2O_{12}$	Nd_2O_3, Dy_2O_3, $BaCO_3$, Mn_2O_3 and CuO	1000 °C, 4h	50% of $DyBa_2Cu_3O_{6.96}$, 25% Dy_2O_3, 20% $Nd_{1.1}Ba_{1.9}Cu_3O_7$, and 5% $BaMnO_3$
		1100 °C, 4h	50% of $DyBa_2Cu_3O_{6.96}$, 25% Dy_2O_3, 20% $Nd_{1.1}Ba_{1.9}Cu_3O_7$, and 5% MnO
$PrHo_2Ba_2Mn_2Cu_2O_{12}$	Pr_6O_{11}, Ho_2O_3, $BaCO_3$, Mn_2O_3 and CuO	1000 °C, 4h	40% of $Ho_2Ba_4Cu_3O_{6.95}$, 20% $BaMnO_3$, 20% $Pr_{10}O_{18}$, 15% Ho_2O_3 and 5% $Ho_2Cu_2O_5$
		1100 °C, 4h	40% of $HoBa_2Cu_3O_7$, 30% Ho_2O_3, 10% $Pr_{10}O_{18}$, 10% $Ba_{0.92}Cu_{1.06}O_{2.14}$ and 10% $Ba_5Mn_4Ho_8O_{21}$
$SmGdDyBa_2Mn_2Cu_2O_{12}$	Sm_2O_3, Gd_2O_3, Dy_2O_3, BaO_3, Mn_2O_3 and CuO	1000 °C, 4h	35% of Dy_2O_3, 25% $Sm_{1.3}Ba_{1.7}Cu_3O_{7.6}$, 25% $GdBa_2Cu_{2.821}O_{6.74}$, 10% $BaMn_8O_{16}$ and 5% $DyMn_2O_5$
		1100 °C, 4h	Target phase

Table 3.3.1a Mixed lanthanide analogues of $Ln_3Ba_2Mn_2Cu_2O_{12}$

The conventional solid state method used to form the single lanthanide phases ($Gd_3Ba_2Mn_2Cu_2O_{12}$, $Sm_3Ba_2Mn_2Cu_2O_{12}$, $Eu_3Ba_2Mn_2Cu_2O_{12}$) produced pure samples after repeated thermal treatments:

Target Phase	Reagents	Heat Treatment	Products
$Gd_3Ba_2Mn_2Cu_2O_{12}$	Gd_2O_3, BaO_3, Mn_2O_3 and CuO	1000 °C, 4h	40% $GdBa_2Cu_3O_{6.99}$, 20% $BaMnO_{2.98}$, 15% $BaCuO_{2.4}$, 10% $GdBa_2Cu_3O_{6.84}$, 10% $CuGd_2O_4$ and 5% Mn_3O_4.
		1100 °C, 4h	100% of target phase
$Sm_3Ba_2Mn_2Cu_2O_{12}$	Sm_2O_3, $BaCO_3$, Mn_2O_3 and CuO	1000 °C, 4h	30% Sm_2CuO_4, 25% Mn_2O_3, 25% $SmBa_2Cu_3O_{6.11}$, 10% $BaCuO_4$ and 10% $Sm_{1.4}Ba_{1.6}Cu_3O_7$
		1100 °C, 4h	95% of target phase and 5% unidentified phase
		1100 °C, 4h	100% of target phase
$Eu_3Ba_2Mn_2Cu_2O_{12}$	Eu_2O_3, BaO_3, Mn_2O_3 and CuO	1000 °C, 4h	30% $EuBa_2Cu_3O_{6.13}$, 30% $Eu_{1.2}Ba_{1.8}Cu_3O_7$, 20% Mn_2O_3, 10% $CuEu_2O_4$ and 10% $BaMnO_3$.
		1100 °C, 4h,	100% of target phase

Table 3.3.1b Conventional synthesis of $Gd_3Ba_2Mn_2Cu_2O_{12}$, $Sm_3Ba_2Mn_2Cu_2O_{12}$ and $Eu_3Ba_2Mn_2Cu_2O_{12}$

Unfortunately the target phase $Gd_3Ba_2(Mn_{1.5}Ru_{0.5})Cu_2O_{12}$ did not form, a mixture of complex and simple oxides being obtained instead:

Target Phase	Reagents	Heat Treatment	Products
$Gd_3Ba_2(Mn_{1.5}Ru_{0.5})Cu_2O_{12}$	Gd_2O_3, $BaCO_3$, Mn_2O_3, RuO_2 and CuO	1000 °C, 4h	30% of $Gd_2Ba_4Cu_{2.821}O_{6.74}$, 30% $Gd_2CuO_{3.98}$, 10% $BaMnO_3$, 10% $Ba_3GdRu_2O_9$, 10% BaO and 10% Mn_3O_4
		1100 °C, 4h	30% of $Gd_2Ba_4Cu_{2.821}O_{6.74}$, 30% $Gd_2CuO_{3.98}$, 20% $Ba_3GdRu_2O_9$, , 10% Mn_3O_4 10% $BaMnO_3$ and 5% BaO

Table 3.3.1c Attempted synthesis of $Gd_3Ba_2(Mn_{1.5}Ru_{0.5})Cu_2O_{12}$

Once again the desired barium/strontium solid solution phases ($Eu_3Ba_{2-x}Sr_xMn_2Cu_2O_{12}$) did not form, a small amount of $Eu_3Ba_2Mn_2Cu_2O_{12}$ formed when barium was present alongside $Eu_{2-x}Ba_xCu_3O_{7-y}$ and a few simple oxides, whilst only binary oxides formed from the attempted synthesis of $Eu_3Sr_2Mn_2Cu_2O_{12}$:

Target Phase	Reagents	Heat Treatment	Products
$Eu_3Ba_2Mn_2Cu_2O_{12}$	Eu_2O_3, $BaCO_3$, Mn_2O_3 and CuO	1000 °C, 4h	30% $EuBa_2Cu_3O_{6.13}$, 30% $Eu_{1.2}Ba_{1.8}Cu_3O_7$, 20% Mn_2O_3, 10% $CuEu_2O_4$ and 10% $BaMnO_3$.
		1100 °C, 4h	70% of target phase, 15% $Eu_{1.2}Ba_{1.8}Cu_3O_{6.67}$, 10% Mn_2O_3 and 5% BaO_2.

$Eu_3BaSrMn_2Cu_2O_{12}$	Eu_2O_3, $BaCO_3$, $SrCO_3$, Mn_2O_3 and CuO	1000 °C, 4h	25% $Eu_{1.2}Ba_{1.8}Cu_3O_7$, 25% $SrMnO_{2.69}$, 20% $SrMnO_3$, 20% $Ba_3Cu_6Eu_3O_{14.1}$ and 10% Cu_2O.
		1100 °C, 4h	60% $Eu_3Ba_2Mn_2Cu_2O_{12}$, 30% $BaSrEuCuO_{6+x}$, 5% BaO and 5% SrO_2.
$Eu_3Sr_2Mn_2Cu_2O_{12}$	Eu_2O_3, $SrCO_3$, Mn_2O_3 and CuO	1000 °C, 4h	50% Eu_2CuO_4, 30% $SrMnO_3$, and 20% $SrMnO_{2.69}$.
		1100 °C, 4h	25% $Sr_3Mn_2O_7$, 25% $EuMnO_3$, 15% $SrMnO_{3-x}$, 15% Mn_2O_3, 10% $Sr_2Cu_2O_5$ and 10% $Sr_2Mn_2O_5$.

Table 3.3.1d Attempted synthesis of $Eu_3Ba_{2-x}Sr_xMn_2Cu_2O_{12}$ (x = 0, 1, 2)

The oxygen annealed $Eu_3Ba_2Mn_2Cu_2O_{12}$ product showed a small increase in the *c* lattice parameter in comparison with the sample prepared in air:

Target Phase	Reagents	Heat Treatment	Products
$Eu_3Ba_2Mn_2Cu_2O_{12}$	Eu_2O_3, BaO_3, Mn_2O_3 and CuO	1000 °C, 4h	30% $EuBa_2Cu_3O_{6.13}$, 20% $Eu_{1.2}Ba_{1.8}Cu_3O_7$, 20% Mn_2O_3, 15% $CuEu_2O_4$ and 15% $BaMnO_3$.
		1100 °C, 4h, under a flow of oxygen	100% target phase (but with slightly altered cell parameters)

Table 3.3.1e Attempted synthesis of $Eu_3Ba_2Mn_2Cu_2O_{12}$ under a flow of oxygen

Unfortunately, the high temperature synthesis of $Sm_3Ba_2Mn_2Cu_2O_{12}$ led to deterioration of the sample:

Target Phase	Reagents	Heat Treatment	Products
$Sm_3Ba_2Mn_2Cu_2O_{12}$	Sm_2O_3, BaO_3, Mn_2O_3 and CuO	1000 °C, 4h	35% Sm_2CuO_4, 25% $SmBa_2Cu_3$ $O_{6.11}$, 20% Mn_2O_3, 10% $BaCuO_4$ and 10% $Sm_{1.4}Ba_{1.6}Cu_3O_7$
		1100 °C, 4h	95% target phase and 5% Sm_2CuO_4
		1120 °C, 4h	30% BaO, 30% $(Sm_{0.925}Ba_{0.075})CuO_{4-x}$, 20% $SmMnO_3$, 10% $SmBa_2Cu_3O_7$ and 10% $Sm_{1.4}Ba_{1.6}Cu_3O_7$

Table 3.3.1f Attempted synthesis of $Sm_3Ba_2Mn_2Cu_2O_{12}$ at high temperature

The use of MnO_2 in place of Mn_2O_3 caused no significant change in the products produced, or their purity:

Target Phase	Reagents	Heat Treatment	Products
$Sm_3Ba_2Mn_2Cu_2O_{12}$	Sm_2O_3, BaO_3, MnO_2 and CuO	1000 °C, 4h	40% Sm_2CuO_4, 25% $SmBa_2Cu_3$ $O_{6.11}$, 20% MnO_2, 10% $BaCuO_4$ and 5% $Sm_{1.4}Ba_{1.6}Cu_3O_7$
		1100 °C, 4h	95% target phase and 5% Sm_2CuO_4

Table 3.3.1g Synthesis of $Sm_3Ba_2Mn_2Cu_2O_{12}$ using MnO_2

Pelletising the reactants after the first heating stage led to a slight improvement in the purity of the target phase:

Target Phase	Reagents	Heat Treatment	Products
$Sm_3Ba_2Mn_2Cu_2O_{12}$	Sm_2O_3, BaO_3, MnO_2 and CuO	1000 °C, 4h	35% Sm_2CuO_4, 20% $SmBa_2Cu_3O_{6.11}$, 20% MnO_2, 15% $BaCuO_4$ and 10% $Sm_{1.4}Ba_{1.6}Cu_3O_7$
		pelletised, then 1100 °C, 4h	100% target phase

Table 3.3.1h Synthesis of $Sm_3Ba_2Mn_2Cu_2O_{12}$ by pelletising

The synthesis of $^{153}Eu_3Ba_2Mn_2Cu_2O_{12}$ proved more difficult than the synthesis of the non-isotope specific phase, requiring additional heat treatments to achieve phase pure product:

Target Phase	Reagents	Heat Treatment	Products
$^{153}Eu_3Ba_2Mn_2Cu_2O_{12}$	$^{153}Eu_2O_3$, $BaCO_3$, Mn_2O_3 and CuO	1000 °C, 4h, pelletised then 1100 °C, 4h	75% target phase and 25% Eu_2CuO_4.
		pelletised then 1100 °C, 4h	85% target phase and 15% Eu_2CuO_4.
		pelletised then 1100 °C, 4h	90% target phase and 10% Eu_2CuO_4.
		pelletised then 1100 °C, 4h	95% target phase and 5% Eu_2CuO_4.
		pelletised then 1100 °C, 4h	100% target phase.
		pelletised then 1050 °C, ~18h under a flow of oxygen	100% of target phase, with increased *c* lattice parameter

Table 3.3.1i Synthesis of $^{153}Eu_3Ba_2Mn_2Cu_2O_{12}$

The synthesis of $^{154}Sm_3Ba_2Mn_2Cu_2O_{12}$ also proved more difficult than the synthesis of the non-isotope specific phase, and additional heat treatments were required to produce a phase pure sample:

Target Phase	Reagents	Heat Treatment	Products
$^{154}Sm_3Ba_2Mn_2Cu_2O_{12}$	$^{154}Sm_2O_3$, $BaCO_3$, Mn_2O_3 and CuO	1000 °C, 4h, pelletised then 1100 °C, 4h	40% target phase, 35% Sm_2CuO_4 and 25% $Sm_2BaCuMnO_7$.
		pelletised then 1100 °C, 4h	70% target phase and 30% $Sm_2BaCuMnO_7$.
		pelletised then 1100 °C, 4h	80% target phase and 20% $Sm_2BaCuMnO_7$.
		pelletised then 1100 °C, 4h	as above
		pelletised then 1100 °C, 4h	as above
		pelletised then 1100 °C, 4h	as above

Table 3.3.1j Synthesis of $^{154}Sm_3Ba_2Mn_2Cu_2O_{12}$

3.3.2 Structural Investigation

The model used as the basis for the refinements was that given by Hervieu [5]. Initially the room temperature data set from $^{153}Eu_3Ba_2Mn_2Cu_2O_{12}$ was analysed; identical methodology was subsequently employed for the data collected at the lower temperatures and for the oxygen-annealed and samarium samples. The tetragonal unit cell, 3.88 x 35.2 Å (space group I 4/m m m) could account for all the reflections in the diffraction profile of the europium based phase; for $^{154}Sm_3Ba_2Mn_2Cu_2O_{12}$ few moderate intensity reflections demanded the incorporation of $Sm_2BaCuMnO_7$ as a second phase in the refinement. For this data set an absorption co-efficient was refined but residual problems in modelling this behaviour lead to a small negative thermal displacement parameter for the absorbing atom due to strong correlations in these parameters. Scattering lengths were taken as default values within GSAS except for ^{154}Sm, 9.30 fm, and ^{153}Eu, 8.22fm.

In the initial stages of the refinement the manganese was placed solely on the (0,0,0.16) position and copper on the (0,0,0.04) site, oxygen atoms were confined to the special sites as given by Hervieu [5]. The refinement proceeded

satisfactorily with incorporation of instrument parameters, atomic positions and atomic displacement parameters. Inspection of the refined atomic displacement parameters showed a number of anomalies. The values for the manganese and copper sites became unrealistically large, 100 x U_{iso} > 8 $Å^2$; indicating that for both sites the scattering was of a lower magnitude. The displacement parameters for O(4) (near (0, 0, 0.22) and forming an apex to the MnO_6 octahedron) were significantly higher than those for the other oxygen sites within the material. The structural model was therefore modified by allowing copper and manganese to distribute over the two (0,0,z) sites. Initially the site occupancies were allowed to vary freely but the 1:1 overall Cu:Mn ratio was retained within e.s.d.s so this composition was fixed over the two sites for the remainder of the refinement. In order to maintain stability in the refinement the thermal displacement parameters of the two sites and each of the two atoms occupying them were constrained to be equal though this value was allowed to vary. Such a constraint can be crucial as partially replacing manganese (b = -3.73fm) by copper (b = 7.718fm) can lead to a small effective scattering from a site making determination of its thermal displacement parameter impossible. Refinement of anisotropic thermal displacement parameters for O(4) demonstrated the origin of the high U_{iso} for this site with large components found in the *xy* plane. This is a manifestation of disorder in the oxygen position in this plane as has been observed in other layered perovskites where there is mismatch between the various A and B cation types and their co-ordination to oxygen. Therefore this oxygen was displaced on to an (x,0,z) site with x ≈ 0.1 and z ≈ 0.22 with ¼ occupancy and both positional parameters and the isotropic thermal displacement parameter varied; the refinement converged smoothly on this basis. Inspection of the barium and lanthanide atom displacement parameters showed these values to be reasonable and attempts to disorder these ions reverted to the perfect segregation proposed by Hervieu [5] which was, therefore, maintained in the final stages of the refinement.

One further aspect of the oxygen distribution was probed in the final stages of the refinement. The (½,½,½) site, which lies between the CuO_5 square pyramids, is formally vacant in the basic structural model. However, given the partial displacement of manganese onto this site, refined here, it is possible that partial occupancy of this "inter-cuprate" layer sites occurs. Therefore oxygen was allowed to occupy the (½,½.½) site and its occupancy factor was refined leading to a small, but statistically significant determined site occupation. Refinement of both the small occupation factor and thermal displacement parameter for this site

proved problematical so they were refined in alternate cycles. The final refined stoichiometry was equivalent to $^{153}Eu_3Ba_2Mn_2Cu_2O_{12.1}$.

The overall profile fit to the back scattering data was excellent but close inspection of the 90° bank data at longer d-spacings showed a few weak additional reflections not fitted by the $^{153}Eu_3Ba_2Mn_2Cu_2O_{12.1}$ unit cell. A number of these could be assigned to the cryostat and aluminium but three further reflections could not be allocated to such instrumental origins. The d-spacings of these reflections lying to slightly larger d-spacings than the main reflections from the $^{153}Eu_3Ba_2Mn_2Cu_2O_{12.1}$ phase could be assigned to a perovskite-like impurity and a reasonable fit could be achieved using an orthorhombic $GdFeO_3$ type structure as, for example, adopted by Gd_2MnCoO_6 [12]. Such a structure type was introduced into the refinement as disordered $(Eu,Ba)(Mn,Cu)O_3$ refinement of lattice parameters and phase fraction alone produced a slight improvement to the profile fit. However given the paucity of data, three weak reflections, full refinement of this additional phase was not attempted; the refinement of the phase fraction indicated a weight fraction within the sample of <5 %.

A similar refinement process was followed for each of the other three data sets from $^{153}Eu_3Ba_2Mn_2Cu_2O_{12+y}$ and in each case convergence was reached.

For $^{154}Sm_3Ba_2Mn_2Cu_2O_{12+y}$ a similar refinement methodology was used but with the incorporation of $Sm_2BaCuMnO_7$ as a second phase in the refinement process and the use of excluded regions to remove peaks deriving from instrumental factors. A co-ordinate description for $Sm_2BaCuMnO_7$ was taken from the well known Ruddlesden–Popper phase $Sr_3Ti_2O_7$ [13] with fully disordered *A* and *B* cation sites, and only the basic instrumental and structural parameters refined in order to fit the contribution of this phase to the profile. For sites occupied by samarium, the thermal displacement factors refined to significant negative values; this is an artefact of the sample absorption, not corrected for in this sample but significant for the presence of 1 % ^{149}Sm (absorption cross section 42,0820 b).

Refined atomic co-ordinates, lattice parameters, profile fit factors and derived bond lengths and angles are summarised in Table 3.3.2. Table 3.3.3 summarises the derived bond lengths and angles of importance and bond valence calculations following the method of Brown [14] for the cation sites in $^{153}Eu_3Ba_2Mn_2Cu_2O_{12+y}$ at 298K are summarised in Table 3.3.4.

Figures 3.3a and 3.3b show typical profile fits (for the backscattering and 90° banks in turn) as obtained for $^{153}Eu_3Ba_2Mn_2Cu_2O_{12+y}$, 150 K data and $^{154}Sm_3Ba_2Mn_2Cu_2O_{12+y}$ 290 K data respectively.

Table 3.3.2 Refined atomic co-ordinates, lattice parameters and profile fit factors. Space group I4/mmm Eu/Sm(1) on (0,0,½), Eu/Sm(2) on (0,0,$z_{Eu/Sm(2)}$), Ba on (0,0,z_{Ba}), Cu(Mn) on (0,0,z_{Cu}) with Cu site occupancy residual is n_{Mn} (1- n_{Cu}), Mn(Cu) on (0,0,z_{Mn}) with Mn site occupancy $n_{Mn,}$ O(1) on (½, 0,$z_{O(1)}$), O(2) on (0,0,$z_{O(2)}$), O(3) on (½,0,$z_{O(3)}$), O(4) on ($x_{O(4)}$,0,$z_{O(4)}$) with ¼ occupancy, O(5) on (½,½,½) with site occupancy $n_{O(5)}$. Thermal displacement parameters (all x 100, Å^2) for each atom sites are also given, values for Cu and Mn were constrained to be equal.

Compound Temperature	Eu as prepared 2K	Eu as prepared 150K	Eu as prepared 298K	Eu O_2 annealed 298K	Sm as prepared 298K
U_{iso} Eu/Sm(1)	-0.06(6)	0.06 (7)	0.69(7)	0.82(5)	-0.84(9)
$z_{Eu/Sm(2)}$	0.71209(5)	0.71206(6)	0.71211(6)	0.71212(4)	0.71225(6)
U_{iso} Eu/Sm(2)	0.75(5)	0.87(6)	1.58(6)	1.70(4)	0.10(7)
z_{Ba}	0.60459(8)	0.60472(10)	0.60516(10)	0.60560(7)	0.60462(12)
U_{iso} Ba	0.78(5)	0.96(6)	1.12(7)	1.27(5)	3.38(12)
z_{Cu}	0.04790(7)	0.04790(8)	0.04799(8)	0.04798(6)	0.04837(11)
n_{Cu}	0.836(3)	0.830(4)	0.837(4)	0.818(2)	0.807(4)
U_{iso} Cu/Mn	0.21(6)	0.27(7)	0.50(8)	0.64(5)	2.56(11)
z_{Mn}	0.1649(2)	0.1646(3)	0.1645(3)	0.1649(2)	0.1654(4)
$z_{O(1)}$	0.04250(5)	0.04240(6)	0.04227(6)	0.04225(4)	0.04306(6)
U_{iso} O(1)	1.21(4)	1.38(5)	1.52(5)	1.57(5)	3.21(7)
$z_{O(2)}$	0.11305(8)	0.11309(9)	0.11302(9)	0.11312(6)	0.11337(11)
U_{iso} O(2)	1.72(7)	1.84(8)	1.99(8)	1.98(4)	3.93(11)
$z_{O(3)}$	0.17124(5)	0.17124(6)	0.17116(6)	0.17090(4)	0.16976(8)
U_{iso} O(3)	1.87(4)	1.97(5)	2.19(5)	2.30(3)	4.11(7)
$x_{O(4)}$	0.0899(11)	0.0868(13)	0.0806(17)	0.0736(15)	0.0877(14)
$z_{O(4)}$	0.22348(9)	0.22354(10)	0.22385(11)	0.22375(7)	0.22270(12)
U_{iso} O(4)	0.36(13)	0.57(16)	1.13(18)	2.18(14)	3.52(8)
$n_{O(5)}$	0.108(10)	0.091(11)	0.091(12)	0.122(7)	0.145(12)
U_{iso} O(5)	1.3(1.0)	1.4(1.2)	1.7(1.4)	2.0(8)	3.5(1.0)
a / Å	3.88081(2)	3.88176(2)	3.88500(2)	3.88136(2)	3.88362(3)
c / Å	35.1795(3)	35.2197(4)	35.2949(4)	35.3507(3)	35.4928(5)
R_p	2.44	2.48	2.71	9.53	6.57
R_{wp}	4.24	4.26	4.75	11.9	8.07
χ^2	3.01	1.86	2.48	3.43	6.75

Table 3.3.3. Derived bond lengths and angles of note.

Compound	Eu as prepared	Eu as prepared	Eu as prepared	Eu O_2 annealed	Sm as prepared
Temperature	2K	150K	298K	298K	298K
Bond					
Eu1 – O1 x 8	2.450(1)	2.449(1)	2.449(1)	2.449(1)	2.471(1)
Eu1 – O5 x 4*	2.7442(1)	2.7448(1)	2.7471(1)	2.7445(1)	2.7461(1)
Eu2 – O3 x 4	2.415(2)	2.415(2)	2.421(2)	2.427(1)	2.458(2)
Eu2 – O4a x 4*	3.027(3)	3.020(4)	3.005(5)	2.982(4)	3.020(4)
	2.541(3)	2.550(3)	2.569(4)	2.583(4)	2.544(4)
Eu2 – O4b x 1*	2.293(4)	2.293(5)	2.282(5)	2.285(3)	2.334(5)
Ba – O1 x 4	2.922(3)	2.930(3)	2.950(4)	2.964(2)	2.923(4)
Ba – O2 x 4	2.7602(4)	2.7606(5)	2.7611(5)	2.7574(1)	2.7637(6)
Ba – O3 x 4	3.044(3)	3.042(3)	3.033(4)	3.016(2)	3.019(4)
Cu(Mn) – O1 x 4	1.9497(3)	1.9505(3)	1.9530(4)	1.9512(3)	1.9509(4)
Cu(Mn) – O2 x 1	2.292(4)	2.296(4)	2.295(4)	2.303(3)	2.307(5)
Cu(Mn) – O5*	1.685(2)	1.687(3)	1.694(3)	1.696(2)	1.717(4)
Mn(Cu) – O2x 1	1.825(9)	1.815(10)	1.817(10)	1.830(7)	1.848(15)
Mn(Cu) – O3 x 4	1.9531(9)	1.9548(12)	1.9566(12)	1.9523(8)	1.9479(11)
Mn(Cu) – O4b x4* x ¼	2.089(8)	2.103(9)	2.118(9)	2.100(7)	2.060(14)
Oct tilt	9.62(12)	9.23(15)	8.5(2)	7.82(15)	9.5(2)
Cu–O1–Cu	168.8(2)	168.6(2)	168.1(1)	168.1(2)	168.9(2)
Mn–O3–Mn	166.9(5)	166.3(6)	166.2(6)	167.5(4)	171.0(9)

* Indicates partially occupied site

Table 3.3.4. Bond valence sums for $Eu_3Ba_2Mn_2Cu_2O_{12}$ at 298K (the number of each bond is given in Table 3.3.3).

Atom	Eu(1)	Eu(2) 4 x O(4)	Eu(2) 2 x (4a) 2 x (4a`)	Ba	Cu II	Cu III	Mn III	Mn IV	Oxygen valence
O(1)	0.3630	-	-	0.1657	0.4769	0.5608	-	-	2.01 Cu II
O(2)	-	-	-	0.2762	0.1892	0.2225	0.8572	0.8412	2.15 Cu II
O(3)	-	0.3915	0.3915	0.1324	-	-	0.5878	0.5768	2.22 Mn III
O(4a)	-	0.1512*	0.2624# 0.0808#	-	-	-	-	-	1.58* Mn III 1.64# Mn III
O(4b)	-	0.5968*	0.5700#	-	-	-	0.3800	0.3729	
O(5)	0.1622	-	-	-	n/a	n/a	-	-	-
Cation valence	2.97	2.78	2.82	2.30	2.10	2.47	3.59	3.52	-

The values marked as * and # differentiate the two europium-oxygen bonding models based on O(4) on special site (*) and displaced on to (x,0,z) (#) leading to different bond valence sums.

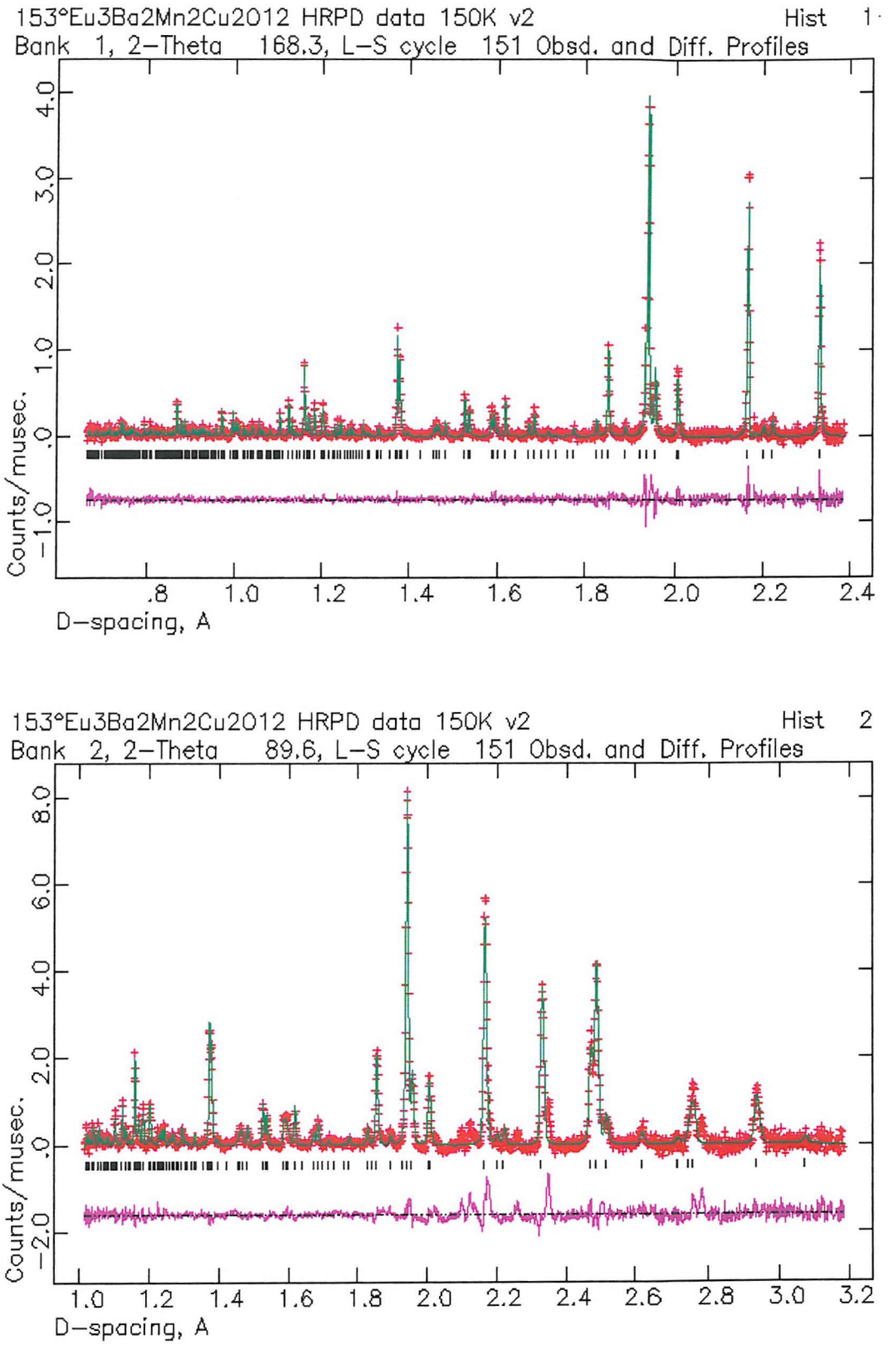

Figure 3.3a Profile fit as obtained to $^{153}Eu_3Ba_2Mn_2Cu_2O_{12+y}$ 150 K data sets

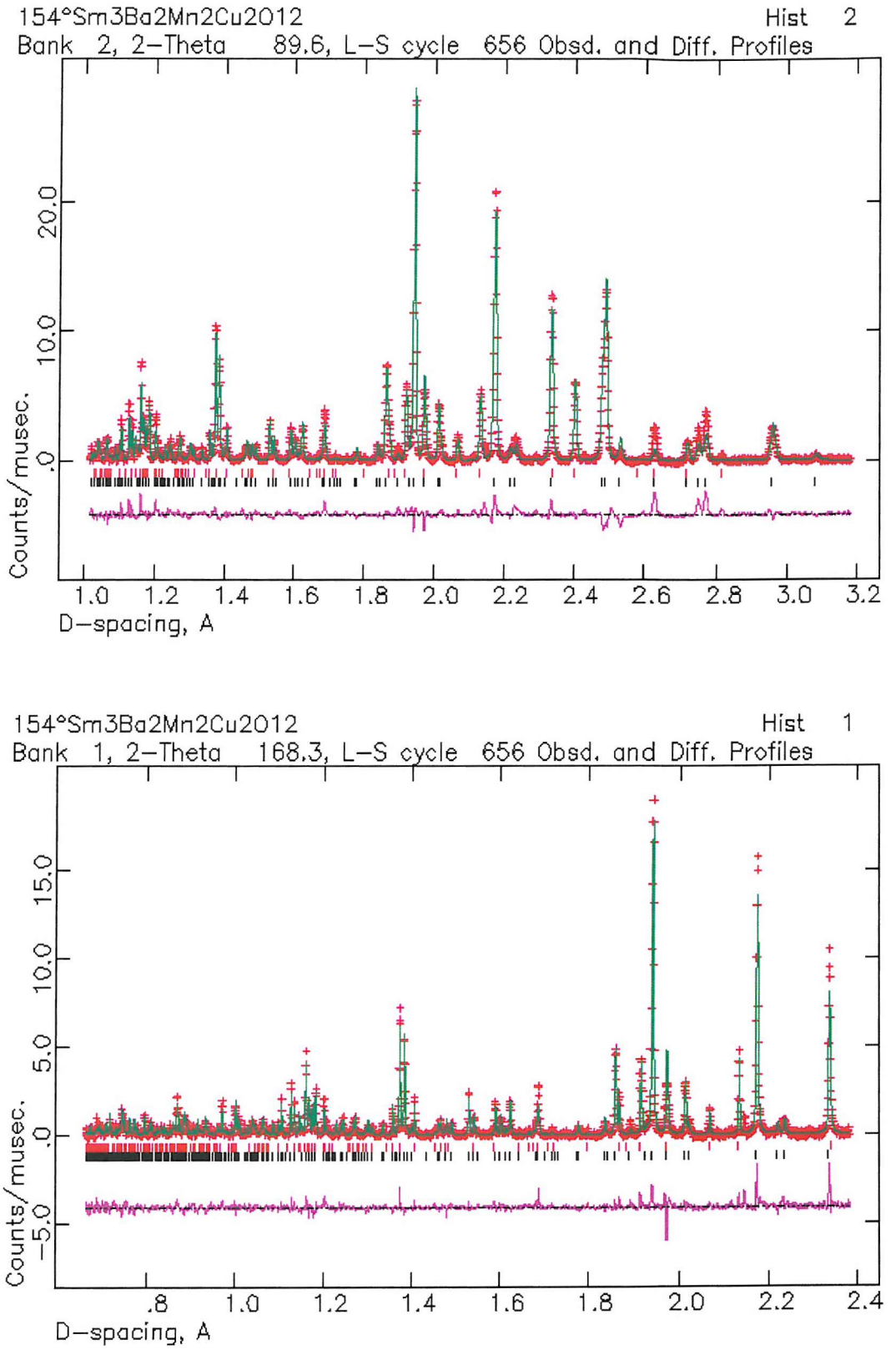

Figure 3.3b Profile fit as obtained to $^{154}Sm_3Ba_2Mn_2Cu_2O_{12+y}$ 298 K data sets

3.4 Discussion

The idealised $Ln_3Ba_2Mn_2Cu_2O_{12}$ structure, shown in Figure 3.1a, consists of a Ln_2MnO_4 structure block separated by $LnBa_2Cu_2MnO_8$ blocks. Alternatively the structure can be considered as an oxygen deficient quadruple perovskite block with the layer sequence MnO_6-CuO_5-CuO_5-MnO_6 separated by 'rocksalt' layers based on EuO; full oxygen occupancy of the perovskite layers would give a stoichiometry of the type $A_5B_4O_{13}$, which is the n = 4 member of the Ruddlesden-Popper series $A_{n+1}B_nO_{3n+1}$.

However, as with many mixed A and B cation perovskite superstructures the true structure is more complex as each of the cation types has specific structural and coordinative requirements that cannot all necessarily be satisfied. In addition there exists, for systems containing more than one A or B cation type, the potential for ordered, partially ordered or fully disordered distribution.

In $Eu_3Ba_2Mn_2Cu_2O_{12.1}$ there is a significant mixing between the formally copper and manganese sites. In each sample studied this mixing was refined independently at 0.83(±0.05)/0.17 confirming unequivocally that in this structure full segregation of the B cation types does not occur. The presence of a small level of impurity (approx. 3 %) of the type (Eu,Ba)(Mn,Cu)O_3 in the product has little influence on the stoichiometry of the main phase; the presence of this material, also with a perovskite based structure and similar unit cell parameters, only becomes apparent under very high resolution neutron diffraction. Presumably this phase represents a greater degree of manganese and copper disordering than is seen in $Eu_3Ba_2Mn_2Cu_2O_{12.1}$ and its observation may be related to the presence of intergrowths phases as observed by Hervieu [5].

For double perovskites of the type AA'BB'O_n Poeppelmeier and Anderson [15] have defined rules controlling whether two B cations will separate into ordered structures, either layered or three dimensional. These rules include the requirement for large charge differences on B and B' (the charge on B' to be two higher than that on B), ionic size differences (B' larger than B) and additional structure directing parameters, such as the Jahn-Teller effect, to promote layering of the two ions. Consideration of Mn^{3+}/Mn^{4+} and Cu^{2+} as present in $Eu_3Ba_2Mn_2Cu_2O_{12.1}$ indicates that there is a driving force for segregation of these ion types but it is equivocal. The formal charge difference is close to two at 1.5+, the ionic radii are similar at r (Mn^{3+}) = 0.58 Å, r (Mn^{4+}) = 0.53 Å and r (Cu^{2+}) = 0.60 Å (as modified and used in reference [15]), and both Mn^{3+} and Cu^{2+} are

subject to Jahn-Teller distortions. This data may be compared with that of tin (IV), r (Sn^{4+}) = 0.69 Å, which layers with Cu^{2+} in La_2SnCuO_6 [15]. So while Mn^{4+} and Cu^{2+} would be expected to have tendencies towards ordering the same would not be expected of Mn^{3+} and Cu^{2+}. Hence the observed incomplete separation of manganese and copper in $Eu_3Ba_2Mn_2Cu_2O_{12.1}$ is consistent with these arguments such that manganese has a tendency, presumably as Mn^{3+}, to disorder onto the copper site. Bond valence calculations for manganese and copper support the refined co-ordination geometries, Table 3.3, with calculations based on Cu^{2+} producing a bond valence sum of 2.1 and both Mn^{3+} and Mn^{4+} values giving manganese bond valence sums close to 3.5.

In $Eu_3Ba_2Mn_2Cu_2O_{12.1}$ the Eu^{3+} and Ba^{2+} cations are fully ordered, presumably due to their significant differences in ion size (r (Eu^{3+}) = 1.07 Å and r (Ba^{2+}) = 1.42 Å, in 8-fold co-ordination) and co-ordination preferences. Europium adopts the lower 8 and 9 co-ordination sites to oxygen while barium is 12 co-ordinated (r (Ba^{2+}) = 1.61 Å in 12-fold co-ordination).

A further consequence of layering B type cations in perovskite type structures is mismatch in the sheet dimensions leading to buckling of layers and rotation of polyhedra as seen in $Ln_2Ba_2Ti_2Cu_2O_{12}$ [16]. Local and long range displacements of the oxygen atoms may also help better serve the coordination preferences of A type cations. In $Eu_3Ba_2Mn_2Cu_2O_{12.1}$ these oxygen displacements are associated with O(4), the terminal oxygen of the MnO_6 octahedra in the Eu_2O_2 layers (see Fig. 3.4a), and are probably a result of the co-ordination preferences of Eu and the otherwise weak interaction of this oxygen with the cations. Without displacements the Eu-O distances would be 4 x 2.421 + 4 x 2.773 + 1 x 2.265 Å, but as a result of local displacements the latter four become, on average, 2 x 2.569 + 2 x 3.005 Å. In terms of bond valence calculations this has the effect of increasing the Eu bond valence to 2.82 from 2.77, see Table 3.3.4. For the oxygen itself bond valence calculations give values well below two which are increased slightly through the local displacement towards europium.

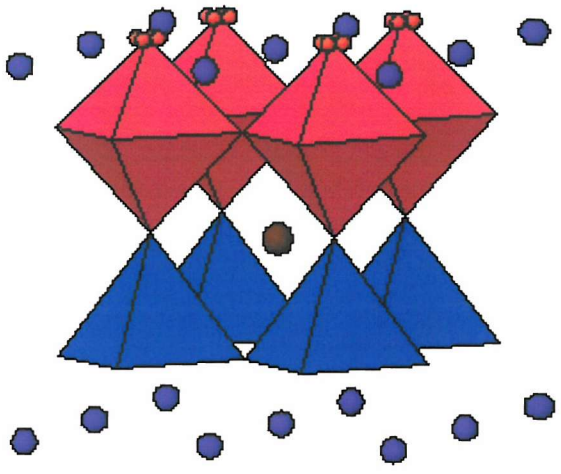

Figure 3.4a Section of the $Eu_3Ba_2Mn_2Cu_2O_{12}$ structure showing how the local oxygen displacements are associated with the terminal oxygen of the MnO_6 octahedra.

The final feature of interest in the $Eu_3Ba_2Mn_2Cu_2O_{12.1}$ structure is the partial occupancy of the (½,½,½) site by oxygen. The small but significant refined value of 0.10(1) was refined independently for each data set. It is likely that occupation of this site is associated with the partial occupation of the neighbouring (0, 0, 0.05) site by manganese. Intriguingly the refined occupancy for this site, which bridges two square based CuO_5 pyramids, is almost exactly half the level of manganese substitution on this square pyramidal site. This would seem to suggest that the manganese locally orders within the structure replacing $O_5Cu..\ ..CuO_5$, where represents the vacant (½,½,½) position by $O_5Mn..O..MnO_5$ in 10 % of the site pairs, (see Fig. 3.4b).

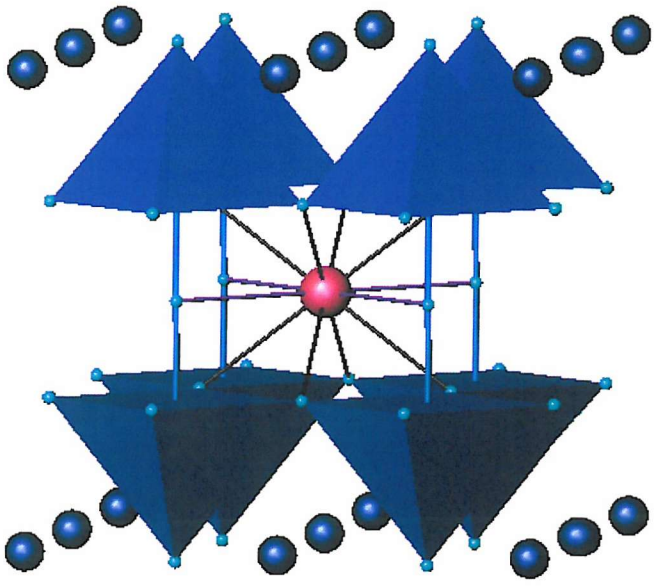

Figure 3.4b Section of the $Eu_3Ba_2Mn_2Cu_2O_{12}$ structure showing the partially occupied O(5) (½,½,½) site bridging two square based CuO_5 pyramids, whilst also being coordinated to the europium ion.

For the samarium derivative the main differences are those that would be expected from replacing europium ions (r (Eu^{3+}) = 1.07 Å) with larger samarium ions (r (Sm^{3+}) = 1.08 Å). The presence of a higher level of impurity within this product means that caution should be applied in interpreting the results in terms of the cation composition, although the values of extracted distances and angles have equal validity. Both the *a* and *c* lattice parameters increase, as do the average bond lengths around the lanthanide site resulting in a reduced buckling of the MnO_2 layers (Mn-O-Mn increasing from 167° to 171°); the local environments of the barium and Mn/Cu are largely unaffected. More important are the differences in some of the associated structural features. Firstly, there is a small increase in the distortion around the lanthanide site and, secondly, the oxygen level on the partially occupied site adjacent to the lanthanide is significantly higher for samarium. This latter factor would seem to principally result from the change in size of the lanthanide ion, rather than a significant increase in the level of manganese on the copper site, which is only marginally higher at 0.19 (cf 0.17 for Eu). Clearly placing the samarium between the cuprate layers increases their separation, as a result of the increased Ln-O(1) distance, Cu….Cu is 3.388Å at 298K for Ln = Eu in $Ln_3Ba_2Mn_2Cu_2O_{12}$ but 3.434Å for Ln = Sm and thus oxygen can more easily occupy this inter-cuprate site.

The limits in terms of lanthanide size that exist for the $Ln_3Ba_2Mn_2Cu_2O_{12}$ series can be rationalised in terms of the structure presented here. Lanthanides larger than Sm experience difficulties in forming this phase, the origin of this behaviour being the Ln(1) site, which is formally co-ordinated to 8 oxygen atoms in the idealised structure. Larger lanthanides would prefer to increase their co-ordination within oxides to more than 8 with longer Ln-O distances. This means that incorporation of oxygen on to the (½,½,½) site, with concomitant displacement of manganese (presumably as Mn^{4+}) on to the neighbouring position, becomes more facile. Therefore increasing lanthanide size causes the structure to move towards a more disordered arrangement in terms of B cation and oxide ion distributions. The end result is the formation of disordered structures like the impurity phase $Sm_2BaMnCuO_7$, where manganese and copper share a site, rather than the desired product. In the case of smaller lanthanides, incorporation into the 'rocksalt' layers presumably becomes unfavourable as is illustrated by the existence of the K_2NiF_4 structure for Ln_2CuO_4 only occurring for Ln = La [17], and in a distorted form for Ln_2CuO_4 Ln = Nd – Gd[18].

The effect of oxygen annealing $Ln_3Ba_2Mn_2Cu_2O_{12}$ is small in term of changes to the structure. A small increase in the manganese occupancy of the copper site occurs (0.182(2) v 0.165(4)) with an associated increase in the occupancy of the partially filled oxygen site O(5) (0.12(1) from 0.10 (1)). These slight changes in cation and oxygen distribution result in small changes in the geometry of the $Cu(Mn)O_5$ square based pyramid with a lengthening of the apical bond and shortening of the in-plane bonds. This is reflected in the observed decrease in *a* parameter and increase in *c* parameter.

3.5 Conclusions

The $Ln_3Ba_2Mn_2Cu_2O_{12}$ structure is one of the rare complex oxide types that has two B type cations within perovskite structure elements formally ordered to form layers. This characteristic is a requirement for forming cuprates that might demonstrate superconductivity, and has been noted in quadruple perovskites containing Sn and Cu [19], Ti and Cu [2] , Ru and Cu [16], and In and Cu in $Ba_2InCuO_{5+\delta}$ [20]. More normally the B cations are fully disordered or form ordered three dimensional arrays. However for the $Ln_3Ba_2Mn_2Cu_2O_{12}$ compounds the B cation ordering has been shown to be imperfect and the displacement of

approximately 15 – 20 % of Mn ions into the CuO_2 sheets is likely to destroy any chance of superconductivity. Additionally, the partial cross-linking of $Cu(Mn)O_5$ square-pyramids, through the addition of excess oxygen, will also have an inhibiting effect. The chances of forming fully segregated copper and manganese sites and eliminating the additional oxygen is highest for smaller lanthanides which will contract the inter CuO_5 square pyramid distance and inhibit manganese occupation of these sites. However, the smaller lanthanide sizes are not compatible with the 9-fold co-ordination required of this ion within the 'rocksalt' layers.

Clearly it should be possible to stabilise the structure by the introduction of two different cation types and sizes to fit the two types of site occupied by europium in $Eu_3Ba_2Mn_2Cu_2O_{12.1}$. Similar studies have been undertaken on the quadruple and quintuple titanocuprate perovksites with the formation of materials such as $NdDyBa_2Cu_2Ti_2O_{11}$ and $NdDyCaBa_{1.5}Sr_{0.5}Cu_{2.2}Ti_{2.8}O_{14}$ [21]. However, our attempts to synthesise materials such as $DyNd_2Ba_2Cu_2Mn_2O_{12}$ have been unsuccessful resulting in the preferred formation of competing phases such as $Ln_2BaMnCuO_7$ and Ln_2CuO_4. Possibly high-pressure or sealed-tube techniques could be used to stabilise the high manganese oxidation state to enable the formation of the desired phases, or alternatively sol-gel techniques might succeed through closer integration of the reactants.

The partial displacement of manganese on to the copper sites permits the formation of some linked MnO_n polyhedra in the *c* direction as well as the *ab* plane and given the overall manganese oxidation state near 3.5 these materials could be expected to demonstrate magnetoresistive effects. However, the partial occupancy of the manganese site by copper destroys such a possibility.

Finally, it is worth noting that the potential for ordering on the mixed Cu/Mn sites, as suggested by the partial occupancy of the (½,½,½) site by oxygen being almost exactly half the level of manganese substitution on the associated square pyramidal site, could well prove interesting. Further exploration, and structural determination, of this factor could be achieved using a technique sensitive to localised structure, e.g. EXAFS.

3.6 References

1 Cava R J, *J. Am. Ceram. Soc.*, 2000, **83**, 5; Karpinski J, Meijer G I, Schwer H, Molinski R, Kopnin E, Conder K, Angst M, Jun J, Kazakov S, Wisniewski A, Puzniak R, Hofer J, Alyoshin J, Sin J, *Supercond. Sci. Technol.*, 1999, **12**, R153

2 Gormezano A, Weller M T, *J. Mat Chem.*, 1993, **7**, 3, 771

3 Elemans J B A A, van Laar B, van der Veen K R, Loopstra B O, *J. Solid State Chem.*, 1971, **3**, 238

4 Battle P D, Green M A, Laskey N S, Millburn J E, Rosseinsky M J, Sullivan S P, Vente J F, *Chem. Commun.*, 1996, **6**, 767

5 Hervieu M, Michel C, Genouel R, Maignan A, Raveau B; *J. Solid State Chem.*, 1995, **115**, 1

6 Matsubara I, Kida N, Funahashi R, Ueno K, *Chem Lett.*, 1996, 971

7 Matsubara I, Kida N, Funahashi R, Ueno K, Ishikawa H, *Physica C* 1997, **282-287**, 945

8 Matsubara I, Kida N, Funahashi R, Ueno K, Ishikawa H, Ohno N, *J. Solid State Chem.*,1998, **141**, 546

9 Sarathy KV, Sreeraj P, *Solid State Commun.*, 2002, **122**, 385; Martin C, Maignan A, Hervieu M, Raveau B, Hejtmanek J, *Eur. Phys. J. B*, 2000, **16**, 469

10 Licci F, Gauzzi A, Marezio M, Radaelli G P, Masini R, Chaillout-Bougerol C, *Phys. Rev. B*, 1998, **58**, 15208; Floros N, Hervieu M, van Tendeloo G, Michel C, Maignan A, Raveau B, *Solid State Sci.*, 2000, **2**, 1

11 Larson A C, von Dreele R B, Generalised Structure Analysis System, Los Alamos National Laboratory, 1994

12 Marsh A, Clark C C, *Philos. Mag.*, 1969, **19**, 449

13 Elcombe M M, Kisi E H, Hawkins K D, White T J, Goodman P, Matheson S, *Acta Crystollagr. B*, 1991, **47**, 305

14 Altermatt D, Brown I D, *Acta Crystollagr. B*, 1985, **41**, 240

15 Anderson M T, Greenwood K B, Taylor G A, Poeppelmeier K R, *Prog. Solid State Chem.*, 1993, **22**, 197

16 Weller M T, Pack M J, Binsted N, *Angew. Chem. Int. Ed.*, 1998, **37**, 1094

17 Zolliker P, Cox D E, Parise J B, Carron III E M, Farneth W E. *Phys. Rev. B*, 1990, **42**, 6332

18 Uzumaki T, Kamehara N, Niwa K, *Jpn. J. Appl. Phys.*, 1991, **30** (Part 2), L981

19 Anderson M T, Poeppelmeier K R, *Chem. Mater.*, 1991, **3**, 476; Anderson M T, Poeppelmeier K R, Zhang J-P, Ian H-J, Marks L D, *Chem. Mater.*, 1992, **4**, 1305; Salvador P A, Shen L, Mason T O, Greenwood K B, Poeppelmeier K R, *J. Solid State Chem.*, 1995, **119**, 80

20 Gregory D H, Weller M T, *J. Solid State Chem.*, 1993, **107** 134

21 Mansourian-Hadavi N, Ko D, Mason T O, Poeppelmeier K R, *J. Solid State Chem.*, 2000, **155,** 216; Greenwood K B, Sarjeant G M, Poeppelmeier K R, Salvador P A,

Mason T O, Dabrowski B, Rogacki K, Chen Z, *Chem. Mater.*, 1995, **7**, 1355; Otzschi K D, Poeppelmeier K R, Salvador P A, Mason T O, Zhang H, Marks L D, *J. Am. Chem. Soc.*, 1996, **118**, 8951; Kane M H, Mason T O, Sinkler W, Marks L D, Otzschi K D, Ko D, Poeppelmeier K R, *J. Solid State Chem.*, 1999, **148**, 3

Chapter Four

Synthesis and Structural Analysis of the Solid Solutions $Sr_2Cu_{1-y}Co_yO_2X_2$ (X = Cl and Br, y = 0.2, 0.4, 0.5, 0.6, 0.8)

4.1 Introduction

Solid solutions can be synthesised for a range of materials and are essentially crystalline phases that adopt a single structure but with a variable composition. The properties of such materials, e.g. conductivity and ferromagnetism, can often be adjusted or tuned, by changing the material's composition, to produce an effective material with specific properties. For example, the metal-insulator transition of $Sm_xNd_{1-x}NiO_3$ [1] can be readily tuned between 200 and 410 K as a function of x, making these materials suitable to use in temperature dependant switches.

Solid solutions of cobalt and copper have been used in the past as a tool to explore the nature and mechanism of superconductivity by the substitution of cobalt into $YBa_2Cu_3O_{7-\delta}$ [2, 3]. Whilst other studies have concentrated on the changes in magnetic properties associated with substituting one metal for another. This has included work on traditional solid state oxides (e.g. $LaCo_{1-x}Cu_xO_3$ [4], $La_2Co_{1-x}Cu_xO_{4+x}$ [5]), phosphates (e.g. $Co_{3-x}Cu_x(PO_4)_2$ [6]) and more complex framework materials (e.g. metal hexacyano-metalates [7]). The majority of work carried out on cobalt substitution in the past has involved trivalent cobalt ions.

The cuprates $A^{2+}{}_2CuO_2X_2$ (A = Ca or Sr, X= Cl and Br) contain fully segregated oxide and halide anions [8] with halides adopting the apical positions within the metal octahedra of a K_2NiF_4 structure. As with all materials containing Cu^{2+} in an octahedral environment these octahedra become distorted, due to the Jahn–Teller effect, to produce a tetragonal environment with two lengthened Cu-X bonds and a CuO_4 square plane (see Fig. 4.1a). Thus, it would be logical that an analysis of the apical M-X bond distances in a solid solution with copper would serve as a good handle by which the strength of the Jahn–Teller distortion could be judged.

As both the phases $Sr_2CuO_2Cl_2$ [9, 10] and $Sr_2CoO_2Cl_2$ [11] are now known, an isovalent solid solution of the two could act as a useful probe of the structural differences between the two end-member phases. This should enable an exploration of the significance of the Jahn–Teller effect on the structure, although it is important to note that this requires the assumption that Co^{2+} ions are in a high spin state (as d^7 low spin ions exhibit the Jahn-Teller effect) as was shown

in a recent study [12]. Any differences caused by a change in halide ion could also be investigated by comparing the chloride and bromide analogues.

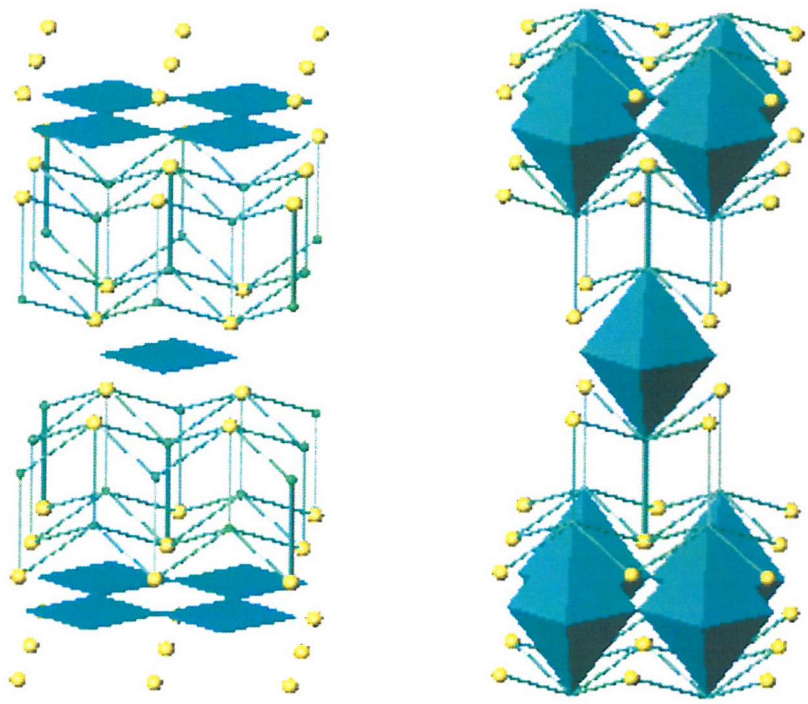

Figure 4.1a Representations of the Structure of $Sr_2CuO_2Cl_2$ with square CuO_4 planes and the Structure of $Sr_2CoO_2Cl_2$ with CoO_4Cl_2 octahedra

4.2 Experimental Procedure

Samples of $Sr_2Cu_{1-y}Co_yO_2Cl_2$ (y = 0.2, 0.4, 0.5, 0.6, 0.8) were prepared by intimately grinding together high purity stoichiometric mixtures of SrO (from $SrCO_3$ heated at 1050 °C for 4 days), $SrCl_2$, CuO and CoO (all 99.9% or better), then placing them in silica ampoules, which were sealed under vacuum. The evacuated ampoules were heated at 850 °C for 48 hours with a single interruption to regrind the intermediate products (for results, see Table 4.3.1a). All sample preparations were carried out inside a glove box (<1 ppm O_2/H_2O) due to the reactive nature of some of the starting materials. Phase purity for each phase was checked by PXD using a Siemens D5000 diffractometer operating

with Cu $K_{\alpha 1}$ radiation; the patterns were consistent with phase pure product material.

Samples of $Sr_2Cu_{1-y}Co_yO_2Br_2$ (y = 0.2, 0.4, 0.5, 0.6, 0.8) were prepared using the same method as for the oxide chlorides, that is by intimately grinding together high purity stoichiometric mixtures of SrO (from $SrCO_3$ heated at 1050 °C for 4 days), $SrBr_2$, CuO and CoO (all 99.9% or better). These reaction mixtures were placed in silica ampoules and sealed under vacuum.

Phase pure samples of the bromide analogue proved slightly more difficult to prepare and several attempts were carried out using different synthesis temperatures (using the $Sr_2Cu_{0.8}Co_{0.2}O_2Br_2$ and $Sr_2Cu_{0.2}Co_{0.8}O_2Br_2$ phases to test the reaction conditions). It was initially thought that a low temperature, 650 °C, would prevent bromide volatilisation and thus aid phase formation. However this temperature proved too low to allow complete reaction to occur and significant quantities of CoO were left alongside the target phases (for results, see Table 4.3.1b). The higher temperature of 750 °C did lead to samples with a lesser amount of CoO present (for results, see Table 4.3.1c), whilst after being treated at 850 °C samples had started to degrade to lesser oxides, probably from loss of bromide, as mentioned above (for results, see Table 4.3.1d). This led to the compromise temperature of 800 °C being tried, which proved to yield essentially phase pure samples (for results, see Table 4.3.1e). Thus, the $Sr_2Cu_{1-y}Co_yO_2Br_2$ (y = 0.5, 0.6, 0.8) reaction mixtures were heated in the evacuated ampoules at 800 °C for 48 hours with a single interruption to regrind the intermediate products.

Once more, all sample preparations were carried out inside a glove box (<1 ppm O_2/H_2O) and phase purity for each phase was checked by PXD using a Siemens D5000 diffractometer operating with Cu $K_{\alpha 1}$ radiation, over the data range of 10 – 110° 2θ. The patterns were consistent with phase pure product material with the exception of a small trace of CoO in $Sr_2Cu_{1-y}Co_yO_2Br_2$ (y = 0.5, 0.6, 0.8), estimated to be at a level of < 2 % from the ratio of the most intense $Sr_2Cu_{1-y}Co_yO_2Br_2$ and impurity reflections ($I:I_0$).

4.3 Results, including Structural Refinement

4.3.1 Synthetic Results

The sealed tube syntheses produced pure samples of the $Sr_2Co_{1-x}Cu_xO_2Cl_2$ (x = 0.2, 0.4, 0.5, 0.6, 0.8) phases:

Target Phase	Reagents	Heat Treatment	Products
$Sr_2Co_{0.2}Cu_{0.8}O_2Cl_2$	$SrCl_2$, SrO, CoO and CuO	~18h at 850 °C	95% target phase and 5% CoO
		~18h at 850 °C	100% target phase
$Sr_2Co_{0.4}Cu_{0.6}O_2Cl_2$		~18h at 850 °C	90% target phase and 5% CoO
		~18h at 850 °C	100% target phase
$Sr_2Co_{0.5}Cu_{0.5}O_2Cl_2$		~18h at 850 °C	95% target phase and 5% CoO
		~18h at 850 °C	100% target phase
$Sr_2Co_{0.6}Cu_{0.4}O_2Cl_2$		~18h at 850 °C	95% target phase and 5% CoO
		~18h at 850 °C	100% target phase
$Sr_2Co_{0.8}Cu_{0.2}O_2Cl_2$		~18h at 850 °C	95% target phase and 10% CoO
		~18h at 850 °C	100% target phase

Table 4.3.1a Synthetic conditions and results in sealed tube synthesis of $Sr_2Co_{1-x}Cu_xO_2Cl_2$ (x = 0.2, 0.4, 0.5, 0.6, 0.8)

Unfortunately, the lower temperature synthesis did not form pure samples of the bromide analogue with significant by-products being formed:

Target Phase	Reagents	Heat Treatment	Products
$Sr_2Co_{0.2}Cu_{0.8}O_2Br_2$	$SrBr_2$, SrO, CoO and CuO	~18h at 650 °C	95% target phase and 5% CoO
		~18h at 650 °C	>95% target phase and <5% $Sr(H_2O)_6Br_2$
$Sr_2Co_{0.8}Cu_{0.2}O_2Br_2$		~18h at 650 °C	90% target phase and 10% CoO
		~18h at 650 °C	55% target phase, 20% $SrBr(OH).4H_2O$, 15% $Sr(H_2O)_6Br_2$ and 10% CoO

Table 4.3.1b Synthetic conditions and results in first sealed tube synthesis of $Sr_2Co_{1-x}Cu_xO_2Br_2$ (x = 0.2, 0.8)

The slightly higher temperature synthesis produced samples with less impurities present, but these still were not phase pure:

Target Phase	Reagents	Heat Treatment	Products
$Sr_2Co_{0.2}Cu_{0.8}O_2Br_2$	$SrBr_2$, SrO, CoO and CuO	~18h at 750 °C	95% target phase and 5% CoO
		~18h at 750 °C	>95% target phase and <5% $Sr(H_2O)_6Br_2$
$Sr_2Co_{0.8}Cu_{0.2}O_2Br_2$		~18h at 750 °C	90% target phase and 10% CoO
		~18h at 750 °C	85% target phase, 10% $Sr(H_2O)_6Br_2$ and 5% CoO

Table 4.3.1c Synthetic conditions and results in second sealed tube synthesis of $Sr_2Co_{1-x}Cu_xO_2Br_2$ (x = 0.2, 0.8)

The synthetic temperature was raised still further, but unfortunately this led to a degradation of the final product, and loss of target phase:

Target Phase	Reagents	Heat Treatment	Products
$Sr_2Co_{0.2}Cu_{0.8}O_2Br_2$	$SrBr_2$, SrO, CoO and CuO	~18h at 850 °C	90% target phase, 5% $Sr(H_2O)_6Br_2$ and 5% CoO
		~18h at 850 °C	85% target phase, 10% $SrCuO_2$ and <5% $Sr(H_2O)_6Br_2$, <5% CoO
$Sr_2Co_{0.8}Cu_{0.2}O_2Br_2$		~18h at 850 °C	85% target phase, 10% $Sr(H_2O)_6Br_2$ and 5% CoO
		~18h at 850 °C	80% target phase, 10% $SrCuO_2$ and <10% $Sr(H_2O)_6Br_2$, <10% CoO

Table 4.3.1d Synthetic conditions and results in third sealed tube synthesis of $Sr_2Co_{1-x}Cu_xO_2Br_2$ (x = 0.2, 0.8)

An intermediate temperature led to the production of phase pure samples:

Target Phase	Reagents	Heat Treatment	Products
$Sr_2Co_{0.2}Cu_{0.8}O_2Br_2$	$SrBr_2$, SrO, CoO and CuO	~18h at 850 °C	95% target phase and 5% CoO
		~18h at 850 °C	100% target phase
$Sr_2Co_{0.4}Cu_{0.6}O_2Br_2$		~18h at 850 °C	90% target phase and 5% CoO
		~18h at 850 °C	100% target phase
$Sr_2Co_{0.5}Cu_{0.5}O_2Br_2$		~18h at 850 °C	95% target phase and 5% CoO
		~18h at 850 °C	100% target phase
$Sr_2Co_{0.6}Cu_{0.4}O_2Br_2$		~18h at 850 °C	95% target phase and 5% CoO
		~18h at 850 °C	100% target phase
$Sr_2Co_{0.8}Cu_{0.2}O_2Br_2$		~18h at 850 °C	95% target phase and 10% CoO
		~18h at 850 °C	100% target phase

Table 4.3.1e Synthetic conditions and results in sealed tube synthesis of $Sr_2Co_{1-x}Cu_xO_2Br_2$ (x = 0.2, 0.4, 0.5, 0.6, 0.8)

4.3.2 Structural Investigation

The model used as the basis for the refinements was that given by Miller [10] for $Sr_2CuO_2Cl_2$. Initially the $Sr_2Cu_{0.5}Co_{0.5}O_2Cl_2$ data set was analysed; an identical methodology was subsequently employed for the data collected for the phases of other stoichiometries and the bromide analogues. A tetragonal unit cell, approx. 4.01 (± 0.03) x 15.35 (± 0.17) Å in the case of the oxide chlorides and 4.04 (± 0.04) x 16.79 (± 0.22) Å in the case of the oxide bromides, space group I 4/m m m was used. This model could account for all the reflections in the diffraction profile of the oxide chlorides, whilst for the oxide bromides a few low intensity reflections were identified as CoO. However, as these additional reflections were of such low intensity, it was not necessary to incorporate a second phase into the refinement.

The refinement proceeded satisfactorily with incorporation of parameters in the order of instrument parameters, atomic positions and atomic displacement parameters. Preferred orientation parameters were included last in the refinement, to take account of the longitudinal stacking that often occurs when unit cells possess one lattice parameter significantly longer than the others. However, the preferred orientation of the $Sr_2Cu_{1-y}Co_yO_2Cl_2$ phases proved particularly strong generating an artificially intense reflection at approx. 11.5° two theta. As a result of this, and because low angle peaks are generally poorly resolved due to the spread of the X-ray beam at such angles, the structural refinement for the oxide chlorides became skewed or biased. Thus the structural refinements for these phases only used the data in the range 20 – 100° 2□. These refinement strategies, although slightly different, enabled both the oxy-chloride and oxy-bromide refinements to converge satisfactorily.

The site occupancies of the cobalt/copper site could not be allowed to vary due to the similarity in electron density between the cobalt and copper ions making them almost indistinguishable with PXD data.

Refined atomic co-ordinates, lattice parameters, and profile fit factors for $Sr_2Cu_{1-y}Co_yO_2Cl_2$ and $Sr_2Cu_{1-y}Co_yO_2Br_2$ are summarised in Tables 4.1 and 4.2 respectively. Tables 4.3 and 4.4 summarise the derived bond lengths of importance for $Sr_2Cu_{1-y}Co_yO_2Cl_2$ and $Sr_2Cu_{1-y}Co_yO_2Br_2$.

The final agreement achieved to the $Sr_2Cu_{0.5}Co_{0.5}O_2Cl_2$ and $Sr_2Cu_{0.5}Co_{0.5}O_2Br_2$ data is shown in Figures 4.3.2a and 4.3.2b.

Table 4.1 Refined atomic co-ordinates, lattice parameters and profile fit factors for $Sr_2Cu_{1-y}Co_yO_2Cl_2$. Space group I4/mmm Sr on $(0,0,z_{Sr})$, Cu/Co on (0,0,0), O on $(0,½,0)$ and Cl on $(0,0,z_{Cl})$. Thermal displacement parameters (all x 100, $Å^2$) for each atom sites are also given, values for Cu and Co were constrained to be equal, esd's are given in parentheses.

Compound	$Sr_2Cu_{0.8}Co_{0.2}O_2Cl_2$	$Sr_2Cu_{0.6}Co_{0.4}O_2Cl_2$	$Sr_2Cu_{0.5}Co_{0.5}O_2Cl_2$	$Sr_2Cu_{0.4}Co_{0.6}O_2Cl_2$	$Sr_2Cu_{0.2}Co_{0.8}O_2Cl_2$
z_{Sr}	0.39258(26)	0.39271(30)	0.39275(30)	0.39201(33)	0.3930(4)
U_{iso} Sr	2.06(11)	1.56(12)	1.74(14)	2.23(17)	2.22(18)
U_{iso} Cu/Co	1.98(21)	1.62(24)	1.97(26)	2.04(32)	2.1(4)
U_{iso} O	2.0(6)	1.7(6)	3.0(7)	1.2(7)	0.3(7)
z_{Cl}	0.1831(5)	0.1823(6)	0.1809(6)	0.1806(7)	0.1807(7)
U_{iso} Cl	2.44(25)	2.32(31)	3.09(34)	2.6(4)	3.1(5)
a / Å	3.98499(11)	4.00148(12)	4.01503(17)	4.02194(19)	4.03819(19)
c / Å	15.5034(5)	15.4194(5)	15.3534(8)	15.3239(8)	15.2203(8)
R_p	1.968	0.933	1.872	1.876	0.772
R_{wp}	2.776	1.185	2.418	2.456	0.983
χ^2	1.329	1.120	1.267	1.440	1.048

Table 4.2 Refined atomic co-ordinates, lattice parameters and profile fit factors for $Sr_2Cu_{1-y}Co_yO_2Br_2$. Space group I4/mmm Sr on $(0,0,z_{Sr})$, Cu/Co on (0,0,0), O on (0,½,0) and Br on $(0,0,z_{Br})$. Thermal displacement parameters (all x 100, $Å^2$) for each atom sites are also given, values for Cu and Co were constrained to be equal, esd's are given in parentheses.

Compound	$Sr_2Cu_{0.8}Co_{0.2}O_2Br_2$	$Sr_2Cu_{0.6}Co_{0.4}O_2Br_2$	$Sr_2Cu_{0.5}Co_{0.5}O_2Br_2$	$Sr_2Cu_{0.4}Co_{0.6}O_2Br_2$	$Sr_2Cu_{0.2}Co_{0.8}O_2Br_2$
z_{Sr}	0.40024(25)	0.40031(26)	0.40039(19)	0.40061(22)	0.39972(30)
U_{iso} Sr	1.75(15)	1.05(15)	2.48(14)	1.81(12)	2.01(17)
U_{iso} Cu/Co	0.23(29)	0.76(32)	0.74(25)	0.54(24)	0.7(4)
U_{iso} O	2.6(9)	-1.6(5)	2.3(7)	4.1(8)	4.0(13)
z_{Br}	0.17825(19)	0.17738(25)	0.17713(18)	0.17781(20)	0.17886(26)
U_{iso} Br	1.38(18)	2.47(21)	2.89(17)	2.33(15)	2.08(26)
a / Å	4.00606(16)	4.02537(13)	4.03454(14)	4.04721(10)	4.06238(16)
c / Å	17.0167(8)	16.8882(7)	16.7885(7)	16.6975(5)	16.5832(8)
R_p	1.399	1.123	0.893	0.820	0.771
R_{wp}	1.863	1.609	1.154	1.044	0.996
χ^2	3.003	2.645	1.647	1.479	1.417

Table 4.3. Derived bond lengths of note for $Sr_2Cu_{1-y}Co_yO_2Cl_2$, esd's are given in parentheses.

Compound	$Sr_2Cu_{0.8}Co_{0.2}O_2Cl_2$	$Sr_2Cu_{0.6}Co_{0.4}O_2Cl_2$	$Sr_2Cu_{0.5}Co_{0.5}O_2Cl_2$	$Sr_2Cu_{0.4}Co_{0.6}O_2Cl_2$	$Sr_2Cu_{0.2}Co_{0.8}O_2Cl_2$
Bond					
Sr – O x 4	2.5968(26)	2.5961(30)	2.5965(29)	2.6043(33)	2.5940(40)
Sr – Cl x 4	3.0524(30)	3.0567(30)	3.0557(33)	3.0538(34)	3.0670(40)
Sr – Cl x 1	3.247(11)	3.245(11)	3.253(12)	3.240(13)	3.231(14)
Cu/Co – O x 4	1.99250(5)	2.00074(6)	2.00751(9)	2.01097(9)	2.01909(9)
Cu/Co – Cl x 2	2.839(8)	2.811(9)	2.777(9)	2.767(10)	2.750(11)

Table 4.4. Derived bond lengths of note for $Sr_2Cu_{1-y}Co_yO_2Br_2$, esd's are given in parentheses.

Compound	$Sr_2Cu_{0.8}Co_{0.2}O_2Br_2$	$Sr_2Cu_{0.6}Co_{0.4}O_2Br_2$	$Sr_2Cu_{0.5}Co_{0.5}O_2Br_2$	$Sr_2Cu_{0.4}Co_{0.6}O_2Br_2$	$Sr_2Cu_{0.2}Co_{0.8}O_2Br_2$
Bond					
Sr – O x 4	2.6256(28)	2.6240(29)	2.6203(20)	2.6172(23)	2.6251(31)
Sr – Br x 4	3.1318(26)	3.1342(30)	3.1357(21)	3.1471(24)	3.1543(32)
Sr – Br x 1	3.778(5)	3.765(5)	3.748(4)	3.720(4)	3.662(5)
Cu/Co – O x 4	2.00303(8)	2.01269(7)	2.01727(7)	2.02361(5)	2.03119(8)
Cu/Co – Br x 2	3.0332(33)	2.9960(40)	2.9738(30)	2.9690(33)	2.966(4)

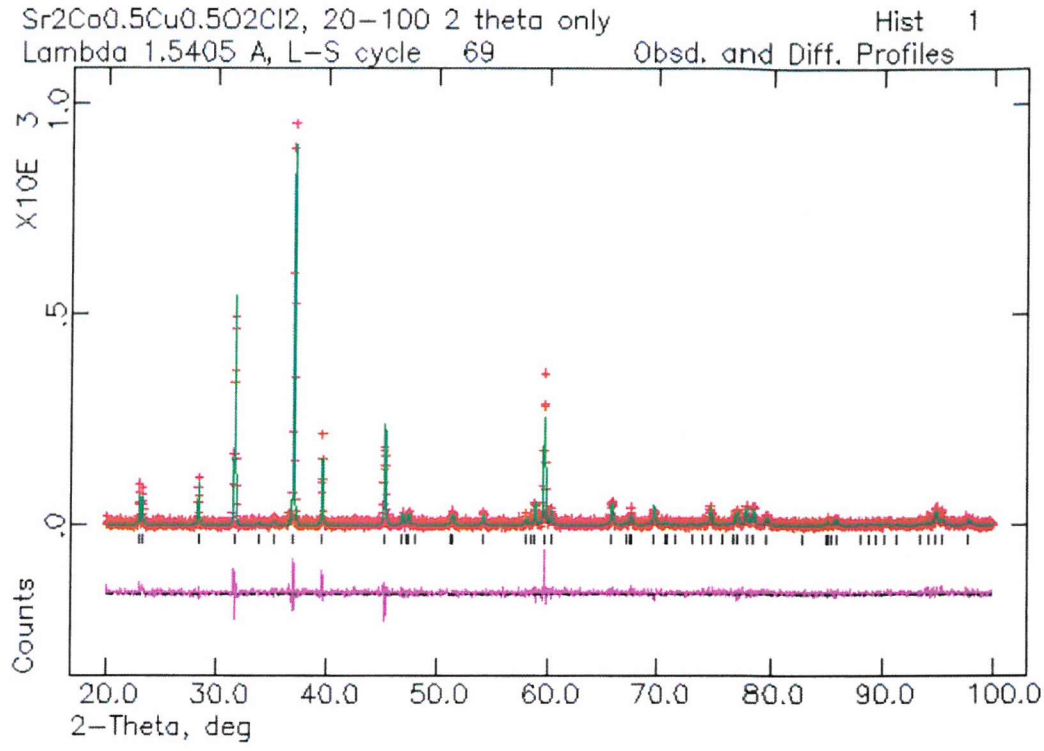

Figure 4.3.2a Profile fit as obtained to $Sr_2Cu_{0.5}Co_{0.5}O_2Cl_2$ data.

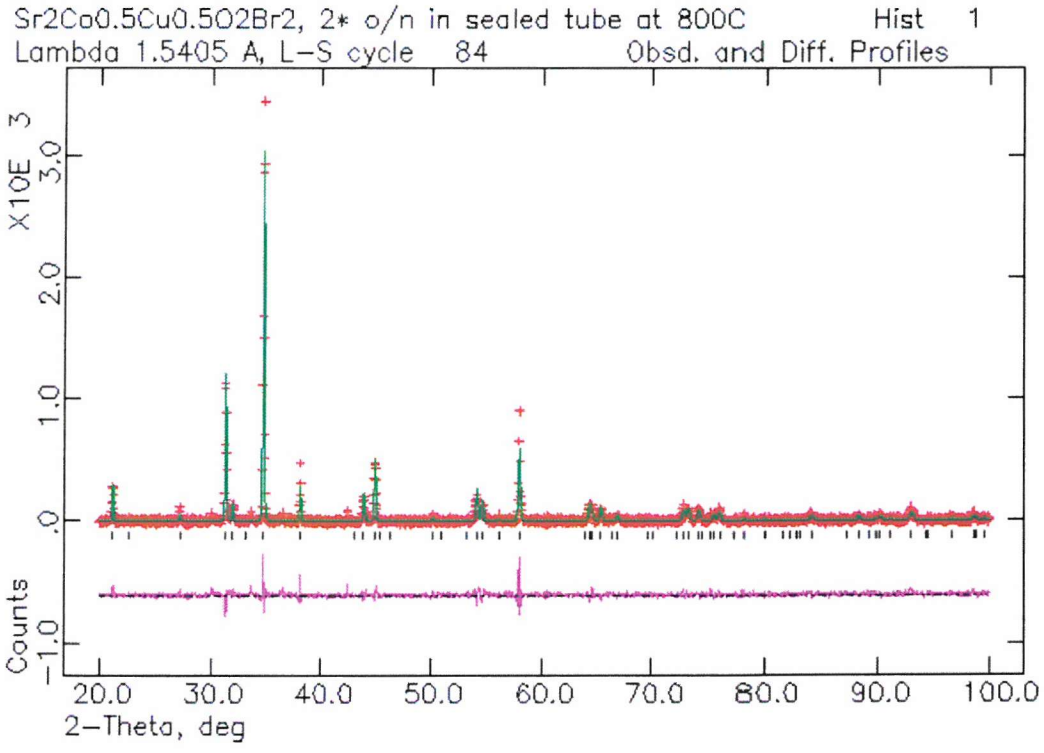

Figure 4.3.2b Profile fit as obtained to $Sr_2Cu_{0.5}Co_{0.5}O_2Br_2$ data.

4.4 Discussion

Complete solid solutions of $Sr_2Cu_{1-y}Co_yO_2Cl_2$ and $Sr_2Cu_{1-y}Co_yO_2Br_2$ (y = 0.2, 0.4, 0.5, 0.6, 0.8) have been synthesised by the direct reaction of the alkaline earth metal halide and oxide and cobalt and copper oxides in stoichiometric quantities. The sealed tube technique was used to prevent cobalt ions from oxidising to form cobalt (III), and to prevent loss of halide through sublimation. This technique can be very useful in enabling the stabilisation of products that would otherwise prove problematic to synthesise.

As expected the $Sr_2Cu_{1-y}Co_yO_2Cl_2$ and $Sr_2Cu_{1-y}Co_yO_2Br_2$ (y = 0.2, 0.4, 0.5, 0.6, 0.8) phases all adopt the structure of the end member phases, $Sr_2CuO_2X_2$ and $Sr_2CoO_2X_2$, (see Fig. 4.1a), the K_2NiF_4 structure type. The oxygen and halide ions order fully over the fluorine sites with the halide ions preferring to adopt the apical position of the Cu/CoO_6 distorted tetragonal/octahedra coordination (see Fig. 4.4a). The ordering of chloride and bromide ions within oxide halides has been known to occur in other related oxide halides, including oxide fluorides, e.g. Ba_2InO_3X (X = F, Cl, Br), $BaSrInO_3Cl$ and $Ba_4In_2SnO_8Cl_2$ [13], $Sr_{3-x}A_xAlO_4F$ [14]

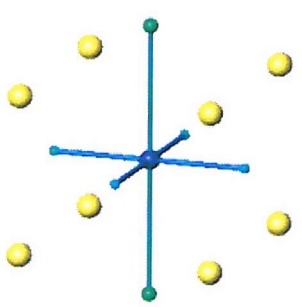

Figure 4.4a Representations of the Cu/CoO_4X_2 octahedra, highlighting the ordering of the anions (green spheres represent halide ions, pale blue spheres represent oxygen ions, dark blue ion represents copper/cobalt ion)

The refined cell parameters show the expected increase in the *a* parameter and decrease in the *c* parameter as the proportion of cobalt within the structure increases. Due to the increased size of cobalt in comparison to copper (Co (II) HS 0.745 Å, Cu (II) 0.73 Å) a gradual increase in the *a* parameter occurs as the smaller ion is progressively replaced with the larger ion. However, the same trend is not seen in the *c* parameter because the Jahn Teller effect causes a more significant change than the ionic radii of the metal ions. Copper (II) is subject to Jahn-Teller distortions and thus tends to have long axial bonds within

its distorted octahedra, hence as the proportion of the metal that causes lengthened axial Cu/Co–X bonds (in the c direction) decreases so does the c axis.

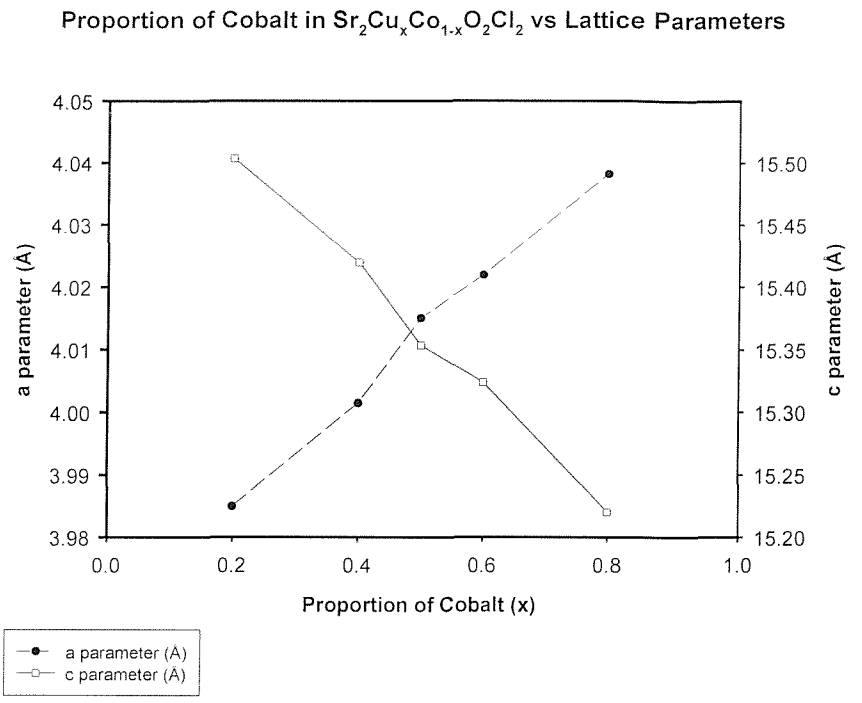

Figure 4.4a Graph showing the variation of lattice parameters with the proportion of cobalt in $Sr_2Cu_{1-y}Co_yO_2Cl_2$.

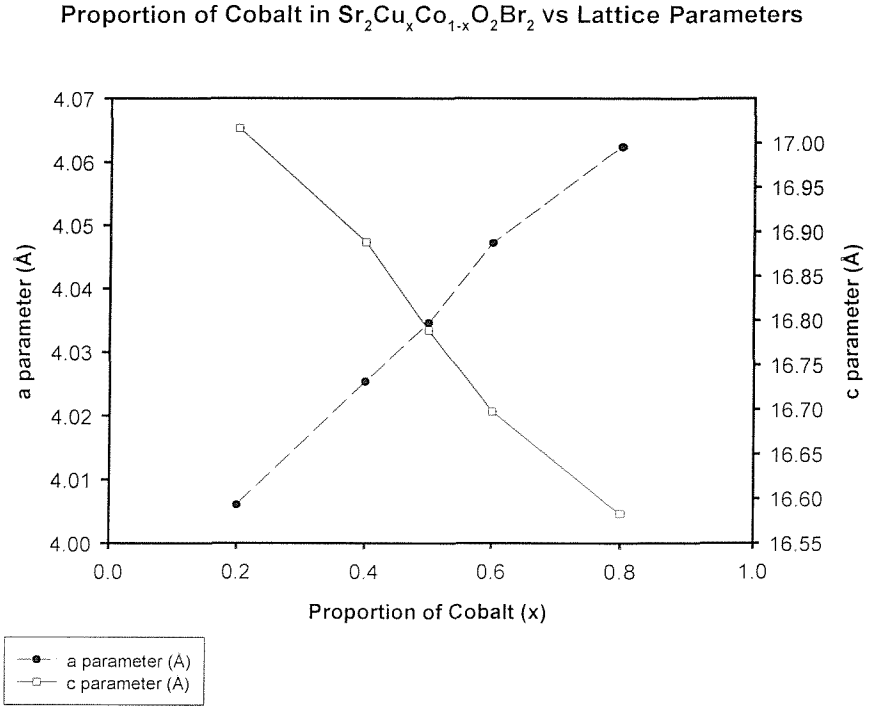

Figure 4.4b Graph showing the variation of lattice parameters with the proportion of cobalt in $Sr_2Cu_{1-y}Co_yO_2Br_2$.

As would be expected the oxide bromide phases consistently have greater cell parameters and bond lengths than the oxide chlorides as a result of replacing chloride ions (r (Cl^-) = 1.81 Å [15]) with the larger bromide ions (r (Br^-) = 1.96 Å [15]). The increases seen in $Sr_2Cu_{1-y}Co_yO_2X_2$ as the halide ion is changed from chloride to bromide are consistent with an approx. 0.5% difference in the a direction and approx. 9% difference in the c direction, as shown by the phases $Sr_2CoO_2Cl_2$ and $Sr_2CoO_2Br_2$. This effect can be demonstrated by comparing the Cu/Co–O and Cu/Co–X bond lengths for $Sr_2Cu_{0.5}Co_{0.5}O_2X_2$: as the X = Cl → Br the metal oxygen bonds (in the a direction) increase from 2.00751 Å to 2.01727 Å, whereas the metal halide bonds (in the c direction) increase from 2.777 Å to 2.974 Å.

The considerably greater increase along the c axis occurs because the length of the axial Cu/Co–X (X = Cl. Br) bonds are the bonds most affected by the change in halide ion (and as mentioned above, these bonds lie along the c direction). Another significant factor causing the *c* parameter to increase is the inter-layer repulsion between the bromide ions. This effect can be seen when comparing the change in the length of the single Sr–X bond to the change in length of the Sr–O bonds. The increase in ionic radius from Cl^- to Br^- can account for a 0.15 Å increase in the single Sr–X bond length; however the bond increases by a significantly greater amount; 0.495 Å. The length of the Sr–O bond remains almost unchanged with an increase of only 0.0238 Å.

As all of the four possible end member phases are known, $Sr_2CuO_2Cl_2$ [9], $Sr_2CuO_2Br_2$ [10], $Sr_2CoO_2Cl_2$ [11] and $Sr_2CoO_2Br_2$ [11], the graphs that follow include data points for these phases as well as for the phases synthesised within this work. (Please note that error bars are not visible for M–O bond lengths as they are too small to be distinguished beneath the data points). The literature data is displayed for comparative purposes, but as the experimental conditions are different from those under which the solid solutions were synthesised, the values used should be treated with a degree of caution (especially as some of the data used is from single crystal studies, as is the case for $Sr_2CoO_2Br_2$).

Please note that the greater electron density of the bromide, in comparison with the chloride, means that the bromide ions are easier to locate within the $Sr_2Cu_{1-y}Co_yO_2X_2$ structure, and thus the errors associated with their positions are lessened (and therefore their error bars shorter).

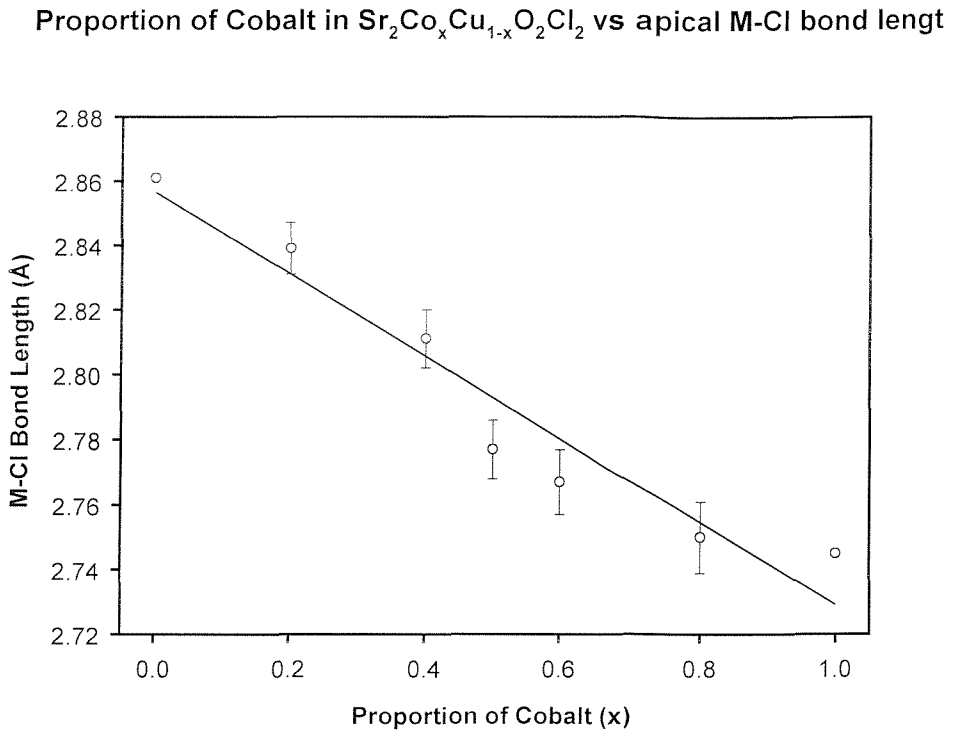

Figure 4.4c Graph showing the variation of M–Cl bond length with the proportion of cobalt in $Sr_2Cu_{1-y}Co_yO_2Cl_2$.

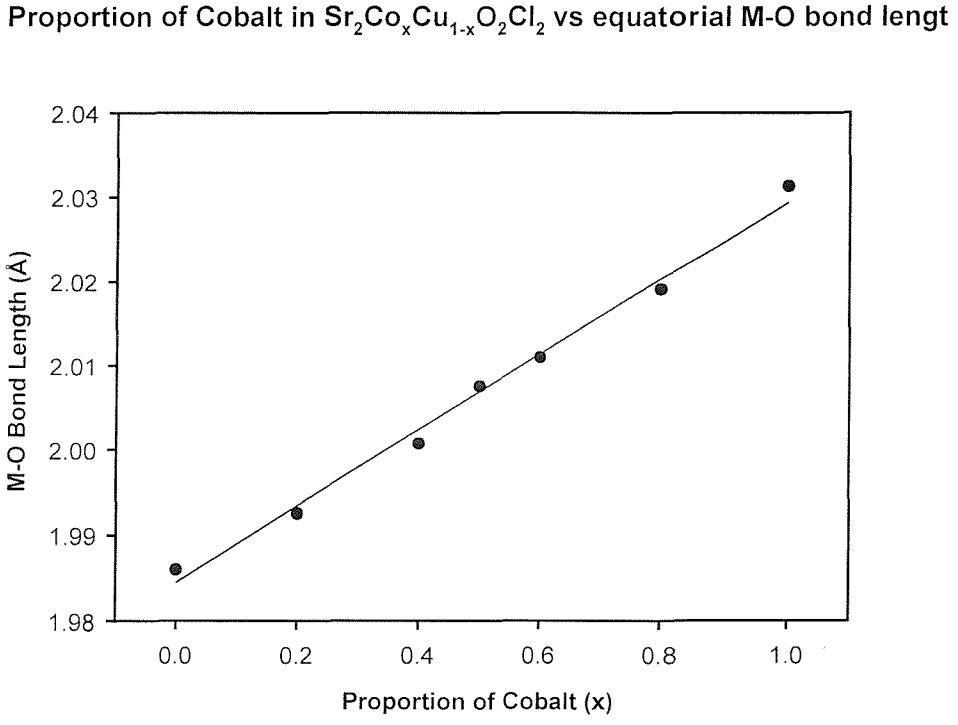

Figure 4.4d Graph showing the variation of M–O bond length with the proportion of cobalt in $Sr_2Cu_{1-y}Co_yO_2Cl_2$.

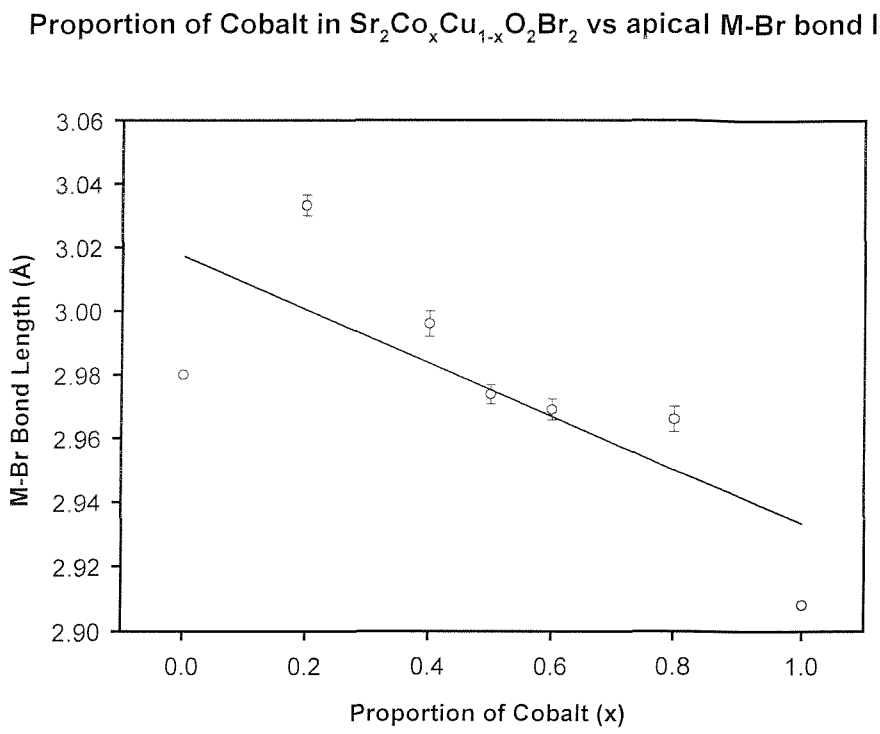

Figure 4.4e Graph showing the variation of M–Br bond length with the proportion of cobalt in $Sr_2Cu_{1-y}Co_yO_2Br_2$.

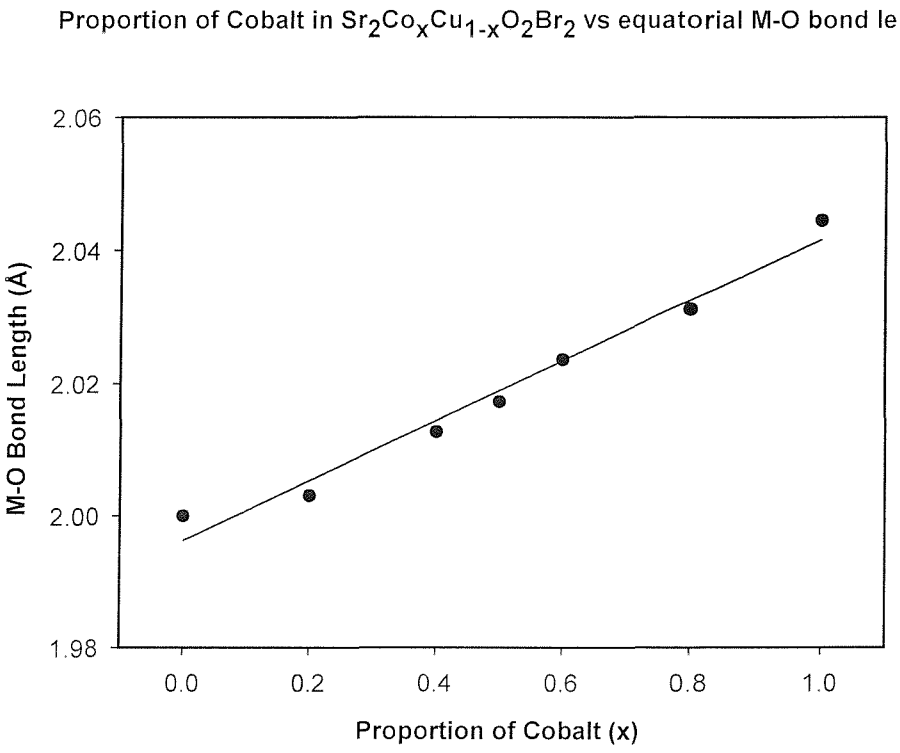

Figure 4.4f Graph showing the variation of M–O bond length with the proportion of cobalt in $Sr_2Cu_{1-y}Co_yO_2Br_2$.

The errors generated by structural refinement programs are thought to be unrealistically low [16], with this taken into account it is reasonable to conclude that the bond lengths do fit the trend lines given. Thus it would appear to be clear that there is a smooth change in bond length associated with the replacement of copper by cobalt, in obeyance with Vegard's law [17]. This gradual change in bond lengths is indicative of a gradual decrease in the Jahn Teller effect as the copper is replaced with cobalt. Such a trend is consistent with that seen in the solid solution of $Co_{3-x}Cu_x(PO_4)_2$ [6], but not with the sudden structural change seen in the $YBa_2Cu_{3-x}Co_xO_{7-\delta}$ [3] solid solution as studied by Voronin et al. This might suggest that when the metals whose proportions are being altered possess a single valency (i.e. are not multivalent) their solid solutions are more likely to adopt a smooth structural transition and display gradual structural changes.

The strontium bond lengths for these phases compare well with those of another cobalt oxide halide of similar stoichiometry, i.e. Sr_2CoO_3Cl [18] (e.g. Sr–Cl = 3.266 Å and 2.969 Å in Sr_2CoO_3Cl, and 3.231 Å and 3.0670 Å in $Sr_2Cu_{0.2}Co_{0.8}O_2Cl_2$). However, the copper/cobalt bond lengths are considerably different in these two phases (e.g. Co–Cl = 3.12 Å in Sr_2CoO_3Cl and Cu/Co–Cl = 2.750 Å in $Sr_2Cu_{0.2}Co_{0.8}O_2Cl_2$). This may reflect the greater degree of distortion associated with having a single halide ion forming an octahedron, rather than the symmetrical di-halide distortion associated with the $Sr_2Cu_{1-y}Co_yO_2X_2$ structure, or this could result from the different oxidation states of the cobalt ions present in the two phases (Co^{2+} in $Sr_2Cu_{1-y}Co_yO_2X_2$, Co^{3+} in Sr_2CoO_3Cl).

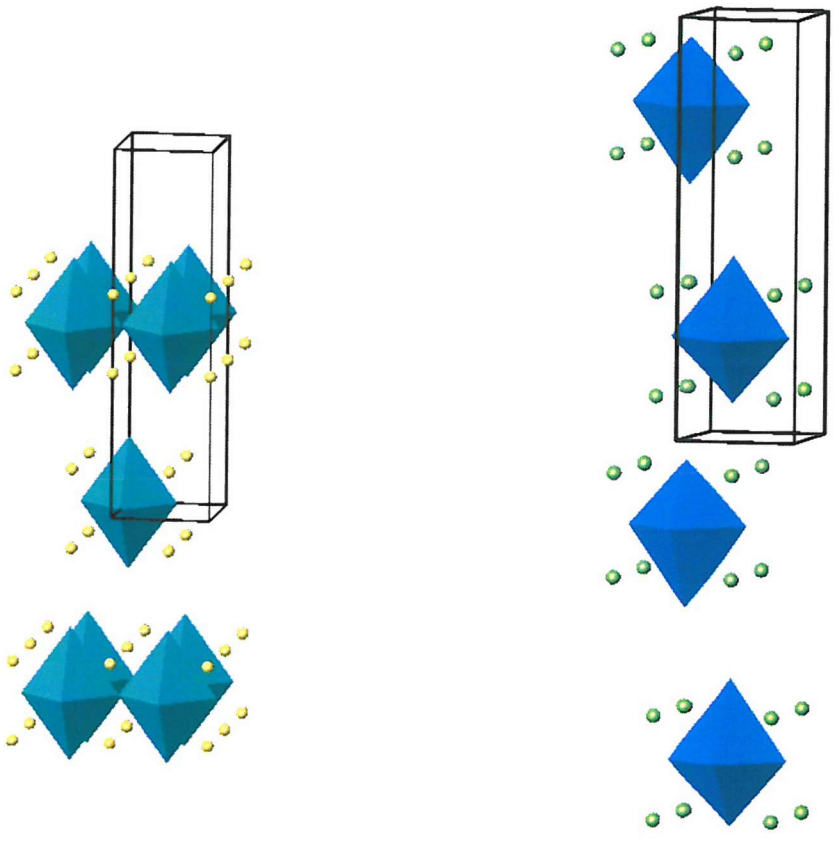

Figure 4.4g Representations of the structures of $Sr_2Cu_{1-y}Co_yO_2X_2$ and Sr_2CoO_3Cl (unit cells highlighted)

4.5 Conclusions

Solid solutions of $Sr_2Cu_{1-y}Co_yO_2Cl_2$ and $Sr_2Cu_{1-y}Co_yO_2Br_2$ (y = 0.2, 0.4, 0.5, 0.6, 0.8) have been synthesised and their structures characterised by PXD. The oxide bromide phases consistently have greater cell parameters and bond lengths than the oxide chlorides.

The cell parameters change as the copper ion is replaced by cobalt, with a steady increase in the *a* parameter and gradual decrease in the *c* parameter. This trend reflects the fact that copper (II) is a Jahn Teller ion whereas high spin cobalt (II) is not and therefore does not form lengthened axial bonds within its octahedra. The even trend in change in bond length that occurs as copper is replaced by cobalt, suggests a gradual decrease in the Jahn Teller effect

The coordination environments of the strontium ions in Sr_2CoO_3Cl and $Sr_2Cu_{1-y}Co_yO_2X_2$ are comparable, whereas the copper/cobalt octahedron being more distorted in Sr_2CoO_3Cl has quite different bond lengths to those in $Sr_2Cu_{1-y}Co_yO_2Cl_2$.

The phase $Sr_2CoO_2Cl_2$ orders antiferromagnetically at approx. 220 K [12], whereas $Sr_2CuO_2Cl_2$ orders antiferromagnetically at approx. 270 K [19]. As the structural transitions that result from replacing copper with cobalt in the phases $Sr_2Cu_{1-y}Co_yO_2X_2$ (X = Cl, Br) would appear to be gradual and smooth it would seem sensible to suggest that magnetic ordering would vary as the proportion of cobalt increased, with the Néel temperature of the material lowering steadily. This gradual change in antiferromagnetic behaviour has also been observed in other copper/cobalt solid solutions, such as $LaCo_{1-x}Cu_xO_3$ [4].

In order for changes in magnetic behaviour to be accurately determined, magnetic susceptibility measurements and powder neutron diffraction studies would need to be carried out.

4.6 References

1 Frand G, Bohnke O, Lacorre P, Fourquet J L, Carre A, Eid R, Theobald J G, Gire A, *J. Solid State Chem.*, 1995, **120**, 157

2 Tarascon J M, Barboux P, Miceli P F, Greene L H, Hull G W, Eibschutz M, Sunshine S A, *Phys. Rev. B*, 1988, **37**, 7458

3 Voronin V I, Goshchitskii B N, Mitberg E B, Leonidov I A, Kozhevnikov V L, *J. Struct. Chem.*, 2000, **41**, 626

4 Porta P, de Rossi S, Faticanti M, Minelli G, Pettiti I, Lisi L, Turco M, *J. Solid State Chem.*,1999, **146**, 291

5 Lappas A, Prassides K, *J. Solid State Chem.*, 1994, **108**, 59

6 Bamberger C E, Specht E D, Anovitz L M, *J. Am. Ceram. Soc.*, 1998, **81**, 2799

7 Widmann A, Kahlert H, Petrovic-Prelevic I, Wulff H, Yakhmi J V, Bagkar N, Scholz F, *Inorg. Chem.*, 2002, **41**, 5706

8 Von Grande B, Müller-Buschbaum H K, *Z. Anorg. Allg. Chem.*, 1977, **429**, 88

9 Von Grande B, Müller-Buschbaum H K, *Z. Anorg. Allg. Chem.*, 1975, **417**, 68

10 Miller L L, Wang X L, Wang S X, Stassis C, Johnston D C, Faber Jnr J, Loong C-K; *Phys. Rev. B*, 1990, **41**, 1921; Von Grande B, Müller-Buschbaum H K, *Z. Anorg. Allg. Chem.*, 1977, **433**, 152

11 Knee C S, Weller M T, *J. Solid State Chem.*, 2002, **168**, 1

12 Knee C S, Weller M T, *Solid State Sci.*, in press

13 Needs R L, PhD Thesis, University of Southampton, 1997

14 Prodjosantoso A K, Kennedy B J, Vogt T, Woodward P M, *J. Solid State Chem.*, 2003, **172**, 89

15 Shannon R D, *Acta Cryst.*, 1976, **A32**, 751

16 McCusker L B, Von Dreele R B, Cox D E, Louër D, Scardi P, *J. Appl. Cryst.*, 1999, **32**, 36

17 Vegard L, *Z. Phys.*, 1921, **5**, 17

18 McGlothlin N, Ho D, Cava R J, Mater. Res. Bull., 2000, **35**, 7, 1035; Loureiro S M, Felser C, Huang Q, Cava R J, Chem. Mater., 2000, **12**, 10, 3181

19 Keimer B, Aharony A, Auerbach A, Birgeneau R J, Cassanho A, Endoh Y, Erwin R W, Kastner M A, Shirane G, *Phys. Rev. B*, 1992, **45**, 7430

Chapter Five

Synthesis and Magnetic Structure Determination of $Sr_3Fe_{2-y}Co_yO_5X_2$ (X = Cl and Br, y = 0, 1, 2)

5.1 Introduction

The area of first row transition metal oxide halide chemistry has recently undergone a rapid expansion with the synthesis of several new cobalt [1, 2] and manganese phases [3] that adopt structures closely related to the technologically important high T_c and CMR Ruddlesden – Popper materials. Significant advances have also been made by Wiley and co-workers who have obtained a number of compounds described by the formula (MCl)$LaNb_2O_7$, *e.g.* M = Cu [4] and Cr, Mn, Fe, Co [5] through low temperature topotactic reactions. The newly synthesised Ruddlesden – Popper oxide halides include the cobalt (III) materials, Sr_2CoO_3Cl and $Sr_2Co_2O_5Cl_2$, reported by Cava and co-workers [1] and the cobalt (II) phases $Sr_2CoO_2X_2$ (X = Cl and Br) reported by Knee and Weller [2] (mixed metal solid solutions of which were discussed in chapter four). These materials all adopt Ruddlesden – Popper related structures in which either one, e.g. Sr_2MnO_3Cl [3], *or both, e.g.* $Sr_3Co_2O_5Cl_2$ [1] *of the terminal apical oxygen positions of* the repeat perovskite block have been replaced by a halide ion.

Leib and Müller-Buschbaum reported the first Ruddlesden – Popper alkaline earth iron oxide chloride, $Sr_3Fe_2O_5Cl_2$, in 1984 [6]. Ackerman later isolated a variety of alkaline earth iron oxide halide single crystals grown from fluxes of the respective alkaline earth halide (including the calcium and bromide analogues of the parent phase; $Ca_3Fe_2O_5Cl_2$ and $Sr_3Fe_2O_5Br_2$) [7], whilst the cobalt analogue of the parent phase, $Sr_3Co_2O_5Cl_2$, was synthesised by Cava [8].

The results of Mössbauer measurements [7] performed on the single crystals of $Sr_3Fe_2O_5X_2$ (X = Cl and Br) indicated the presence of magnetic order within the materials at 300 K. More recently, powder neutron diffraction studies by Hector et al. have revealed the antiferromagnetic spin structure of the single layer, K_2NiF_4-type, oxide fluoride Sr_2FeO_3F [9], whilst Parthé and Hu have re-determined the crystal structures of two phases synthesised by Ackerman $CaFeO_2Cl$ and Ca_2FeO_3Cl [10].

The Ruddlesden – Popper transition metal oxide halides all contain linked metal oxide sheets found in the equivalent oxides, as required for correlated electronic behaviour, and this makes them ideal systems in which to study the key magnetic interactions that facilitate transport phenomena. For example, a significant level of effort has been directed towards understanding the magnetic

interactions within the manganese Ruddlesden – Popper magnetoresistance materials and the role they play in the CMR effect. The competing ferro- and antiferromagnetic exchange coupling that occurs due to the presence of varying levels of Mn^{3+} and Mn^{4+} ions, as well as the increased two-dimensional (2D) character of the materials when compared with perovskites, leads to a variety of magnetic structures being adopted. In particular, the bi-layer $La_{2-2x}Sr_{1+2x}Mn_2O_7$ system exhibits a range of spin structures, including a canted ferromagnetic arrangement for x = 0.40-0.45 [11] and a G-type antiferromagnetic spin structure for the x = 1, Mn (IV) phase $Sr_3Mn_2O_7$ [12]. Studies of the magnetic properties and spin structures of other related multi-layer perovskites, such as the iron containing $YBa_2Cu_3O_{7-\delta}$ analogue $YBa_2Fe_3O_{8+y}$ [13] have also been valuable in increasing the understanding of the unique role copper has in high T_c superconductivity.

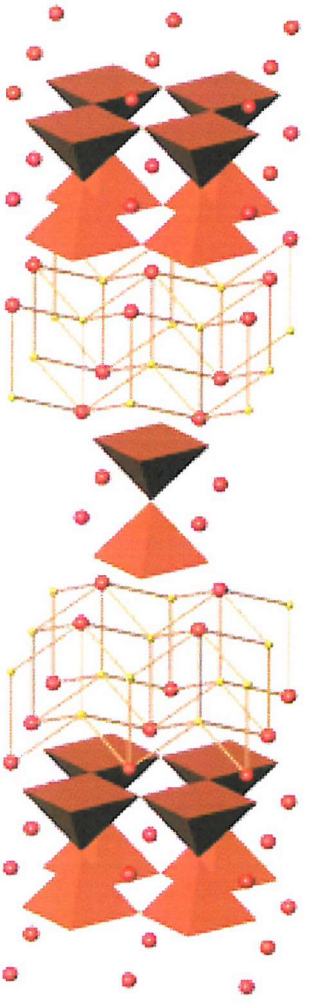

Figure 5.1a Representation of the $Sr_3Fe_{1-y}Co_yO_5X_2$ structure with Fe/CoO_5 square based pyramids

Using the parent structure $Sr_3Fe_2O_5Cl_2$, this work has explored the structural effects of halide and cobalt substitution upon crystal structure and sublattice magnetisation, including temperature dependence, through a PND study of the phases $Sr_3Fe_2O_5Cl_2$, $Sr_3Fe_2O_5Br_2$, $Sr_3Co_2O_5Cl_2$ and the previously unreported phase $Sr_3FeCoO_5Cl_2$.

5.2 Experimental Procedure

Polycrystalline samples of $Sr_3Fe_2O_5Cl_2$ and $Sr_3Fe_2O_5Br_2$ were prepared by intimately grinding together a 2:1:1 mixture of high purity SrO (from $SrCO_3$ at 1050 °C, 4 days), SrX_2, X = Cl and Br and Fe_2O_3 (all 99.9% or better), sealing the reactants in evacuated silica ampoules under vacuum and heating at 850 °C for 48 hours with a single interruption to regrind the products. All sample preparations were performed inside a glove box (< 1 ppm O_2/H_2O) due to the hygroscopic nature of some of the starting materials. Phase purity of the products (both $Sr_3Fe_2O_5Cl_2$ and $Sr_3Fe_2O_5Br_2$ were rusty red in colour) was checked by PXD using a Siemens D5000 diffractometer operating with Cu $K_{\alpha 1}$ radiation. The $Sr_3Fe_2O_5Cl_2$ pattern was consistent with phase pure product material, whereas the $Sr_3Fe_2O_5Br_2$ sample was found to contain an impurity at a level of < 5 % ($I:I_0$) (for results, see Table 5.3.1a).

The $Sr_3Fe_2O_5Br_2$ sample was not exposed to atmospheric conditions at any point, as previous experience with handling oxide bromides have shown their potential for slow hydrolysis.

The synthesis of $Sr_3FeCoO_5Cl_2$ and $Sr_3Co_2O_5Cl_2$ required a slightly more complex approach, to ensure the final product contained cobalt (III). Thus the precursor $Sr_2Co_2O_5$ [14] was reacted with SrO, Fe_2O_3 and $SrCl_2$ in the molar ratio 1:2:1:2 and 1:0:0:1, to form the mixed metal and pure cobalt phases respectively, and a heating regime used identical to that for the pure Fe materials. Once more, all sample preparations were carried out inside a glove box (<1 ppm O_2/H_2O) and phase purity for the phases ($Sr_3FeCoO_5Cl_2$ was dark grey/black in colour, whilst $Sr_3Co_2O_5Cl_2$ was black) was checked by PXD using a Siemens D5000 diffractometer operating with Cu $K_{\alpha 1}$ radiation. The patterns were consistent with phase pure product material (for results, see Table 5.3.1b).

Other analogues of the parent $Sr_3Fe_2O_5Cl_2$ phase were attempted including the oxide fluoride equivalent $Sr_3Fe_2O_5F_2$. The reactants $SrCO_3$, Fe_2O_3 and $SrF_2.6H_2O$ (all 99.9% or better) were prepared by intimately grinding together and heating to 800 °C for 2 ½ hours, regrinding the intermediates, and heating again to 800 °C for approx. 3 days with a single interruption to regrind the products (for results, see Table 5.3.1c).

The sealed tube technique, as detailed above, was used to try to synthesise the calcium analogues, $Ca_3Fe_2O_5Cl_2$ and $Ca_3Fe_2O_5Br_2$, but using CaO, $CaCl_2$ and $CaBr_2$ (Aldrich 99.99 %) in place of $SrCO_3$, $SrCl_2$ and $SrBr_2$ (for results, see Table 5.3.1d).

The synthesis of one final analogue related to the parent phase, the solid solution $Sr_3Fe_{1.5}Co_{0.5}O_5Cl_2$, was also tried. This synthesis also employed the sealed tube technique, as detailed above, but using a molar ratio of 1:4:6:3 of the reactants $Sr_2Co_2O_5$ [15], SrO, Fe_2O_3 and $SrCl_2$ (for results, see Table 5.3.1e).

Time of flight PND data were collected using the medium resolution POLARIS diffractometer at the ISIS facility in the UK. The $Sr_3Fe_2O_5Cl_2$ sample was loaded into an air-tight vanadium can in a helium gas atmosphere and data collection performed at room temperature (295 K), 17 K, 150 K, 400 K, 500 K, 550 K, 600 K and 625 K using a hot-stage / closed cycle refrigerator. Further scans were obtained for $Sr_3Fe_2O_5Br_2$, $Sr_3FeCoO_5Cl_2$ and $Sr_3Co_2O_5Cl_2$, at room temperature and at 2 K inside a standard ISIS cryostat. A second set of time of flight PND data was also collected for the $Sr_3Co_2O_5Cl_2$ sample using the high resolution D2B diffractometer at the ILL facility in France at 2 K inside a standard ILL cryostat.

The diffraction data were analysed using the GSAS software package [16] with the structural models from previously reported X-ray analyses employed in initial cycles [6, 7]. The higher resolution C-bank data of POLARIS (d-spacing range 0.2 - 3.2 Å) was used for the structural refinements for all the phases whilst the magnetic structures of the materials were determined from the wider range (0.5 - 8.3 Å) lower resolution A-bank patterns, for the phases $Sr_3Fe_2O_5Cl_2$, $Sr_3Fe_2O_5Br_2$ and $Sr_3FeCoO_5Cl_2$.

5.3 Results, including Structural Refinement

5.3.1 Synthetic Results

The known phases $Sr_3Fe_2O_5Cl_2$ and $Sr_3Fe_2O_5Br_2$, both formed as planned:

Target Phase	Reagents	Heat Treatment	Products
$Sr_3Fe_2O_5Cl_2$	SrO, Fe_2O_3 and $SrCl_2$	~18h at 850 °C	90% $Sr_3Fe_2O_5Cl_2$ and 10% Sr_2FeO_3Cl
		~18h at 850 °C	100% $Sr_3Fe_2O_5Cl_2$
$Sr_3Fe_2O_5Br_2$	SrO, Fe_2O_3 and $SrBr_2$	~18h at 850 °C	60% $Sr_3Fe_2O_5Br_2$ and 40% Sr_2FeO_3Br
		~18h at 850 °C	> 95% $Sr_3Fe_2O_5Br_2$ and < 5% $SrFeO_{2.86}$

Table 5.3.1a Sealed tube synthesis of $Sr_3Fe_2O_5X_2$ (X = Cl, Br)

The cobalt analogues of the parent phase, $Sr_3FeCoO_5Cl_2$ and $Sr_3Co_2O_5Cl_2$ were both made as phase pure products:

Target Phase	Reagents	Heat Treatment	Products
$Sr_3FeCoO_5Cl_2$	$Sr_2Co_2O_5$, SrO, Fe_2O_3 and $SrCl_2$	~18h at 850 °C	90% $Sr_3Fe_2O_5Cl_2$ and 10% Sr_2FeO_3Cl
		~18h at 850 °C	100% $Sr_3Fe_2O_5Cl_2$
$Sr_3Co_2O_5Cl_2$	$Sr_2Co_2O_5$, SrO, Fe_2O_3 and $SrBr_2$	~18h at 850 °C	60% $Sr_3Fe_2O_5Br_2$ and 40% Sr_2FeO_3Br
		~18h at 850 °C	> 95% $Sr_3Fe_2O_5Br_2$ and < 5% $SrFeO_{2.86}$

Table 5.3.1b Sealed tube synthesis of $Sr_3Fe_{2-x}Co_xO_5X_2$ (X = 1, 2)

Unfortunately the oxide fluoride analogue, $Sr_3Fe_2O_5F_2$ did not form, the single layer compound Sr_2FeO_3F formed instead:

Target Phase	Reagents	Heat Treatment	Products
$Sr_3Fe_2O_5F_2$	$SrCO_3$, Fe_2O_3 and $SrF_2.6H_2O$	2½h at 800 °C, reground, ~18h at 850 °C	80% Sr_2FeO_3F and 20% SrF_2
		~18h at 850 °C	85% Sr_2FeO_3F and 15% SrF_2

Table 5.3.1c Oxide fluoride analogue of $Sr_3Fe_2O_5Cl_2$

Once again the desired calcium analogues of the parent phases, $Ca_3Fe_2O_5Cl_2$ and $Ca_3Fe_2O_5Br_2$ did not form, a mixture of $Ca_2Fe_2O_5$ and simple oxides and oxide halides formed instead:

Target Phase	Reagents	Heat Treatment	Products
$Ca_3Fe_2O_5Cl_2$	CaO, Fe_2O_3 and $CaCl_2$	~18h at 850 °C	65% $Ca_2Fe_2O_5$ and 35% $CaCl_2$
		~18h at 850 °C	as above
$Ca_3Fe_2O_5Br_2$	CaO, Fe_2O_3 and $CaBr_2$	~18h at 850 °C	amorphous
		~18h at 850 °C	45% Fe_2CaO_4, 35% $Ca_2Fe_2O_5$ and 20% $CaBr_2$

Table 5.3.1d Attempted sealed tube synthesis of calcium analogues of $Sr_3Fe_2O_5Cl_2$ and $Sr_3Fe_2O_5Br_2$

Unfortunately the related solid solution compound, $Sr_3Fe_{1.5}Co_{0.5}O_5Cl_2$ also did not form, a mixture of the single layer compound Sr_2FeO_3Cl and simple oxides formed instead:

Target Phase	Reagents	Heat Treatment	Products
$Sr_3Fe_{1.5}Co_{0.5}O_5Cl_2$	$SrCO_3$, Fe_2O_3 and $SrF_2.6H_2O$	~18h at 850 °C	55% Sr_2FeO_3Cl, 30% $Sr_3Fe_2O_5Cl_2$ and 15% CoO
		~18h at 850 °C	45% Sr_2FeO_3Cl, 45% Fe_3O_4 and 10% SrO

Table 5.3.1e Attempted sealed tube synthesis $Sr_3Fe_{1.5}Co_{0.5}O_5Cl_2$

5.3.2 Structural Investigation

5.3.2.1 Crystal Structure

The initial crystal structure refinement was carried out using the room temperature $Sr_3Fe_2O_5Cl_2$ data. The least squares analysis converged quickly to provide a good fit to the diffraction pattern, with the notable exception of a few weak magnetic peaks that were subsequently fitted with the model discussed in section 5.3.2.2 below. The only anomaly was a rather large isotropic atomic thermal displacement parameter for the apical O(1) oxygen located on the (0,0,½) site (U_{iso} = 1.18 x 100 Å^3), which indicated that either positional disorder or partial occupancy was present. The latter possibility was checked by allowing the fractional occupancy of the position to vary however this had only a negligible effect on the refinement statistics (U_{iso} = 1.34 x 100 Å^3, fractional occupancy = 1.04) and the site remained at full occupancy. Introduction of a displaced oxygen position produced a small but appreciable improvement in the Rietveld fit (U_{iso} = 0.032 x 100 Å^3), this confirms the displacement of oxygen from its formal position, and thus confirms the presence of oxygen disorder. A split (x,x,½) position was therefore introduced and refined to give x = 0.0265(8). In the final stages of the refinement the occupancies of all sites were allowed to vary and no significant deviation was observed confirming the phase to be of ideal stoichiometry. Analysis of the other variable temperature $Sr_3Fe_2O_5Cl_2$ data sets and those of $Sr_3Fe_2O_5Br_2$, $Sr_3FeCoO_5Cl_2$ and $Sr_3Co_2O_5Cl_2$ followed a similar method. For the bromide analogue the small level of impurity (identified as $SrFeO_{2.86}$) detected in the PXD scan was also apparent in the PND patterns. For the $Sr_3FeCoO_5Cl_2$ analyses the Fe:Co ratio was allowed to vary, to determine if the compound were truly stoichiometric, and indicated the presence of a small excess of iron. Refinement of an anisotropic oxygen position for the O(1) sites was only found to be necessary for the pure cobalt analogue, not for either the $Sr_3Fe_2O_5Br_2$ or $Sr_3FeCoO_5Cl_2$ refinements.

Refined atomic co-ordinates, lattice parameters and profile fit factors are summarised in Table 5.1. Table 5.2 summarises the derived bond lengths and angles of importance.

The final agreement achieved to the room temperature $Sr_3Fe_2O_5Cl_2$ and $Sr_3FeCo_2O_5Cl_2$ data is shown in Figures 5.3.2.1a and 5.3.2.1b respectively.

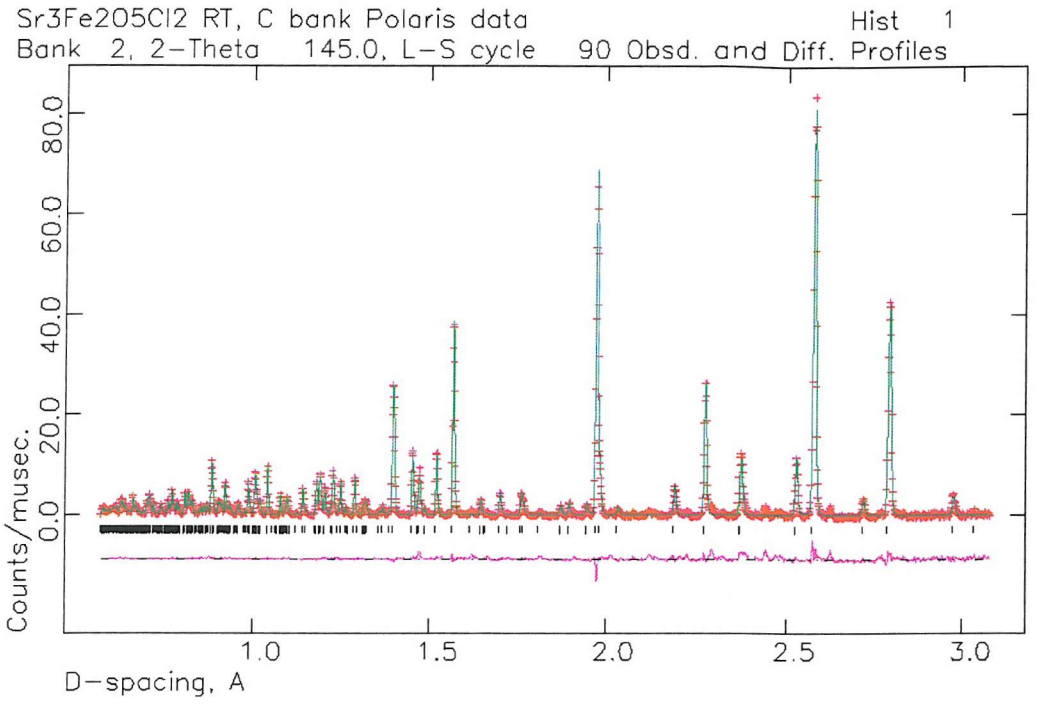

Figure 5.3.2.1a Profile fit as obtained to $Sr_3Fe_2O_5Cl_2$ 295 K C-bank data

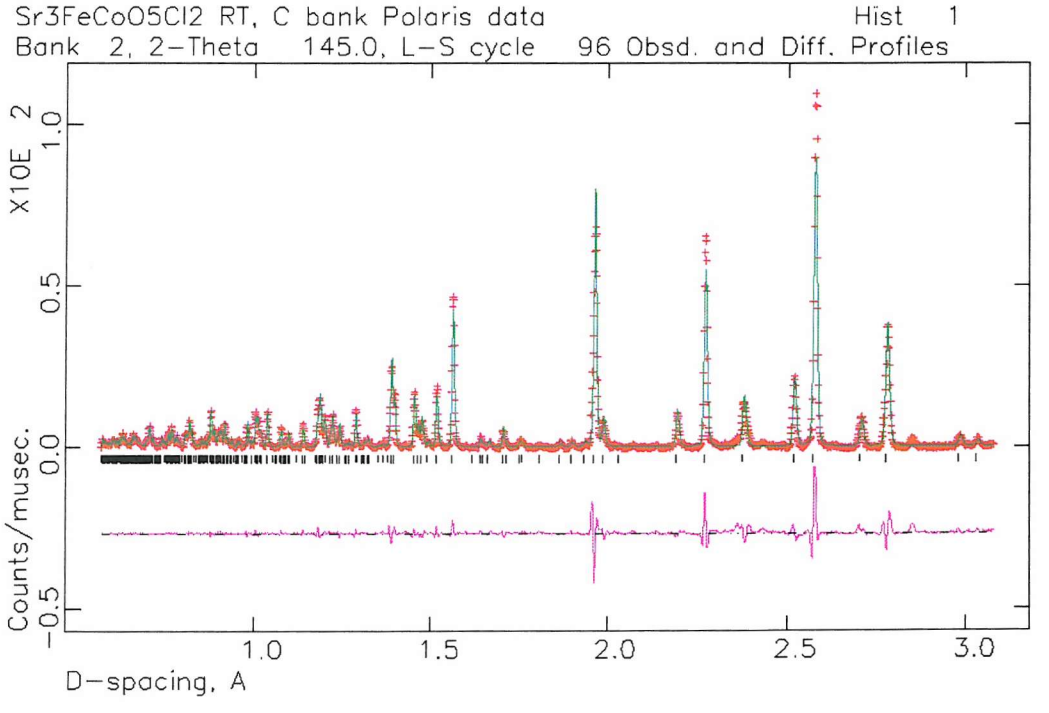

Figure 5.3.2.1b Profile fit as obtained to $Sr_3FeCo_2O_5Cl_2$ 295 K C-bank data.

Table 5.1 Refined atomic co-ordinates, lattice parameters and profile fit factors for $Sr_3Fe_{2-y}Co_yO_5X_2$ (y = 0, 1, 2, X = Cl, Br). Space group I4/mmm Sr(1) on (0,0,0), Sr(2) on (0,0,$z_{Sr(2)}$), Fe/Co on (0,0,z), O(1) on (x,x,½), O(2) on (½,0,z) and X on (0, 0,z_X). Thermal displacement parameters (all x 100, Å^2) for each atom sites are also given, values for Fe and Co were constrained to be equal, esd's are given in parentheses.

Compound	$Sr_3Fe_2O_5Cl_2$		$Sr_3Fe_2O_5Br_2$		$Sr_3FeCoO_5Cl_2$		$Sr_3Co_2O_5Cl_2$	
Temperature	17K	295K	2K	298K	2K	298K	2K	298K
U_{iso} Sr(1)	0.16(1)	0.82(2)	0.19(2)	0.83(4)	0.43(3)	0.93(3)	0.63(5)	1.13(6)
$z_{Sr(2)}$	0.15743(3)	0.15717(4)	0.14664(4)	0.14647(6)	0.15749(6)	0.15709(6)	0.15807(9)	0.15774(9)
U_{iso} Sr(2)	0.017(1)	0.53(1)	0.16(2)	0.45(2)	0.40(2)	0.65(2)	0.67(4)	0.94(4)
$z_{Fe/Co}$	0.42101(2)	0.42134(3)	0.42606(4)	0.42647(6)	0.42148(6)	0.42151(6)	0.42185(23)	0.42211(24)
U_{iso} Fe/Co	0.12(1)	0.39(1)	0.10(2)	0.33(3)	0.23(3)	0.34(3)	0.17(8)	0.65(9)
$x_{O(1)}$	0.0143(3)	0.0265(8)	-	-	-	-	0.0205(28)	0.0286(19)
U_{iso} O(1)	0.17(4)	0.32(5)	0.41(1)	0.94(4)	0.62(4)	0.99(4)	0.23(14)	0.23(14)
$z_{O(2)}$	0.09010(2)	0.08980(3)	0.08413(4)	0.08382(5)	0.08999(4)	0.08964(4)	0.09003(7)	0.08976(7)
U_{iso} O(2)	0.29(1)	0.60(1)	0.25(1)	0.65(2)	0.61(2)	0.93(2)	1.040(34)	1.51(4)
z_X	0.29498(2)	0.29532(3)	0.29935(5)	0.29987(8)	0.29471(5)	0.29511(5)	0.29428(7)	0.29443(8)
U_{iso} X	0.29(1)	0.81(1)	0.40(2)	1.00(3)	0.45(2)	0.94(2)	0.50(4)	0.99(5)
a / Å	3.93848(4)	3.94684(2)	3.94538(6)	3.95465(4)	3.91932(5)	3.92946(4)	3.90022(9)	3.91451(10)
c / Å	23.6902(3)	23.7971(2)	25.2833(5)	25.4146(5)	23.7782(5)	23.8766(4)	23.9054(8)	24.0184(7)
R_p	4.03	3.53	2.92	6.58	3.00	7.08	2.44	6.99
R_{wp}	2.22	2.02	1.84	5.98	1.70	3.50	1.31	3.49
χ^2	2.77	2.30	7.00	2.74	5.45	13.57	4.68	10.26

Table 5.2 Derived interatomic distances (Å) and bond angles (°) for $Sr_3Fe_2O_5Cl_2$, $Sr_3Fe_2O_5Br_2$, $Sr_3FeCoO_5Cl_2$ and $Sr_3Co_2O_5Cl_2$, esd's are given in parentheses.

Compound	$Sr_3Fe_2O_5Cl_2$		$Sr_3Fe_2O_5Br_2$		$Sr_3FeCoO_5Cl_2$		$Sr_3Co_2O_5Cl_2$	
Temperature	17K	295K	2K	298K	2K	298K	2K	298K
Sr(1)-O(1)* × 4	2.705(8)–2.865(8)	2.643(5)–2.939(5)	2.78981(4)	2.79636(3)	2.77137(3)	2.77855(3)	2.645(16)-2.871(16)	2.610(11)-2.926(11)
Sr(1)-O(2) × 8	2.9041(4)	2.9088(5)	2.9011(6)	2.9066(10)	2.9016(8)	2.9054(8)	2.9044(12)	2.9118(12)
Sr(2)-O(2) × 4	2.5343(6)	2.5425(6)	2.5277(8)	2.5386(12)	2.5330(10)	2.5404(10)	2.5394(16)	2.5489(16)
Sr(2)-X × 4	3.0045(3)	3.0112(4)	3.1061(7)	3.1112(10)	2.9954(6)	3.0038(6)	2.9839(9)	2.9969(10)
Sr(2)-X × 1	3.2584(9)	3.2877(11)	3.861(2)	3.899(3)	3.263(2)	3.296(2)	3.2557(31)	3.2830(32)
Fe/Co-O(1)* × 1	1.8730(6)	1.8778(7)	1.870(1)	1.869(1)	1.867(2)	1.874(1)	1.872(6)	1.878(6)
Fe/Co-O(2) × 4	1.9867(1)	1.9911(1)	1.9895(2)	1.9946(2)	1.9786(3)	1.9827(2)	1.9707(8)	1.9779(9)
Fe/Co-X × 2	2.9857(7)	2.9988(9)	3.204(1)	3.217(2)	3.015(2)	3.018(2)	3.050(6)	3.067(7)
O(2)-Fe/Co-O(2)	164.78(4)	164.70(5)	165.15(7)	164.93(10)	164.15(11)	164.57(10)	163.43(33)	163.4(4)

* indicates split (x,x,½) site for O(1) in the $Sr_3Fe_2O_5Cl_2$ and $Sr_3Co_2O_5Cl_2$ analyses

5.3.2.2 Magnetic structure determination

Inspection of the room temperature A-bank data for the $Sr_3Fe_2O_5Cl_2$, $Sr_3Fe_2O_5Br_2$ and $Sr_3FeCoO_5Cl_2$ phases revealed the presence of several moderately intense peaks in the *d*-spacing range 3-6 Å that could not be accounted for by the crystal structure. The high *d* position of the reflections suggested they were likely to be magnetic in origin and this was confirmed by their growth on cooling all samples below room temperature. The $Sr_3Fe_2O_5Br_2$ analysis revealed an additional weak peak at $d \approx 5.0$ Å, whose relative intensity was invariant with temperature and which was therefore assigned to a (non-magnetic) impurity in the sample.

The most intense magnetic peaks could be indexed as the reflections {10*l*}, with l = 1, 2, 3 and 4 on the basis of a magnetic cell related to the nuclear cell by $a_{mag} = b_{mag} = \sqrt{2}a_{nuc}$ and $c_{mag} = c_{nuc}$, consistent with a magnetic propagation vector $\underline{k} = (½, ½, 0)$. The magnetic intensity was modelled by introducing a second magnetic-only phase, and to allow for canting of the magnetic moments with respect to the four-fold rotational axis the spin structure was refined in space group *P*-1. A number of collinear ordering schemes for the Fe spins were investigated using the magnetic form factor for Fe^{3+} [17] and it quickly became apparent that the moments within these materials are coupled antiferromagnetically along all three crystallographic axes. Reasonable quality fits were obtained for models in which the moments were aligned parallel to the *z*-axis or confined to either the *x*- (or *y*-) direction within the *xy*-plane, although for both models some discrepancies between calculated and observed profiles were still apparent. A level of rotation of the spin direction was found to greatly enhance the agreement to the observed data for both scenarios; yielding a cant angle $\psi \approx 45°$ from the *z*-axis for the $Sr_3Fe_2O_5Cl_2$ analyses for the first model and an angle $\theta \approx 40°$ with respect to the *x*-axis for the second description and almost identical goodness of fit parameters. With little to differentiate the models in terms of agreement to the diffraction data the evidence from the previous Mössbauer measurements, which indicates that the Fe spins lie within the *xy*-plane [7], was used to discount the *z*-component model. The final agreement achieved to the low temperature $Sr_3Fe_2O_5Cl_2$ data is shown in Figures 5.3.2.2a, and details of all the refined magnetic moments are given in Table 5.3.

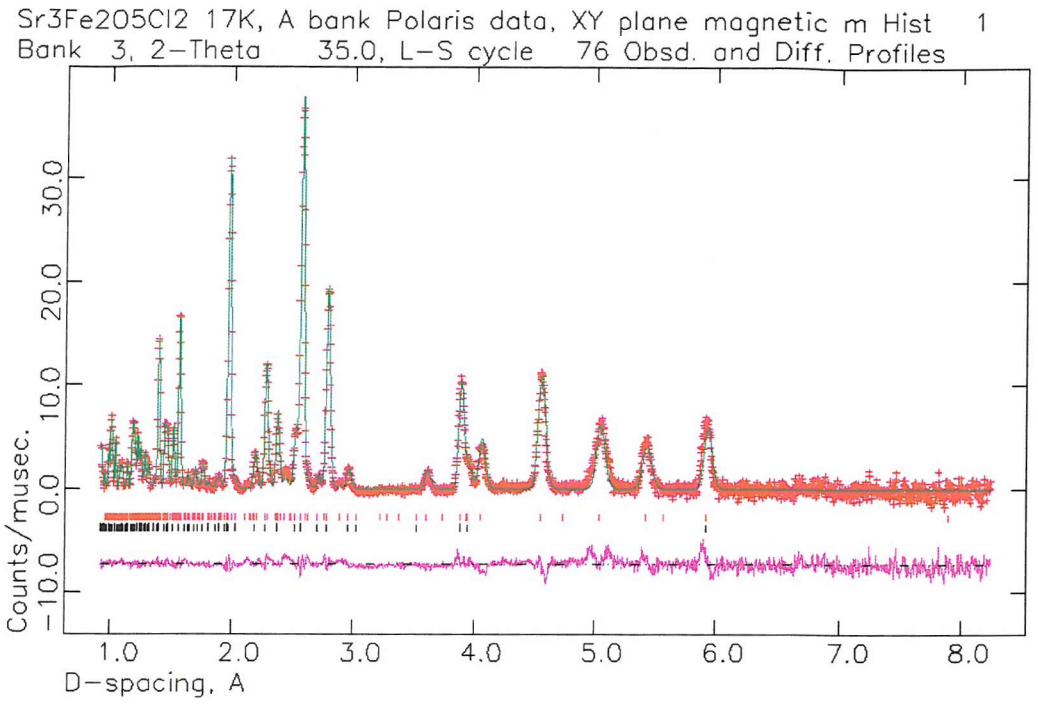

Figure 5.3.2.2a Profile fit as obtained to $Sr_3Fe_2O_5Cl_2$ 295 K C-bank data

Table 5.3 Refined magnetic parameters obtained from the A-bank of POLARIS. Magnetic space group *B112*/m; magnetic cell $a_{mag} = b_{mag} = \sqrt{2}a_{nuc}$, $c_{mag} = c_{nuc}$, $\beta = 90°$; Fe(/Co) on (¼, ¼, z) 8*j* site. Constraint $\mu_z = 0$.

Compound	$Sr_3Fe_2O_5Cl_2$		$Sr_3Fe_2O_5Br_2$		$Sr_3FeCoO_5Cl_2$	
Temperature	17K	295K	2K	298K	2K	298K
μ_x	3.61(4)	2.90(4)	3.12(6)	2.16(4)	1.55(5)	1.28(3)
μ_y	2.50(4)	2.36(5)	2.61(6)	2.20(4)	1.43(5)	1.20(3)
θ (°)	34.8(5)	39.1(7)	39.9(6)	45.5(9)	42.0(10)	43.0(10)
$\lvert\mu\rvert$ (μ_B)	4.40(4)	3.74(4)	4.07(6)	3.08(5)	2.11(4)	1.75(5)
R_p	5.08	5.19	3.12	6.34	2.89	4.48
R_{wp}	6.92	6.92	3.61	7.07	3.43	5.28
χ^2	1.24	1.28	1.72	4.20	1.34	2.02

Surprisingly both sets of data collected for the $Sr_3Co_2O_5Cl_2$ phase showed that no additional peaks were present in the *d*-spacing range 3-6 Å, and thus no magnetic structure refinement could be carried out for this structure.

5.4 Discussion

5.4.1 Crystal Structure

The structure of the $Sr_3Fe_{1-y}Co_yO_5X_2$ oxide halides as shown in Figure 5.1a consists of layers of opposing FeO_5 square pyramids, each pair linked through an oxygen with puckered double 'rocksalt' (SrX) layers separating their basal planes. Alternatively, the metal coordination can be viewed as infinite planes of highly distorted MO_5X octahedra if the extended metal to halide interaction is taken into account (see Fig. 5.4.1a).

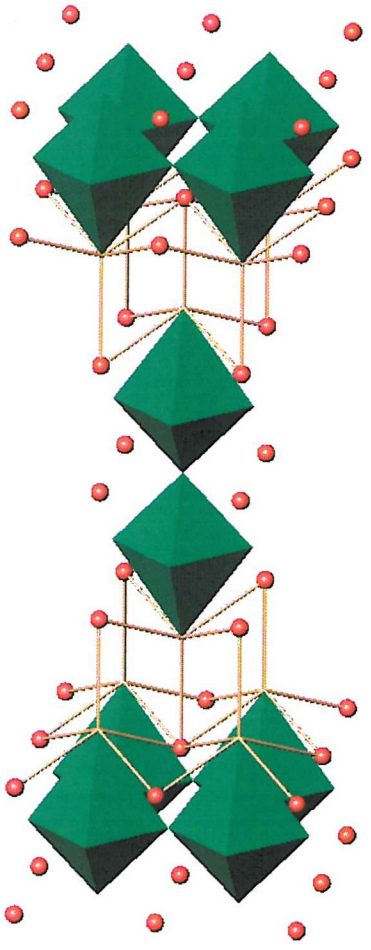

Figure 5.4.1a Representation of the $Sr_3Fe_{1-y}Co_yO_5X_2$ structure with Fe/CoO_5X octahedra

Our structural analyses have essentially confirmed the literature models determined from X-ray diffraction studies. The increased sensitivity of PND to oxygen positions has allowed the detection of a level of site disorder for the apical

O(1) site of $Sr_3Fe_2O_5Cl_2$ and $Sr_3Co_2O_5Cl_2$. This site links the layers of Fe/CoO_5 square pyramids and the displacement corresponds to static disorder of the oxygen of approximately 0.1 Å within the tetragonal plane (see Fig. 5.4.1b). Its effect on the Fe/Co-O(1) bond is small, as the bond distance changes from 1.8719(6) Å without the spilt site to 1.8778(6) Å in the case of the analysis of room temperature data for the pure iron phase, and from 1.866(6) Å to 1.878(6) Å for the pure cobalt phase.

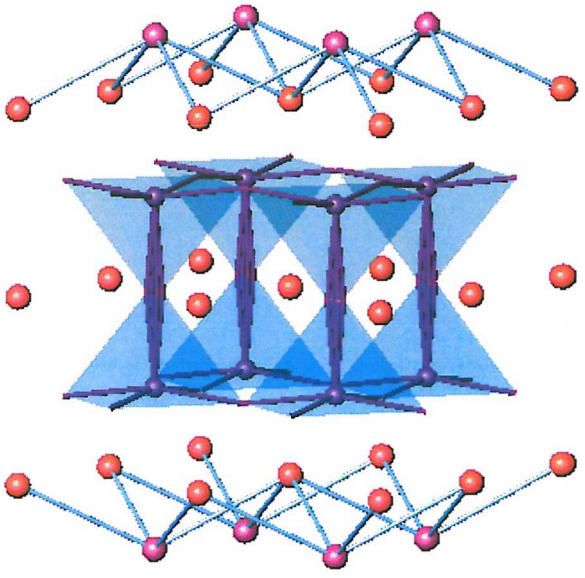

Figure 5.4.1b Representation of the $Sr_3Fe_{1-y}Co_yO_5Cl_2$ structure with distorted oxygens linking the Fe/CoO_5 polyhedra (red spheres represent strontium ions, pink spheres represent chloride ions and translucent blue square based pyramids represent iron/cobalt polyhedra)

The structural refinements have also confirmed the absence of significant anion (oxygen) deficiency within the phases and consequently the average metal valence state is confirmed as (III), which is consistent with the rusty red colour of the two pure iron phases.

5.4.2 Structural Trends

The room temperature cell constants of the $Sr_3Fe_2O_5X_2$ phases show the expected expansion when the chloride ion (r_{eff} = 1.81 Å) is replaced with the larger bromide ion (r_{eff} = 1.96 Å) [18]. The slight change in *a* ~ 0.002 % is minimal compared with the much larger 6.5 % elongation of the *c* parameter. The distance across the Fe-O(1)-Fe double perovskite layer within the materials remains constant within the constraints of experimental uncertainty, i.e. 3.744(3) Å for $Sr_3Fe_2O_5Cl_2$ and 3.737(4) Å for $Sr_3Fe_2O_5Br_2$. The expansion in *c* occurs solely as a result of expansion within the strontium halide 'rocksalt' layers, with the halide to halide separation along *z* increasing from 2.15 Å for X = Cl to 2.54 Å for X = Br. The expansion is also reflected in the large increase in the apical Fe-X distance (Table 5.2) in line with the increase in ionic radii.

Introduction of approximately 50 % of Co ions onto the square pyramidal sites within $Sr_3Fe_2O_5Cl_2$ has a significant effect, with the *a* parameter of the mixed Fe/Co material showing a small decrease ~ 0.02 Å and *c* exhibiting a 0.08 Å increase. Completely replacing the iron ions with cobalt produces a further reduction in the *a* parameter by an additional 0.015 Å, and further increase in *c* by an additional 0.014 Å. The reduction in *a* is consistent with the presence of the smaller Co^{3+} ionic radii (high spin r_{eff} = 0.61 Å, low spin r_{eff} = 0.545 Å) compared to Fe^{3+} (high spin r_{eff} = 0.645 Å). In contrast, the increase in the size of the *c* parameter with cobalt substitution does not follow the expected trend and runs contrary to the behaviour observed for the closely related Ruddlesden-Popper $Sr_3Fe_{2-x}Co_xO_{7-\delta}$ series [19] and the $YBa_2(Fe_{1-z}Co_z)_3O_{8+x}$ with $0.0 \leq z \leq 0.5$ series [20]. This elongation of the unit cell occurs principally through the average M-Cl interactions which increase by ~ 0.02 Å for 50 % substitution, and by a further ~ 0.05 Å at full substitution. One possible reason for this expansion could be that a proportion of the Co^{3+} ions are present in the $t_{2g}^5e_g^1$ intermediate spin (IS) state within the oxide halides. This results in a partially filled d z^2 orbital, which as it points along the apical axis causes the lattice parameter *c* to lengthen. Equally because the d x^2-y^2 orbital becomes less filled, the equatorial bonds shorten leading to a reduction in the *a* parameter. A similar explanation has been suggested to account for the analogous highly elongated coordination seen in $TlSr_2CoO_5$ [21]. See below for a diagram depicting spin states for a d^6 ion.

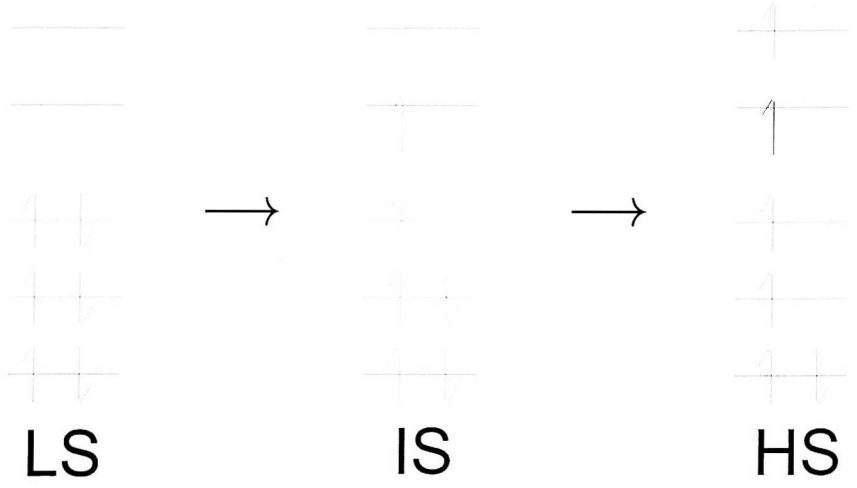

Figure 5.4.2a Representation of the possible spin states for a d^6 ion, low spin (LS), intermediate spin (IS) and high spin (HS)

It is worth noting that the refined fractional occupancy of the metal site of $Sr_3FeCoO_5Cl_2$ indicates a slight cobalt deficiency, suggesting the true stoichiometry of the sample to be $Sr_3Fe_{1.12(2)}Co_{0.88(2)}O_5Cl_2$.

A comparison of the interatomic distances obtained from the room temperature and low temperature data sets (Table 5.2) reveals the expected contraction on cooling for all four materials. The variation in the lattice constants of $Sr_3Fe_2O_5Cl_2$ (Fig. 5.4.2a) over a 600 K temperature range shows a smooth monotonic variation and significantly there is no sign of an anomaly as long range magnetic order is established at $T \leq 600$ K. The percentage changes in the cell parameters are ~ 0.6 % for *a* and 1.0 % for *c* indicating that the thermal expansion within the phase is not appreciably anisotropic; a somewhat surprising result as lamellar materials usually exhibit significantly greater expansion in the direction perpendicular to the tetragonal plane. The temperature dependence of the Fe coordination of $Sr_3Fe_2O_5Cl_2$ is shown in Figure 5.4.2a. The apical Fe-O(1) and Fe-Cl interactions show the expected expansion on heating, as does the in-plane Fe-O(2) distance (see Fig. 5.4.2b). The basal O(2)-Fe-O(2) bond angle demonstrates a small reduction with increasing temperature that corresponds to a reduction in the level of buckling within the plane as a result of increased atomic vibration (as with the behaviour of negative thermal expansion materials). Once more there is no indication of a structural response in any of these parameters coincident with the onset of magnetic order within the phase.

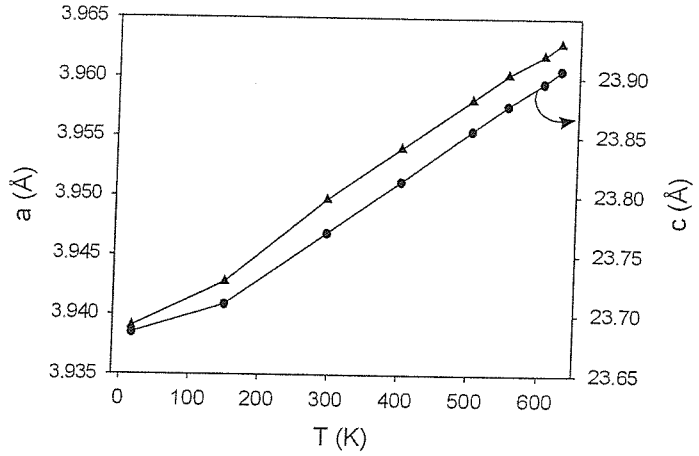

Figure 5.4.2a Graph showing the variation of lattice parameters with temperature in $Sr_3Fe_2O_5Cl_2$

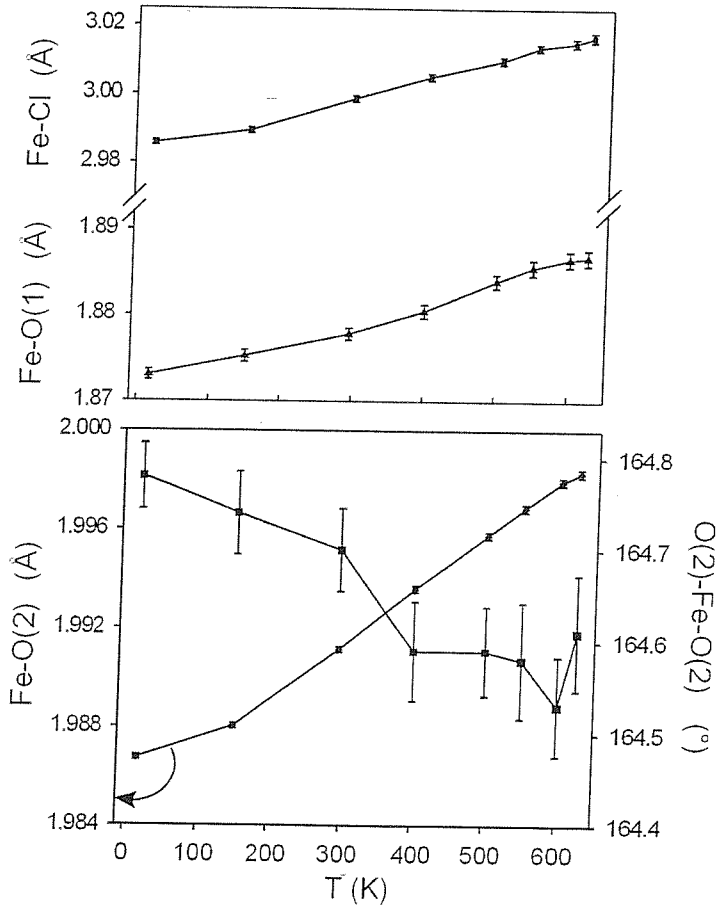

Figure 5.4.2b Graph showing the change in the Fe-O(1) and Fe-Cl bond distances, and the basal Fe-O(2) bond and O(2)-Fe-O(2) bond angle, with temperature in $Sr_3Fe_2O_5Cl_2$

5.4.3 Magnetic structure

The additional magnetic Bragg reflections in the neutron diffraction patterns collected at 295 K and below for $Sr_3Fe_2O_5Cl_2$, $Sr_3Fe_2O_5Br_2$, and $Sr_3FeCoO_5Cl_2$ arise from long range antiferromagnetic order of the transition metal spins and are consistent with Ackerman's Mössbauer spectrum of $Sr_3Fe_2O_5Cl_2$ single crystals, obtained at room temperature [7]. The oxide halides adopt a G-type antiferromagnetic spin structure shown in Figure 5.4.3a with each iron moment aligned anti-parallel to its five nearest neighbours. This type of arrangement is commonly adopted by Ruddlesden-Popper phases, see for example $Sr_3Mn_2O_7$, the Mn^{4+} parent compound of the layered CMR manganites [11]. It is also similar to the magnetic structures adopted by related multi-layer iron perovskites such as $Pb_4Fe_3O_8Cl$ [22] and $YBa_2Fe_3O_{8+x}$ [12] whose structures result from antiferromagnetic interactions through the basal Fe $d^1_{x^2-y^2}$-O$p_{x,y}$- $d^1_{x^2-y^2}$ links and across the apical Fe $d^1_{z^2}$ -O$_{pz}$- $d^1_{z^2}$ bonds as predicted by the Goodenough-Kanamori (GK) superexchange rules [23, 24].

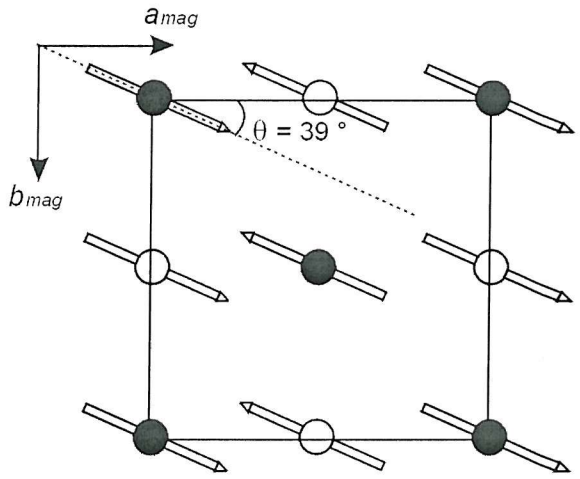

Figure 5.4.3a Alignment of the Fe moment within the xy-plane for $Sr_3Fe_2O_5Cl_2$. Fe spins are shown at the (½,0,z) z ≈ 0.42 positions (white spheres) and on the (0,0,z) and (½,½,z) z ≈ 0.08 sites (dark spheres).

The previous single crystal Mössbauer investigation indicates that the Fe moments lie within the *xy*-plane and our refinements show that the spins do not point along the *a* or *b* axes of the magnetic cell. Instead a level of rotation of the Fe spins within the *xy*-plane is favoured with the easy axis lying at an angle θ close to 40 ° for all three phases (see Fig. 5.4.3b). It is also worth noting that the uniform temperature dependence of the magnetic reflections of $Sr_3Fe_2O_5Cl_2$ shown in Figure 5.4.3b indicates that the spin alignment angle θ remains constant within ± 5° throughout the

measured temperature range, confirming the absence of spin crossover effects within the plane.

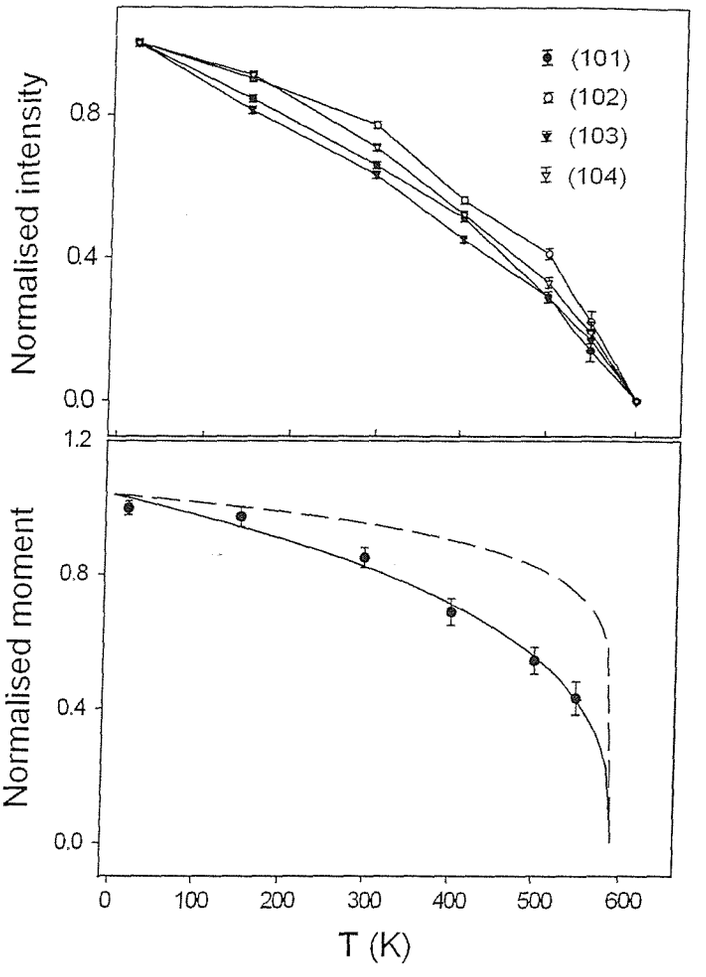

Figure 5.4.3b Graph showing the temperature dependence of the normalised intensity of the main magnetic peaks (upper) and normalised magnetic moment (lower) of $Sr_3Fe_2O_5Cl_2$. In the lower plot, the solid line represents the fit to the power law in Equation 5.4.3a and the broken line corresponds to the expected behaviour for a 2D Ising system.

The magnitudes of the low temperature refined moments of $Sr_3Fe_2O_5Cl_2$ (17 K) and $Sr_3Fe_2O_5Br_2$ (2 K) are 4.40(4) μ_B and 4.07(6) μ_B respectively. These values are both consistent with the presence of high spin Fe(III), with the reduction from the ideal spin only value of 5 μ_B attributed to zero point fluctuations in the layered structures [24]. The lower ordered moment for the bromide phase is compatible with the expected weakening of the exchange interactions as a result of the expanded in-plane Fe-O distances and the increased interlayer separation within the material.

The ordered moment μ = 2.11(4) μ_B obtained for $Sr_3FeCoO_5Cl_2$ at 2 K, compared with 4.4 μ_B for the un-substituted Fe oxide chloride represents a significant reduction in the average moment. We would expect the Co ions to be present in a high spin (HS) state within $Sr_3FeCoO_5Cl_2$ and $Sr_3Co_2O_5Cl_2$, as our recent study on the closely related single layer K_2NiF_4-type cobalt oxide halide Sr_2CoO_3Cl [25] revealed an ordered moment of 2.82(3) μ_B at 2 K indicative of a HS electron configuration. However, the absence of any magnetic ordering in $Sr_3Co_2O_5Cl_2$ and the greater than expected reduction in the ordered moment of $Sr_3FeCoO_5Cl_2$ (assuming HS states for both ions, approx. 50:50 mix of S = 1 ½, Fe^{3+} and S = 2, Co^{3+} would yield a reduction of ~ 20 %) suggests that the Co^{3+} ions are in a low spin state in these materials. A further possible explanation would be that a proportion of the Co^{3+} ions are in an intermediate spin state. This electron arrangement would produce a lower refined moment, as the IS state consist of two unpaired electrons, *i.e.* S = 1 compared with the HS $t_{2g}^4e_g^2$, S = 2. Additionally, the presence of even a small amount of the IS state could diminish the (antiferromagnetic) magnetic moment still further due to the opposing, weakly ferromagnetic, interaction between the occupied d_x^2 - $_y^2$ orbitals of HS Fe^{3+} and HS Co^{3+} and the empty d_x^2 - $_y^2$ orbital of IS Co^{3+}. Nonetheless, the complete absence of any magnetic peaks for the phase $Sr_3Co_2O_5Cl_2$ suggests that the Co^{3+} ions are in fact in a low spin state within these oxide halides.

The thermal dependence of the normalised magnetic moment of $Sr_3Fe_2O_5Cl_2$ is shown fitted to the power law given in Equation 5.4.3a below (see Fig. 5.4.3b (lower)). Also shown is the expected behaviour of a 2D Ising system (*i.e.* critical exponent β = 0.125).

$$\frac{M(T)}{M(0)} = C(1 - T/T_N)^{\beta}$$

Equation 5.4.3a

A good quality fit over the whole temperature rage was obtained with C = 1.04(3), T_N = 590(22) K and a critical exponent β = 0.33(6) characteristic of a 3D transition. The value of β indicates that the growth of long range magnetic order occurs more gradually than the 2D behaviour observed for planar antiferromagnets such as K_2NiF_4 itself [26]. This probably reflects the increased dimensionality of the double layer perovskite block within the material when compared to the single layer, n = 1 members of the Ruddlesden-Popper series. The fitted $T_{Néel}$ of 590 K, is in good

agreement with our observation of the complete disappearance of magnetic intensity which occurred on heating the sample between 550 K and 600 K. The T_N is similar to those typically reported for related Fe perovskites [12, 22] and we would expect a lower ordering temperature for $Sr_3Fe_2O_5Br_2$ given the expanded Fe to Fe distances (particularly the interlayer separations) within the phase.

5.5 Conclusions

Powder neutron diffraction has been used to characterise the crystal structure of four Ruddlesden–Popper related oxide halide materials ($Sr_3Fe_2O_5Cl_2$, $Sr_3Fe_2O_5Br_2$, $Sr_3Co_2O_5Cl_2$ and $Sr_3FeCoO_5Cl_2$), and the magnetic structure of three of these phases (those containing iron).

Structurally the expansion induced by the replacement of the chloride ion by the larger bromide ion occurs solely in the 'rocksalt' SrX_2 layers whilst cobalt substitution produces a reduction in overall cell volume but an unexpected increase in the *c* parameter.

The compounds $Sr_3Fe_2O_5Cl_2$, $Sr_3Fe_2O_5Br_2$, and $Sr_3FeCoO_5Cl_2$ adopt an antiferromagnetic spin arrangement with an expanded $\sqrt{2}a_{nuc}$ by $\sqrt{2}a_{nuc}$ by *c* magnetic cell with magnetic moments that lie off-axis within the *xy*-plane. $Sr_3Co_2O_5Cl_2$ does not order magnetically.

5.6 References

1 McGlothlin N, Ho D, Cava R J, *Mater. Res. Bull.*, 2000, **35**, 1035

2 Knee C S, Weller M T, *J. Solid State Chem.*, 2002, **168**, 1

3 Knee C S, Weller M T, *Chem. Commun.*, 2002, 256

4 Kodenkandath T A, Lalena J N, Zhou W L L, Carpenter E E, Sangregorio C, Falster A U, Simmons W B, O'Connor C J, Wiley J B, *J. Am. Chem. Soc.*, 1999, **121**, 10743

5 Viciu L, Caruntu G, Royant N, Koenig J, Zhou W L L, Kodenkandath T A, Wiley J B, *Inorg. Chem.*, 2002, **21**, 3385

6 Leib W, Müller-Buschbaum Hk, *Z. Anorg. Allg. Chem.*, 1984, **518**, 115

7 Ackerman J F, *J. Solid State Chem.*, 1991, **92**, 496

8 Loureiro S M, Felser C, Huang Q, Cava R J, *Chem. Mater.*, 2000, **12**, 3181

9 Hector A L, Hutchings J A, Needs R L, Thomas M F, Weller M T, *J. Mater. Chem.*, 2001, **2**, 527

10 Parthé E, Hu S, *J. Solid State Chem.*, 2003, **174**, 165

11 Hirota K, Morimoto Y, Fujioka H, Kubota M, Yoshizawa M, Endoh Y, *J. Phys. Soc. Jpn.*, 1998, **67**, 3380

12 Mitchell J F, Millburn J E, Medarde M, Short S, Jorgensen J D, Fernandez-Diaz M T, *J. Solid State Chem.*, 1998, **141**, 599

13 Huang Q, Karen P, Karen V L, Kjekshus A, Lynn J W, Mighell A D, Rosov N, Santoro A, *Phys. Rev. B*, 1992, **45**, 9611

14 Grenier J C, Ghodbane S, Demazeau G, Pouchard M, Hagenmuller P, *Mat. Res. Bull.*, 1979, **14**, 831

15 Grenier J C, Ghodbane S, Demazeau G, Pouchard M, Hagenmuller P, *Mat. Res. Bull.*, 1979, **14**, 831

16 Larson A C, von Dreele R B, Generalised Structure Analysis System, Los Alamos National Laboratory, 1994

17 Brown P J, in International Tables for Crystallography (T. Hahn, Ed.) Vol. C, Kluwer Academic Publishers, Dordrecht, 1992

18 Shannon R D, *Acta Crystallogr. Sect. A*, 1976, **32** 751

19 Veith G M, Chen R, Popov G, Croft M, Shokh Y, Nowik I, Greenblatt M, *J. Solid State Chem.*, 2002, **166**, 292

20 Huang Q Z, Karen V L, Santoro A, Kjekshus A, Lindén J, Pietari T, Karen P, *J. Solid State Chem.*, 2003, **172**, 73

21 Doumerc J P, Coutanceau M, Demourgues A, Elkaim E, Grenier J C, Pouchard M, *J. Mater. Chem.*, 2001, **11**, 78

22 Knee C S, Weller M T, *J. Mater. Chem.*, 2001, **11**, 2350

23 Goodenough J B, *J. Phys. Chem. Solids.*, 1958, **6** 287

24 Li R K, Gu L N, Greaves C, *Phys. Rev. B*, 2002, **65** Art. No. 104439

25 Knee C S, Price D J, Lees M R, Weller M T, *Phys. Rev. B*, 2003, **68** Art. No. 174407

26 Birgeneau R J, Guggenheim H J, Shirane G, *Phys. Rev. B*, 1970, **1**, 2211

Chapter Six

Synthesis and Structural Characterisation of $NdSrZnO_{4-x}(CO_3)_y$

6.1 Introduction

The structural chemistry of zinc is dominated by octahedral and tetrahedral coordination environments, other four-coordinate zinc structures are also known, whilst five-coordinate zinc is rarely recorded in the literature.

The single crystal structures of phosphates and arsenates containing octahedrally coordinated zinc have been quite widely reported [1, 2], however there are only a few examples of zinc in this coordination environment within oxide chemistry. $(Sr_3La)(ZnRu)O_8$ [3] and $BaLaZnRuO_6$ [4] are two examples of zinc in different octahedral coordination environments. $(Sr_3La)(ZnRu)O_8$ [3] possesses distorted octahedra, with longer apical zinc-oxygen bonds than the equatorial zinc-oxygen bonds, whilst the zinc-oxygen octahedra $BaLaZnRuO_6$ [4] are regular in shape.

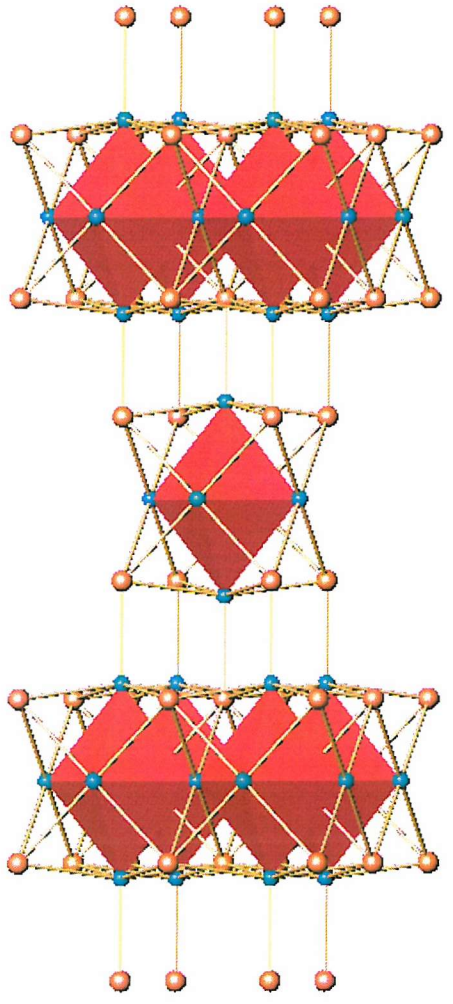

Figure 6.1a Representation of the Structure of $NdSrZnO_{4-x}$ with ZnO_6 octahedra

The structure of $NdSrZnO_{4-x}$ has been reported previously by Grandjean [5], and its orthorhombic to tetragonal distortion already noted (when in its tetragonal form it adopts the K_2NiF_4 structure). This structural transition appears to be peculiar to zinc, for the related $NdSrCo_{1-y}Cu_yO_{4-x}$ structure is tetragonal for values of y from 0 to 0.9 [6]. Therefore, it was thought that a more in-depth study of the unusual structural transition of $NdSrZnO_{4-x}$ was warranted, to attempt to gain an understanding as to how it occurred.

Different lanthanide analogues (as seen in Chapter three), solid solutions and oxide halide analogues (both seen in Chapter four) were also thought to be of potential interest and appropriate syntheses duly attempted.

6.2 Experimental Procedure

Initial work within this area was based on trying to synthesise a series of lanthanide analogues of the known phase $NdSrZnO_{4-x}$ (x = 0.5) [5], using samarium, gadolinium, dysprosium, cerium and praseodymium. Samples were prepared by intimately grinding together high purity stoichiometric mixtures of Nd_2O_3 / Sm_2O_3 / Gd_2O_3 / Dy_2O_3 / Pr_6O_{11} / CeO_2, $SrCO_3$ and ZnO (all 99.9% or better) and heating the reactants to 1025 °C for 60 hours, regrinding the intermediates and heating again to 1100 °C for a further 60 hours (for results, see Table 6.3.1a).

Synthetic work then concentrated on making good quality samples of both the orthorhombic and tetragonal forms of $NdSrZnO_{4-x}$ for study by powder neutron diffraction. The optimised method involved heating the reactants to 1025 °C for 24 hours to produce the orthorhombic phase, this product could then be pelletised and heated at 1100 °C for 24 hours to form the tetragonal phase (for results, see Table 6.3.1b). This optimised synthetic method was used to try and explore other structural variations by attempting to synthesise the solid solution $Nd_{2-x}Sr_xZnO_{3.5}$ (x = 0.5, 1.5) (for results, see Table 6.3.1c).

Synthetic attempts were then made towards a final variation upon the $NdSrZnO_{4-x}$ phase, $NdSrZnO_3Cl$, using lower reaction temperatures due to the

volatility of chloride. This low temperature approach involved heating Nd_2O_3, $SrCO_3$, $SrCl_2$ and ZnO at 800 °C for 24 hours, regrinding, pelletising and heating again at 950 °C, then regrinding, pelletising and heating one final time at 1050 °C (for results, see Table 6.3.1d).

To determine whether the use of a carbonate starting material affected the final product, formed the optimised $NdSrZnO_{4-x}$ synthetic method was employed, but with SrO taking the place of $SrCO_3$ as a reactant (for results, see Table 6.3.1e).

In order to clarify whether the orthorhombic and tetragonal phases formed during synthesis were stable to further heating, thermal analysis data for the tetragonal and orthorhombic samples analysed by powder neutron diffraction were collected on a Polymer Laboratories STA 1500 in flowing air at temperatures up to 1150 °C (for results, see Table 6.3.1f).

Infrared spectroscopy was carried out using a Perkin Elmer Spectrum One system. Data were collected using an average of five scans over the range 400 to 4000 cm^{-1}, at high resolution.

All of the syntheses and analyses were monitored by PXD using a Siemens D5000 diffractometer operating with Cu $K_{\alpha 1}$ radiation, over the data range of 10 – 110° 2θ. The phases identified within the PXD patterns collected are listed in the results section.

Powder neutron diffraction data were collected for 1g samples, of the orthorhombic and tetragonal forms of $NdSrZnO_{4-x}$, on the GEM detector array at Rutherford Appleton Laboratories at 298K. Data collection times were 3 hours and data reduction was carried out using the standard methods; data banks two, three and four were included in the structure refinement, which employed the GSAS package [7].

6.3 Results, including Structural Refinement

6.3.1 Synthetic Results

Except in the case of the known phase $NdSrZnO_{4-x}$, it proved impossible to form the desired target phases with $SrLn_2O_4$ forming as the primary alternative product instead:

Target Phase	Reagents	Heat Treatment	Products
$LnSrZnO_{4-x}$	Nd_2O_3, $SrCO_3$ and ZnO	1025 °C, 60h	100% (orthorhombic) $NdSrZnO_{4-x}$
		1100 °C, 60h	100% (tetragonal) $NdSrZnO_{4-x}$
	Sm_2O_3, $SrCO_3$ and ZnO	1025 °C, 60h	60% $SrSm_2O_4$, 20% $SrZnO_2$ and 20% ZnO
		1100 °C, 60h	45% $SrSm_2O_4$, 35% $SrZnO_2$ and 20% ZnO
	Gd_2O_3, $SrCO_3$ and ZnO	1025 °C, 60h	50% $SrGd_2O_4$, 25% $SrGd_4O_7$, 15% ZnO and 10% $GdZn_{12}$
		1100 °C, 60h	35% $SrGd_2O_4$, 25% $SrGd_4O_7$, 25% ZnO and 15% $SrZnO_2$
	Dy_2O_3, $SrCO_3$ and ZnO	1025 °C, 60h	55% $SrDy_2O_4$, 35% $SrZnO_2$ and 10% ZnO
		1100 °C, 60h	as above
	Pr_6O_{11}, $SrCO_3$ and ZnO	1025 °C, 60h	55% $SrPrO_3$, 30% Zn and 15% ZnO
		1100 °C, 60h	as above
	CeO_2, $SrCO_3$ and ZnO	1025 °C, 60h	60% $Sr(CeO_3)$, 20% ZnO, 15% CeO_2 and 5% $SrZnO_2$
		1100 °C, 60h	85% $Sr(CeO_3)$, 10% ZnO and 5% CeO_2

Table 6.3.1a Varied lanthanide analogues of $NdSrZnO_{4-x}$

The optimised method readily produced pure samples of both the orthorhombic and tetragonal phases:

Target Phase	Reagents	Heat Treatment	Products
$NdSrZnO_{4-x}$	Nd_2O_3, $SrCO_3$ and ZnO	1025 °C, 24h	100% (orthorhombic) $NdSrZnO_{4-x}$
		pelletised then 1100 °C, 24h	100% (tetragonal) $NdSrZnO_{4-x}$

Table 6.3.1b Optimised synthesis of $NdSrZnO_{4-x}$.

Unfortunately the target phases did not form when the Nd:Sr ratio was varied from 1:1; instead only a small proportion of $NdSrZnO_{4-x}$ was produced alongside simple by-products:

Target Phase	Reagents	Heat Treatment	Products
$Nd_{1.5}Sr_{0.5}ZnO_{4-x}$	Nd_2O_3, $SrCO_3$ and ZnO	1025 °C, 24h	65% (orthorhombic) $NdSrZnO_{4-x}$, 20% Nd_2O_3 and 15% ZnO.
		pelletised then 1100 °C, 24h	55% (tetragonal) $NdSrZnO_{4-x}$, 15% Nd_2O_3, 15% ZnO and 15% unknown impurity.
$Nd_{0.5}Sr_{1.5}ZnO_{4-x}$		1025 °C, 24h	60% (orthorhombic) $NdSrZnO_{4-x}$, 20% $SrZnO_2$, 10% Nd_2O_3 and 10% SrO.
		pelletised then 1100 °C, 24h	35% ZnO, 25% Nd_2O_3, 15% (tetragonal) $NdSrZnO_{4-x}$, 15% ZnO_2, and 10% SrO.

Table 6.3.1c Varied stoichiometric analogues of $NdSrZnO_{4-x}$.

In the case of $NdSrZnO_3Cl$, once again the desired analogue did not form, Sr_4OCl_6 and simple oxides formed instead:

Target Phase	Reagents	Heat Treatment	Products
$NdSrZnO_3Cl$	Nd_2O_3, $SrCO_3$, $SrCl_2$and ZnO	800 °C, 24h	60% Nd_2O_3, 20% ZnO and 20% Sr_4OCl_6
		Pelletised, then 24h at 950 °C	50% Nd_2O_3, 25% ZnO, 15% Sr_4OCl_6 and 10% NdO
		Pelletised, then 24h at 1050 °C	45% ZnO, 35% Nd_2O_3, 15% Sr_4OCl_6 and 5% NdO

Table 6.3.1d Oxide chloride analogue of $NdSrZnO_{4-x}$

It was thought that the use of a carbonate starting material might be affecting the final phases formed and thus an oxide only method was tried in an attempt to judge if the phases formed were any different.

The carbonate-free optimised method successfully synthesised pure samples of the orthorhombic phase but did not lead to formation of the tetragonal phase, even after repeated thermal treatments. Higher reaction temperatures were tried as a means to encourage the tetragonal phase to form, but although some tetragonal phase formed, significant phase degradation, to a mixture of simple oxides, also occurred:

Target Phase	Reagents	Heat Treatment	Products
$NdSrZnO_{4-x}$	Nd_2O_3, SrO and ZnO	1025 °C, 24h	100% (orthorhombic) $NdSrZnO_{4-x}$
		Pelletised, then 24h at 1100 °C	100% (orthorhombic) $NdSrZnO_{4-x}$
		Pelletised, then 24h at 1200 °C	50% (tetragonal) $NdSrZnO_{4-x}$, 25% NdO_2, 15% ZnO and 10% $SrZnO_2$

Table 6.3.1e Carbonate-free synthesis of $NdSrZnO_{4-x}$

Thermal analysis showed that the orthorhombic phase degraded slightly with heating, whilst the tetragonal phase did not alter at all:

Original Phase	TGA/DTA Conditions	Colour	Products
Orthorhombic $NdSrZnO_{4-x}$	Up to 1150 °C in flowing air	Pale green	95% (orthorhombic) $NdSrZnO_{4-x}$ and 5% Nd_2O_3
Tetragonal $NdSrZnO_{4-x}$		Dirty green	100% (tetragonal) $NdSrZnO_{4-x}$

Table 6.3.1f TGA/DTA of orthorhombic and tetragonal $NdSrZnO_{4-x}$ in flowing air

PXD data was used to confirm the purity of the phases formed, however full structural refinements of the orthorhombic and tetragonal phases were attempted using the PND data.

6.3.2 Structural Investigation

The models used as the basis for the structural refinements were those given by Grandjean [5] Initially the orthorhombic data set was analysed using a unit cell approx. 3.76 x 3.72 x 13.29 Å in space group I/m m m. A similar methodology was subsequently employed for the data collected for the tetragonal phase using a unit cell approx. 3.73 x 13.31 Å in space group I 4/m m m. This model could account for the majority of the reflections in the diffraction profile of the phases, but significant other peaks were still present (discussed later in this section).

Initially the refinements proceeded readily with incorporation of background, zero-point and lattice parameters, but once peak shape was allowed to vary the refinements became quite unstable. Careful handling of the refinements using damping coefficients allowed atomic positions, atomic displacement parameters and site occupancies to be varied, but the peak shape coefficients remained large.

Refined atomic co-ordinates, lattice parameters and profile fit factors for the orthorhombic and tetragonal phases are summarised in Tables 6.1 and 6.2 respectively, whilst the derived bond lengths and angles for these phases are in Table 6.3 and 6.4. Figures 6.3.2a and 6.3.2b show profile fits as obtained to orthorhombic and tetragonal $NdSrZnO_{4-x}$.

Table 6.1 Refined atomic co-ordinates, lattice parameters and profile fit factors for orthorhombic $NdSrZnO_{4-x}$. Space group I/mmm Nd/Sr on $(0,0,z_{Nd/Sr})$ site, Zn on (0,0,0), O(1) on $(0,0,z_O)$, O(2) on (0,½,0) and O(3) on (½,0,0). Thermal displacement parameters (all x 100, $Å^2$) for each atom sites are also given, values for Nd and Sr were constrained to be equal, esd's are given in parentheses.

Compound	Orthorhombic $NdSrZnO_{4-x}$
$z_{Nd/Sr}$	0.35473(13)
U_{iso} Nd/Sr	1.53(6)
U_{iso} Zn	1.13(9)
z_O	0.17191(25)
U_{iso} O(1)	3.72(9)
$n_{O(2)}$	0.388(9)
U_{iso} O(2)	0.79(12)
$n_{O(3)}$	0.694(23)
U_{iso} O(3)	6.02(36)
x	0.530(16)
a / Å	3.76029(10)
b / Å	3.72166(10)
c / Å	13.2939(5)
R_p	4.33
R_{wp}	5.02
χ^2	9.923

Table 6.2 Refined atomic co-ordinates, lattice parameters and profile fit factors for tetragonal $NdSrZnO_{4-x}$. Space group I 4/mmm Nd/Sr on $(0,0,z_{Nd/Sr})$ site, Zn on (0,0,0), O(1) on $(0,0,z_{O(2)})$ and O(2) on $(x_{O(2)},½,0)$. Thermal displacement parameters (all x 100, $Å^2$) for each atom sites are also given, values for Nd and Sr were constrained to be equal, esd's are given in parentheses.

Compound	Tetragonal $NdSrZnO_{4-x}$
$z_{Nd/Sr}$	0.35368(8)
U_{iso} Nd/Sr	1.502(26)
U_{iso} Zn	1.97(5)
z_O	0.17266(15)
U_{iso} O(1)	3.54(4)
$x_{O(2)}$	0.0979(6)
$n_{O(2)}$	0.371(3)
U_{iso} O(2)	2.13(8)
x	0.516(2)
a / Å	3.73087(4)
c / Å	13.31506(26)
R_p	4.14
R_{wp}	4.44
χ^2	4.686

Table 6.3. Derived bond lengths (Å) of note for orthorhombic $NdSrZnO_{4-x}$

Compound Bond	Orthorhombic $NdSrZnO_{4-x}$
Nd/Sr – O(1) x 1	2.430(4)
Nd/Sr – O(1) x 4	2.6689(4)
Nd/Sr – O(2) x 2	2.4479(13)
Nd/Sr – O(3) x 2	2.6819(12)
Zn – O(1) x 2	2.2853(33)
Zn – O(2) x 2*	1.89845(5)
Zn – O(3) x 2*	1.88014(5)

* Indicates partially occupied site

Table 6.4. Derived bond lengths (Å) of note for tetragonal $NdSrZnO_{4-x}$

Compound Bond	Tetragonal $NdSrZnO_{4-x}$
Nd/Sr – O(1) x 1	2.4123(29)
Nd/Sr – O(1) x 4	2.66104(29)
Nd/Sr – O(2) x 4	2.4584(16)
Zn – O(1) x 2	2.2971(22)
Zn – O(2) x 4*	1.9008(4)

* Indicates partially occupied site

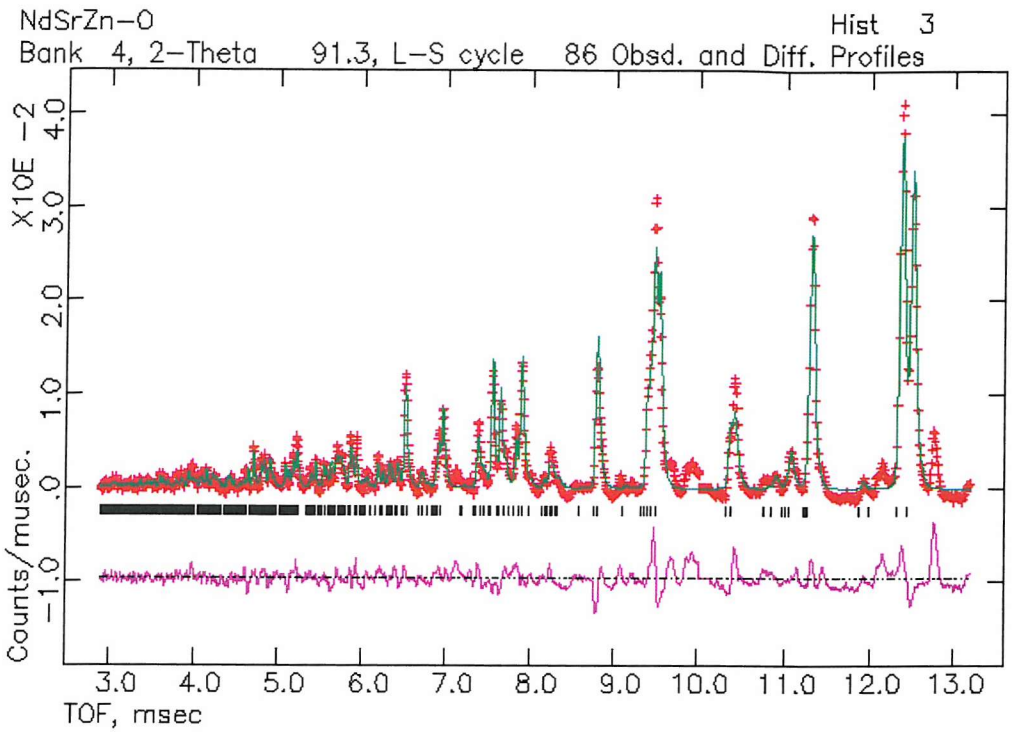

Figure 6.3.2a Profile fit as obtained to orthorhombic $NdSrZnO_{4-x}$ data

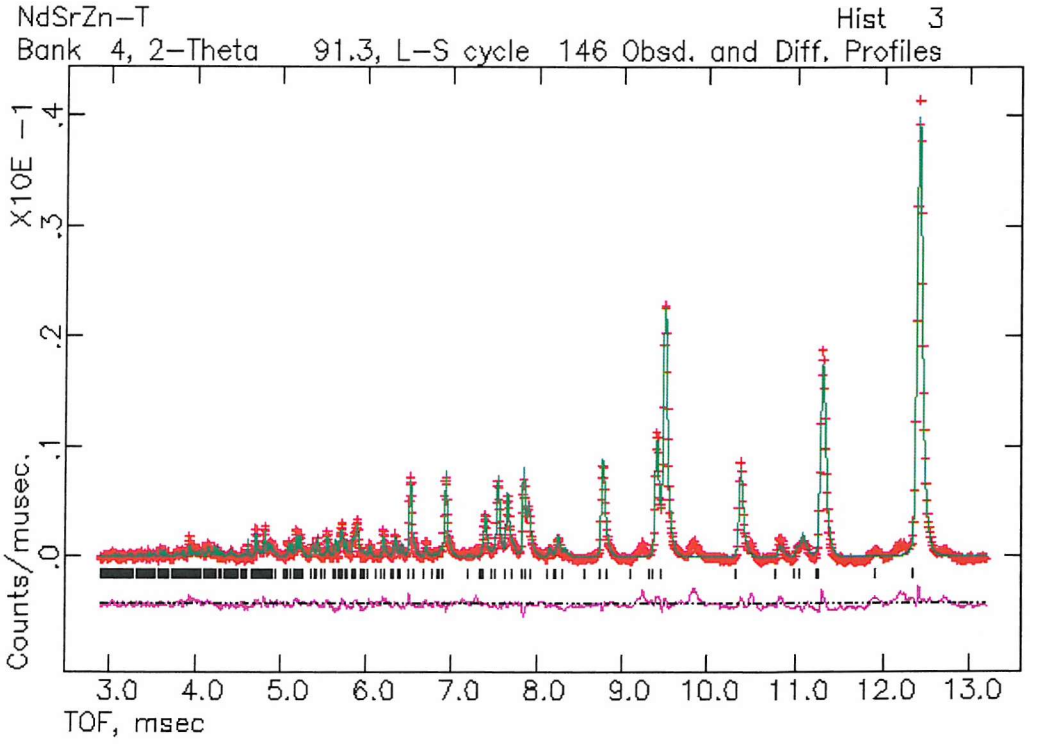

Figure 6.3.2b Profile fit as obtained to tetragonal $NdSrZnO_{4-x}$ data

Several unidentified peaks were present in the profiles that had not been noticeable in the PXD refinements, thus it was thought that secondary phases must be present in the samples.

Various combinations of probable by-products and/or unreacted starting materials, including $SrCO_3$, $SrZnO_2$ and Nd_2O_3, were tried in an effort to model the additional peaks, but none was successful. Often the peaks resulting from incorporation of the additional phase/s were in slightly the wrong position, and/or consistently of the wrong intensity, to model the peaks successfully (see Fig. 6.3.2c). No combination of possible impurities could be found that would satisfactorily model all the additional peaks seen, and thus it was concluded that impurities were not what were causing the additional peaks to occur.

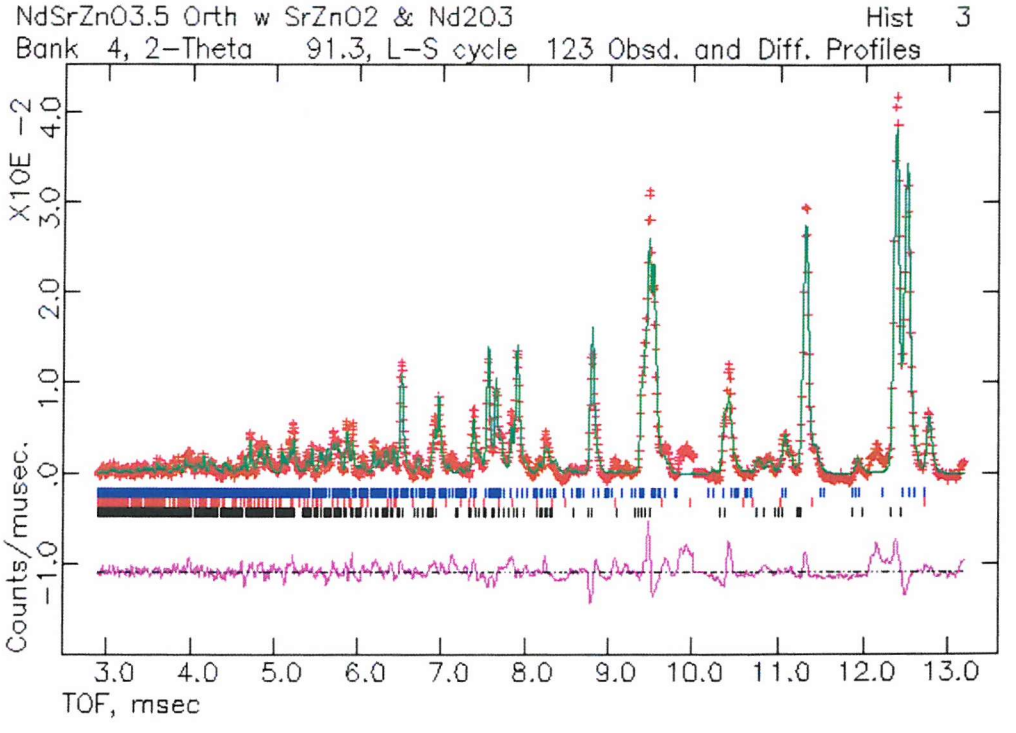

Figure 6.3.2c Profile fit as obtained to orthorhombic $NdSrZnO_{4-x}$ data, including $SrZnO_2$ (blue markers) and Nd_2O_3 (red markers) as impurities

At this point in the refinement process thermal analysis was carried out on the two phases and a significant weight loss at approx. 850 °C was noted in both phases. This temperature is characteristic to the loss of carbonate from materials and led to the question whether, although the synthesis of the samples had

exceeded the temperature at which such a structural group should have exited the sample, carbonate had been incorporated into the phases.

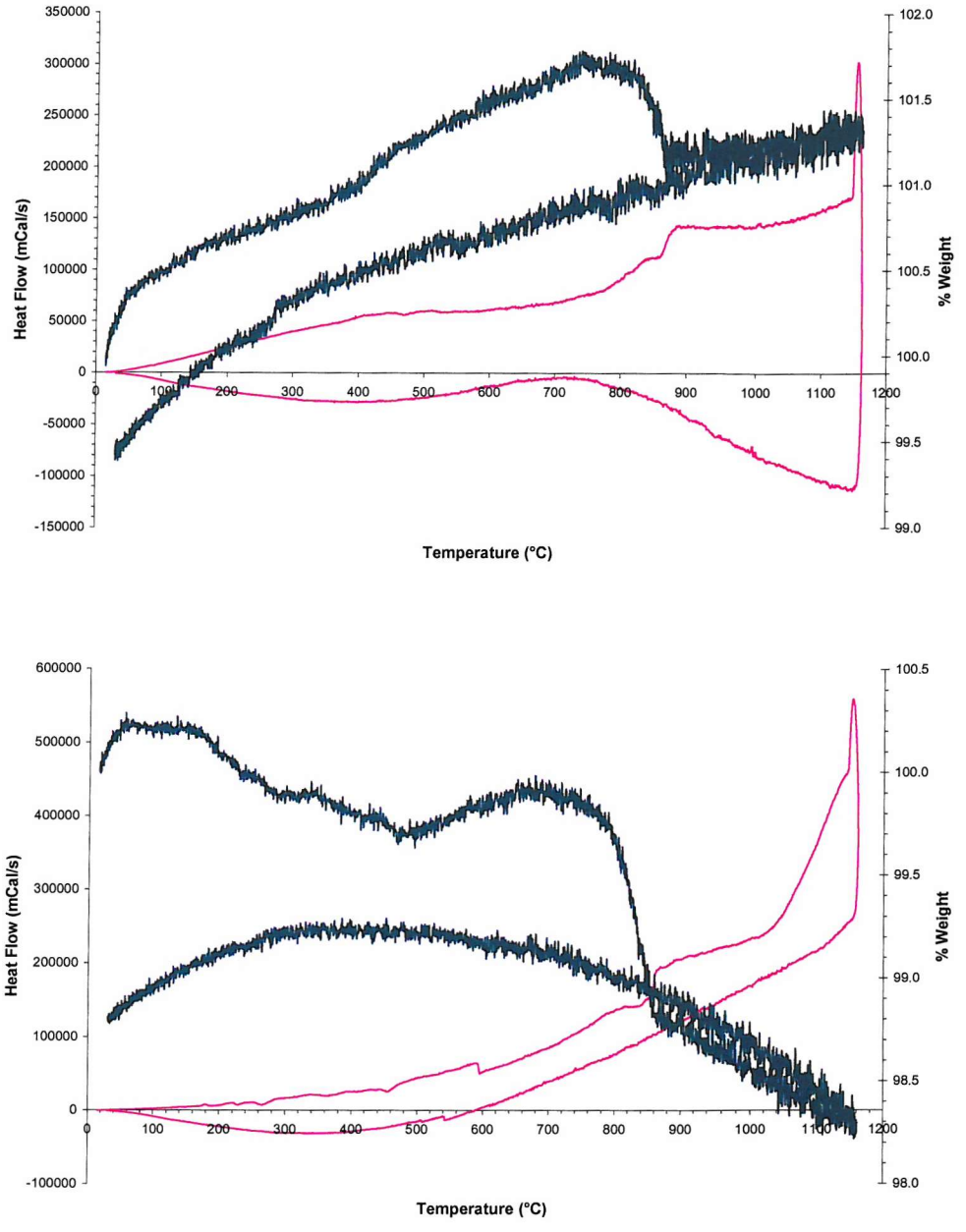

Figure 6.3.2d TGA (dark blue) and DTA (pink) data for orthorhombic $NdSrZnO_{4-x}$ (upper) and tetragonal $NdSrZnO_{4-x}$ (lower) phases heated to 1150 °C in flowing air

Infrared spectroscopy was used to determine whether carbonate was present as carbonate groups result in a characteristic, and easy to recognise, absorption of infrared radiation at approx. 1450 cm^{-1} [8] resulting from a stretch of the C-O bond. When the scans for the two phases were compared to the scan

for a very similar structure, $Nd_{1.8}Ce_{0.2}CuO_4$, (that had also been made from carbonates) significant absorption of radiation in the relevant region could be seen (see Fig. 6.3.2e).

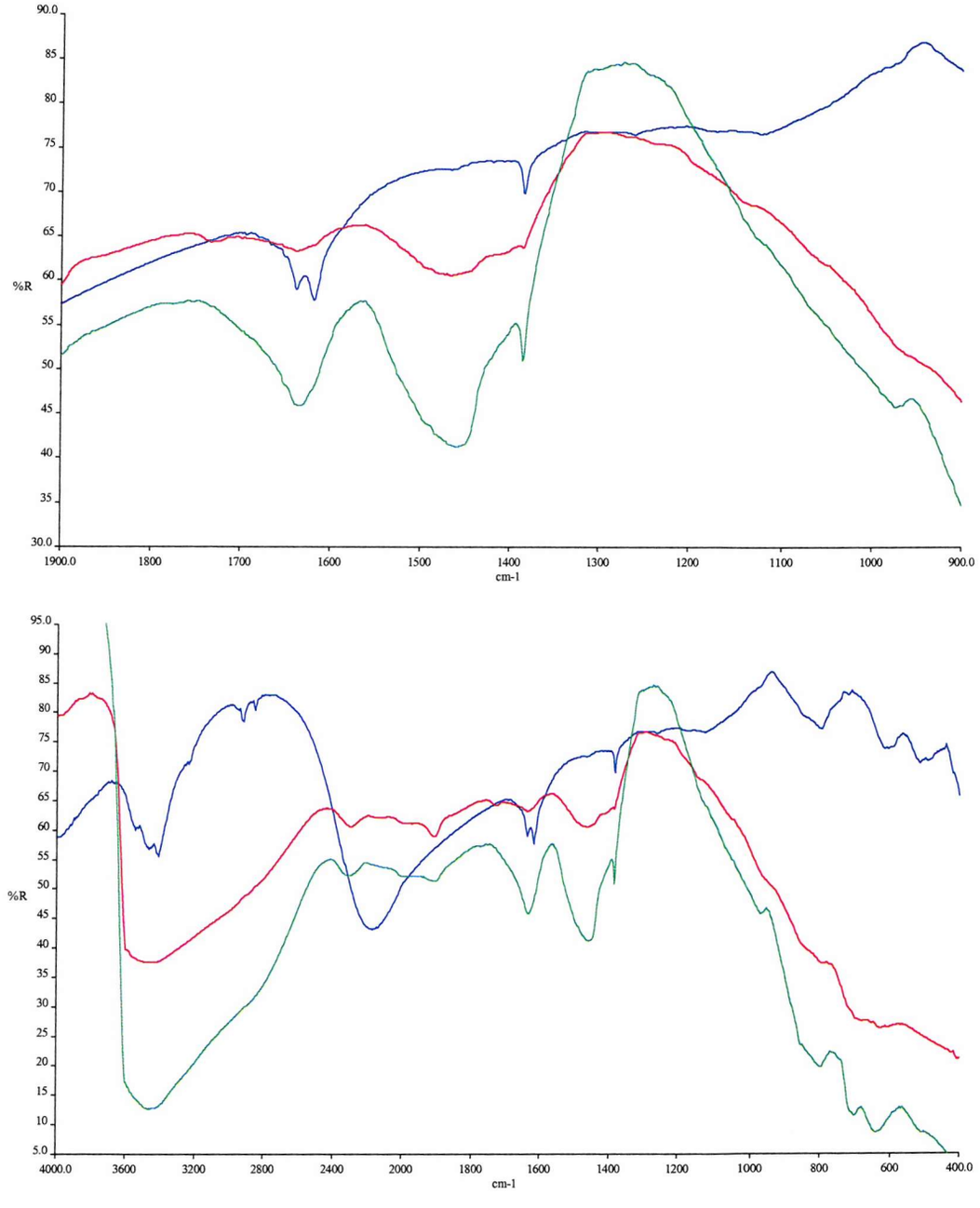

Figure 6.3.2e Comparative Infrared spectra of orthorhombic $NdSrZnO_{4-x}$ (red), tetragonal $NdSrZnO_{4-x}$ (green) and $Nd_{1.8}Ce_{0.2}CuO_4$ (Blue), over the full 400 – 4000 cm^{-1} range (upper) and shorter 1000 – 1900 cm^{-1} range (lower).

This confirmed that carbonate was present in the samples and that the phases should be represented by the more accurate stoichiometric formula $NdSrZnO_{4-x}(CO_3)_y$.

The confirmation of the presence of carbonate meant that TGA data was used to try and calculate the proportion of carbonate in the samples. This was done by determining the weight loss that occurred during the course of the thermal analysis, and attributing this to the loss of carbonate.

$$NdSrZnO_{4-x}(CO_3)_y \rightarrow NdSrZnO_{4-x} + yCO_2$$

With such small weight losses such calculations were bound to include a large degree of e7rror, but tolerably similar values were determined for both the samples. Orthorhombic $NdSrZnO_{4-x}(CO_3)_y$ led to y = 0.04, whilst the tetragonal equivalent led to y = 0.09 (see calculations below).

Assumptions: Mr $NdSrZnO_{4-x}$ (x = 0.5) = 353.2
Mr CO_2 = 44
sample at 750 °C is $NdSrZnO_{3.5}$
sample at 870 °C is $NdSrZnO_{3.5}(CO_3)_y$

Orthorhombic sample calculation:

$$\frac{w_i}{w_f} = \frac{Mr_i}{Mr_f}$$

$$\frac{12.007}{11.948} = \frac{353.2 + 44y}{353.2}$$

$$y = 0.04$$

Tetragonal sample calculation:

$$\frac{17.441}{17.249} = \frac{353.2 + 44y}{353.2}$$

$$y = 0.09$$

Although the amount of carbonate present was certainly very small, nonetheless it had a significant effect upon the refinement causing it to be unstable and resulting in additional peaks. However the small quantity of carbonate was difficult to include within the refinements, especially as carbonate groups are particularly hard to model. This is because although the position of the carbon can usually be fixed, the oxygens often rotate, creating disorder within the sample structure. This problem is not too significant with X-ray data when the light oxygen atoms diffract quite weakly, however in the case of neutron

diffraction oxygen atoms diffract significantly. When using neutron data to examine the change in position of the oxygen atoms associated with the change from orthorhombic to tetragonal forms of the structure this inherent difficulty with the structural model was unavoidable.

The crystal structure of a similar material incorporating carbonate, $Ba_4In_2(CO_3)O_6$ [9], (see Fig. 6.3.2a) was found within the literature and structural models based upon this phase were used to attempt the refinement of both the orthorhombic and tetragonal forms of $NdSrZnO_{4-x}(CO_3)_y$.

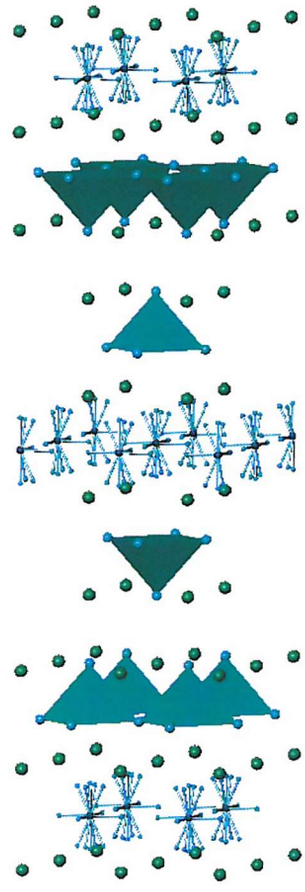

Figure 6.3.2f Representation of the Structure of $Ba_4In_2(CO_3)O_6$, with InO_5 square-based pyramids (the oxygen sites associated with the carbon atoms are partially occupied)

By incorporating carbonate within the refinement, peaks were produced in the diffraction plot in positions that accounted for the previously unmodelled

peaks (see Fig. 6.3.2g), suggesting that Baszczuk's model was correct. However, with such a small proportion of the carbonate atoms present it became almost impossible to refine any of the variables beyond the minimal background, lattice and zero point characteristics, whenever peak shape or atomic variables were altered the refinement became unstable.

Beyond an indication of the suitability of the model used no more detail could be extracted from the refinement as the proportion of carbonate present was too small to be refineable. As a result no refined atomic co-ordinates, or derived bond lengths are presented here for $NdSrZnO_{4-x}(CO_3)_y$,

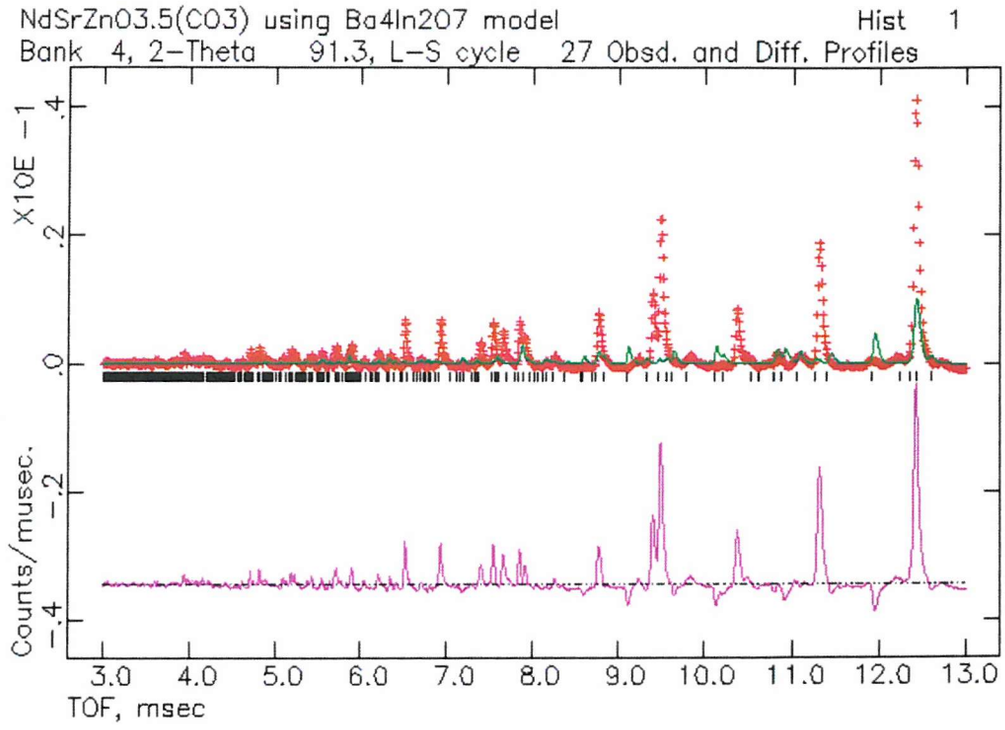

Figure 6.3.2g Profile fit as obtained to tetragonal $NdSrZnO_{4-x}$ data, using Baszczuk's model to incorporate carbonate as $NdSrZnO_{4-x}(CO_3)_y$

Table 6.5 Unrefined atomic co-ordinates, refined lattice parameters (esd's are given in parentheses) and profile fit factors for $NdSrZnO_{4-x}(CO_3)_y$

Atom	x	y	z	Fractional occupancy
Nd	0	0	0.353	0.5
Sr	0	0	0.353	0.5
Zn	0	0	0	1
O	0	0.5	0.1269	1
O	0	0	0.4513	1
C	0	0	0.1269	0.1
O	0.281	0	0.1269	0.025
O	0.116	0	0.1455	0.0125
O	0	0	0.1469	0.05

Space group = I4/mmm, a = 3.7257(9), c = 26.376(10)

R_p = 12.96, R_{wp} = 18.35, χ^2 = 163.9

6.4 Discussion

Samples of the orthorhombic and tetragonal forms of $NdSrZnO_{4-x}(CO_3)_y$ (x = 0.530, y = 0.04and x = 0.516, y = 0.09 respectively) have been successfully synthesised by solid state reactions between metal oxides and metal carbonate. The tetragonal phase adopts a K_2NiF_4 structure, whilst a slight disorder in oxygen positions results in the orthorhombic phase, which remains closely related to the K_2NiF_4 structure type.

The structure of this compound may not be as simple as that of K_2NiF_4, as although zinc would be in full octahedral coordination if the stoichiometry of the structure were $NdSrZnO_{4-x}$, x = 0, it has been shown that x 0.5 for both of the samples studied. The presence of approximately 50 % vacancies on the equatorial oxygen site of the Nd/SrO_6 octahedra means that zinc is in fact in an average coordination state of five. However, it seems unlikely that zinc would be in its least favourable coordination environment, especially when the structural data appears to confirm the presence of zinc octahedra. Overall this would suggest that approximately half the zinc present is indeed six-coordinate, whilst the other half is four-coordinate. This could take the form of alternating

octahedra and distorted tetrahedra; generated by removing two equatorial oxygens from the octahedra.

It would appear that the $NdSrZnO_{4-x}$ structure is only stable for a narrow range of lanthanide ionic radii as even a small difference in near neighbour ionic radii (r (Nd^{3+}) = 1.163 Å, r (Sm^{3+}) = 1.132 Å) could not be tolerated within the structure, with $SrLn_2O_4$ forming instead of the target phase for every lanthanide analogue tried. This may suggest that the structure requires an ionic radius average of 1.33 Å on the neodymium/strontium site.

As mentioned above the neodymium and strontium ions share the same site within the $NdSrZnO_{4-x}$ structure, and no discernible ordering of the two ions is detectable by either PXD or PND analysis. Thus it seemed logical that solid solutions of the parent compound could be made with varying amounts of either of the two ions. Attempts to make the compounds $Nd_{1-x}Sr_xZnO_{4-x}$ (x = 0.5, 1.5) proved unsuccessful, which could be considered as further demonstrating the strict ionic radius restrictions needed to create a stable K_2NiF_4 structure from these ions (see previous paragraph). Alternatively, the lack of target phase formation may be due to the change in oxygen content associated with the change in neodymium to strontium ratio ($Nd_{1.5}Sr_{0.5}ZnO_{3.75}$, $Nd_{0.5}Sr_{1.5}ZnO_{3.25}$) being too great to allow for stable phase formation.

The K_2NiF_4 structure has been shown to incorporate halide ions in place of oxygen and thus it was thought that it should be possible to synthesise a chloride analogue of $NdSrZnO_{4-x}$ in the form $NdSrZnO_3Cl$. This phase was expected to be particularly favoured as the presence of Cl^- in place of O^{2-} would balance the structure's charge, removing the need for a non-stoichiometric number of oxygen ions, and the inherent associated vacancies within the structure.

However, once again the analogue did not form. It is possible that Sr_4OCl_6 is more stable than $NdSrZnO_3Cl$ at the low synthesis temperatures that were needed to prevent halide volatilisation, and that this prevented the target phase from forming. Another possibility is that the vacancies associated with the non-stoichiometric amount of oxygen present in the parent compound somehow stabilise the structure as a whole, and that without their presence the structure cannot form.

6.4.1 Orthorhombic → Tetragonal Structural Comparison

Generally zinc favours octahedral or tetrahedral coordination environments, and thus would be expected to be stable within a K_2NiF_4 structure, and indeed zinc is known to exist within the related double perovskite phase $BaLaZnRuO_6$ [4]. However, the zinc ions in the two compounds, $BaLaZnRuO_6$ and $NdSrZnO_{4-x}$, are in quite different coordination environments. One compound has distorted zinc-oxygen octahedra within its structure, with two long apical bonds and four shorter equatorial bonds, whilst the other has a more regular arrangement of bond lengths. The bond lengths within the $NdSrZnO_{4-x}$ structure are four bonds of approx. 1.89 Å and two of 2.29 Å, whereas the $BaLaZnRuO_6$ structure has four bonds of 2.05 Å and two of 2.02 Å.

The zinc octahedra are responsible for the change from the orthorhombic to the tetragonal phase. Two partially occupied oxygen sites are present within the orthorhombic phase, O(2) (0, ½, 0) and O(3) on (½, 0, 0), but the oxygen atoms distributed between these two sites are restricted to only one within the tetragonal phase (0.0979, ½, 0). The two oxygen positions result in different lengths for the *a* and *b* parameters, thus causing the structure to be orthorhombic, whereas the disordered oxygen position results in equal *a* and *b* parameters (see Fig. 6.4.1a) in the tetragonal form.

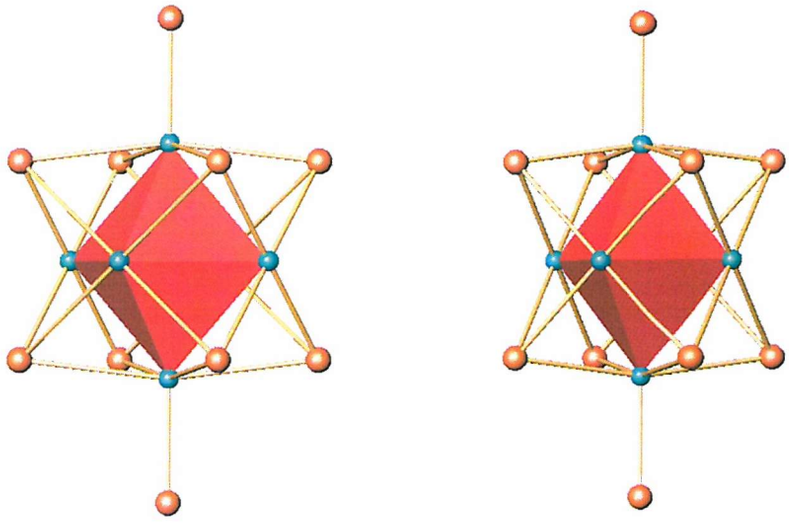

Figure 6.4.1a Simplifed representations of the orthorhombic and tetragonal forms of $NdSrZnO_{4-x}(CO_3)_y$ (carbonate not shown) ZnO_6 octahedra

This change in the oxygen positions almost certainly results from thermal stabilisation effects associated with the different synthesis temperatures used, and is not associated with the oxygen stoichiometry of the phases, which remains constant (within experimental error) at 3.5.

Order to disorder / orthorhombic to tetragonal phase transitions have been noted in $YBa_2Cu_3O_{7-x}$ [10] and related phases such as $GdBa_2Cu_3O_{7-x}$ [11]. In fact, the superconducting properties of $YBa_2Cu_3O_{7-x}$ have been shown to strongly depend on the overall oxygen stoichiometry and the ordering of oxygen vacancies within the structure [10].

Therefore, one possible explanation for the phase transition observed for $NdSrZnO_{4-x}$ is that it too undergoes an oxygen vacancy order to disorder transition that results in an orthorhombic to tetragonal phase transition. A similar phase change has been observed for Pr_2NiO_{4-x}, another compound that adopts the K_2NiF_4 structure, making it seem probable that oxygen vacancy ordering is indeed responsible.

If this is correct, then the orthorhombic structure produced at 1025 °C results from an uneven distribution of the basal oxygen vacancies associated with the O(2) and O(3) positions, whereas at 1100 °C the oxygen vacancies are more mobile and upon quenching settle into an approximate 50:50 distribution to produce a tetragonal diffraction pattern. As PND is an average technique it is unsuitable for examining the local bonding environment experienced by individual atoms and would not be able to pick out the oxygen vacancy positions accurately. To determine the true local bonding environment for the zinc atoms within this structure another analytical technique would need to be used, e.g. EXAFS.

However, if an order to disorder transition were responsible for the transition from orthorhombic to tetragonal structure type it would be expected to be a reversible phase change, i.e. that the tetragonal phase would only be observable at high temperature. The fact that the phase does not revert to an orthorhombic structure on cooling suggests that some other effect might be responsible.

One alternative explanation for the orthorhombic to tetragonal phase transition could be loss of zinc at elevated temperatures. This could lead to a more ordered bonding environment. However, any significant loss of cation would be expected to lead to a change in oxygen content, which is not observed.

Overall, it is unclear what effect is responsible for the phase transition observed for this phase.

6.4.2 Partially Carbonated Structure

The orthorhombic form incorporates a very small amount of carbonate within its structure to give the formula $NdSrZnO_{4-x}(CO_3)_{0.04}$ whilst the tetragonal form contains a larger, but still small, amount of carbonate to give the formula $NdSrZnO_{4-x}(CO_3)_{0.09}$. It seems surprising that the tetragonal form of the compound contains more carbonate, when you consider that this has been heated to a higher temperature, however, one potential explanation for this could be that the tetragonal form of this compound is able to incorporate more carbonate, as its O(2) environment may be better able to bond to the disordered carbonate ions (see Fig. 6.4.1b).

Although only simple oxide carbonates are known for the rare earth elements (and equally for zinc) copper oxide carbonate chemistry has been extensively explored, due to the associated interest of high T_c superconducting cuprates. The structures of the copper oxide carbonates reveal that carbonate groups may readily replace cuprate groups, enabling strings of carbonate ions to take the place of copper oxide chains [12], or for the formation of alternating CuO_4–CO_3–CuO_4 chains, as in $Sr_2CuO_2(CO_3)$ [13].

However, the copper oxide carbonates tend to contain substantial quantities of carbonate, whereas our $NdSrZnO_{4-x}(CO_3)_y$ phases contain very little. Such small amounts of carbonate ions, as found in our phases, cannot be modelled and structural refinements of the tetragonal and orthorhombic $NdSrZnO_{4-x}(CO_3)_y$ phases have proved too unstable to yield useful information about the arrangement of the carbonate ion.

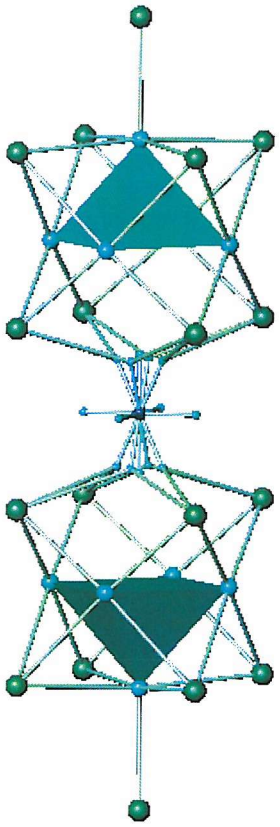

Figure 6.4.1b Simplifed representation of the tetragonal $Ba_4In_2(CO_3)O_6$ structure, with disordered carbonate ions (with partially occupied oxygen sites) present between the basal planes of the InO_5 square-based pyramids (green spheres represent neodymium and strontium ions, green square pyramids represent zinc polyhedra, pale blue spheres represent oxygen ions, dark blue sphere represents the carbon ion)

Syntheses using metal oxides as the only starting material did form the orthorhombic phase, but were unable to produce a pure phase tetragonal product. As a result we are unable to compare the non-carbonated forms of the two phases with each other (to fully examine the structural transition from orthorhombic to tetragonal), or with the carbonated forms (to determine structural changes resulting from carbonate inclusion).

6.5 Conclusions

Both orthorhombic and tetragonal phases of $NdSrZnO_{4-x}(CO_3)_y$ have been synthesised and studied by PND. Unfortunately little structural information has been gained from this study due to the difficulty associated with modelling small proportions of carbonate within the two structures.

However, the orthorhombic and tetragonal $NdSrZnO_{4-x}$ structures remain interesting examples of zinc in a distorted six-coordinate geometry with long apical bonds. PND data suggests that the orthorhombic to tetragonal phase transition occurs when oxygen that is distributed between two partially occupied sites in the orthorhombic phase, is restricted to only one site within the tetragonal phase.

Although non-carbonate routes to the $NdSrZnO_{4-x}$ compound were tried, these were not able to form the tetragonal phase, and thus were not of use in exploring the structural arrangement of carbonate within this compound.

None of the synthetic attempts to produce analogues of $NdSrZnO_{4-x}$ were successful.

6.6 References

1 Gross F, Vahrenkamp H, Müller-Hartman A, *Eur. J. Inorg. Chem.*, 2000, **11**, 2363

2 Feng P, Bu X, Stucky G D, *Acta Cryst. C*, 1997, **53**, 997

3 Attfield M P, Battle P D, Bollen S K, Kim S H, Powell A V, Workman M, *J. Solid State Chem.*, 1992, **96**, 344

4 Hong K-P, Choi Y-H, Kwon Y-U, Jung D-Y, Lee J-S, Shim H-S, Lee C-H, *J. Solid State Chem.*, 2000, **150**, 383; Battle P D, Gibb T C, Jones C W, Studer F, *J. Solid State Chem.*, 1989, **78**, 281

5 Unknown Reference

6 Grandjean D, Weller M T, *Mat. Res. Bull.*, 1993, **28**, 685

7 Larson A C, von Dreele R B; *General Structure Analysis System*, Los Alamos National Laboratory LAUR, 1994, 86 – 748

8 Williams D H, Fleming I, *Spectroscopic Methods in Organic Chemistry*, McGraw-Hill Publishing Co., Maidenhead, 1995

9 Baszczuk A, Wolcyrz M, Zygmunt A, *J. Alloys Compd.*, 2003, **360**, 1

10 Jorgensen J D, Shaked H, Hinks D G, Dabrowski B, Veal B W, Paulikas A P, Nowicki LO J, Crabtree G W, Kwok W K, Nunez L H, *Physica C*, 1988, **153-155**, 578

11 Prado F, Caneiro A, Serquis A, *Physica C*, 1998, **295**, 235

12 Fracesconi M G, Greaves C, *Supercond. Sci. Technol.*, 1997, **10**, A29

13 Armstrong A R, Obhi H S, Edwards P P, *J. Solid State Chem.*, 1993, **106**, 120